Vertical Contrast Interferometry and Bloch-Band Approach to Atom Optics

Daniel Gochnauer

A dissertation
submitted in partial fulfillment of the
requirements for the degree of

Doctor of Philosophy

University of Washington

2020

Reading Committee:

Subhadeep Gupta, Chair

Boris Blinov

Lukasz Fidkowski

Program Authorized to Offer Degree:
Physics

University of Washington

Abstract

Vertical Contrast Interferometry and Bloch-Band Approach to Atom Optics

Daniel Gochnauer

Chair of the Supervisory Committee:
Subhadeep Gupta
Department of Physics

This dissertation covers a series of atom interferometry experiments with a focus on applying the Bloch-band model to atom optics and performing vertical interferometry with a magnetically neutral atom. This approach lets us analyze the diffraction processes from a pulsed optical lattice in terms of the Bloch solutions for the atom in the periodic lattice Hamiltonian. Using a ytterbium (^{174}Yb) Bose-Einstein condesate as the matter-wave source, measurements of Rabi frequencies, as well as those of diffraction phase and amplitude, demonstrate the validity of the Bloch-band approach over a regime which is typically satisfied within an atom interferometer. Applications for this model are discussed, including the use of an interferometric phase measurement to determine an unknown band structure. Additionally, a unique feature of the excited Bloch-bands—the magic depth—is exploited to improve the phase stability of atom interferometers which use Bloch oscillations for large momentum transfer. We also demonstrate the technique of delta-kick cooling as a fruitful method for reduction of the BEC's vertical velocity distribution, allowing for more efficient momentum transfer with a vertical optical lattice. This is a crucial tool for non-magnetic atoms such as ^{174}Yb, which we use to perform vertical interferometry in our system with both a contrast interferometer geometry and a double Mach-Zehnder interferometer. Lastly, the effect of Landau-Zener-Stückelberg interference during Bloch oscillations is studied in its relation to momentum transfer efficiency for precision interferometry.

ACKNOWLEDGMENTS

I would like to thank those who enabled the success of these experiments as well as those who encouraged me throughout my time in the University of Washington graduate program.

First and foremost I want to acknowledge my advisor and our lab PI, Deep Gupta. He was inspirational and instructive, motivating me to become a better physicist and providing me with the intellectual tools I needed to succeed. He delivered direction to our lab's experiments while also allowing us to be innovative and pursue our own curiosities.

Ben Plotkin-Swing and Katie McAlpine were the graduate students senior to me in Deep's group. This work certainly would not have been possible without the work they have done before me—this also includes contributions from Alan Jamison during an earlier iteration of the experiment. Ben, being the most senior student, also filled a mentorship role for me during our overlapping time in the lab.

Our more recent grad student additions, Tahiyat Rahman and Anna Wirth-Singh, have been a great help as well. Their frequent extractions from my knowledge and experience affirmed my own understanding of our experiment, while their fresh ideas often led to new and interesting discussions about older concepts.

Deep incorporated a number of undergraduate students into our lab, all of whom contributed considerably during their more brief passages through the group. Some of those I have personally interacted with and would like to thank include Ryan Weh, Brendan Saxberg, Aruku Senoo, Pasha Bullock, and Andrew Ivanov. In addition to these UW undergrads, I would like to recognize contributions from some of our summer REU students, Eric Cooper and Camden Kasik.

Ting Lin, a fellow physics graduate student in my cohort, was the most prominent intel-

lectual stimulus outside of Deep's lab. His sincere interest in my work gave rise to relevant, engaging conversations. Similarly, his friendship and abundance of common interests found us in many less-relevant, yet still engaging, conversations.

Finally, I want to thank my family, including my parents and my wife, Cassidy, in particular. Their continued support throughout this doctoral program was immensely appreciated. Cassidy's willingness to listen to my endless physics ramblings as a non-physicist enabled me to improve in tailoring my explanations for multiple levels of understanding, and her encouragement continually inspired me when I most needed it.

This work was supported by NSF Grant No. PHY-1707575.

TABLE OF CONTENTS

LIST OF FIGURES

GLOSSARY

AD9910: the particular DDS device used in our lab. Output frequencies range from about 10 to 400 MHz.

AGB: anti-gravity beam. A carefully shaped optical potential intended to cancel the linear gravitational potential over some small region of space.

AOM: acousto-optic modulator. This ubiquitous lab tool uses the acousto-optic effect to deflect and shift the frequency of light using sound waves.

BEC: Bose-Einstein condensate. Bosons at sufficiently low temperatures may condense into this state of matter in which a large fraction of the particles exist in identical quantum states.

BO: Bloch oscillation. Periodic behavior of a particle's velocity within a lattice potential arising from a relative acceleration.

CI: contrast interferometer. A symmetric three-path interferometer designed for measuring recoil phase.

CICERO: timing software used for constructing sequences of digital pulses and analog waveforms.

DDS: direct digital synthesis. This method of signal generation begins with generating a time-varying signal in digital form and then performing a digital-to-analog conversion

DKC: delta-kick cooling. A matter-wave lensing technique for reducing the velocity distribution of a BEC or thermal atom cloud.

DRG: digital ramp generator. In DDS control, this module designates frequency ramp parameters.

LRR: useful for debugging the AD9910. When the Load LRR @ I/O update bit is effective, the OSK amplitude ramp rate timer is reloaded anytime an I/O update is asserted or a profile change occurs.

LZS: refers to Landau-Zener-Stückelberg interferometry. A process which is studied here in its relation to BO efficiency.

MOT: magneto-optic trap. This trapping method captures neutral atoms and can cool them to the Doppler temperature.

ODT: optical dipole trap. This trapping method for neutral atoms can reach temperatures sufficiently low for Bose-Einstein condensation.

OSK: output shift keying—sometimes called amplitude shift keying—is a form of amplitude modulation in DDS control.

PBS: polarizing beam splitter. A cube-shaped optic which splits laser light into two orthogonal linear polarization components.

PLL: phase locked loop. This is a common method for generating high frequency waveforms equivalent to some integer multiple of a lower input frequency.

PMT: photomultiplier tube. An extremely sensitive light detector, capable of measuring individual photons.

QED: quantum electrodynamic theory. The precise measurement of a recoil frequency may serve as a test of QED by its connection to the fine-stricture constant and a comparison with alternative competitive measurements.

Chapter 1
INTRODUCTION

Within the conventionally titled realm of atomic, molecular and optical physics lies the more narrowly defined area involving the study of ultracold neutral atoms. Further within this subset is the practice of probing fundamental physics specifically through atom interferometry. This high degree of specialization, even among 'physics' in general, necessitates the development of several relevant and significant concepts before turning to our latest experimental work and subsequent results. In this chapter I will attempt to introduce the basic ideas behind the experiments performed in our ultracold atoms lab, each of which will appear again and be expanded upon in later chapters.

While composed of many noteworthy constituent devices prevalent in the field of atomic physics, the key tool used for experiments in our lab is the comprehensive apparatus—an atom interferometer. Here we will lay the groundwork for understanding atom interferometry, describe several novel interferometer designs and applications, and discuss a new approach to atom optics which leads to an innovative technique for obtaining high momentum separation within an atom interferometer. The following chapters will cover details of our experimental apparatus, elucidate the processes which make up atom optics elements, and present observations and results within the context of a generally applicable Bloch-band model.

1.1 Atom Interferometers

Interference is a common colloquial term which can be understood as coming into collision or opposition, or interposing in the business of another entity. It is even vaguely recognized as having something to do with physics, being observed in phenomena such as electrical

interference or radio static. The definition we want to use here is this: the combination of two or more waveforms into a superposition to form a resultant wave in which the amplitude may be greater, reduced, or unchanged. Typically this notion of interference is introduced to young physicists in an example pertaining to electromagnetic waves, perhaps as part of laser optics course. Much more mundane examples exist among everyday occurrences, however, such as interfering ripples in a pond or using noise-canceling headphones.

A much less ubiquitous term, on the other hand, is interferometer. Generically an interferometer is a tool for measuring the relative phase of two interfering waveforms. The usefulness of such a device is limited only by the ability of one to conceive a means for recasting another problem into one associated with wave manipulation. For example, a ruler is one way of measuring length, but a much more sensitive measurement can be made with a Michelson interferometer[1] [43].

As with general interference, interferometry is typically observed through the medium of electromagnetic waves. The sensitivity of a measurement is improved with the phase-coherence and monochromaticity of the wave; therefore, the development of laser technology has led to a significant prevalence of laser light among interferometric applications. This has established a conventional notion that interferometers are comprised of a light wave which is manipulated by material optics (e.g. beam splitters, mirrors, polarizers). Nonetheless, with the advent of quantum mechanics came an accepted understanding that even matter may exhibit wave properties—this includes interference. It was inevitably demonstrated that atom interferometry could be performed [13] with strong atom-photon coupling allowing for straightforward manipulation (e.g. splitting, reflecting) of the atomic wave packets.

Like the laser sources in light interferometry, it is desirable for the matter wave to be both coherent and monochromatic. According to the de Broglie wavelength, $\lambda = h/p$, a highly monochromatic matter wave can be equivalently described as having a narrow momentum

[1] There exist a multitude of different interferometer configurations; thus, it would be impractical to detail the geometry and unique applications of each. Exceptions will be those with particular relevance to this work, illustrations of which may be found in Figures 1.1 and 1.2.

distribution. Thus atom interferometry benefited greatly from the concurrent realization of ultracold, quantum-degenerate Bose gases [4] (i.e. Bose-Einstein condensates) which can be produced in an ultra-high vacuum environment ideal for sensitive interferometric measurements. In such systems (discussed partly in Chapter 2 and more fully in [53]) the interferometer sequence is typically performed on atoms in free-fall, which limits the duration of experiments to the time atoms remain within a specific region of space defined mostly by the size and orientation of the optical lattice beams but also by the size of the vacuum chamber. This limitation may be reduced, however, by either (i) increasing the region of interest through adding, e.g., a vertical optical lattice and an atomic fountain [66] or by (ii) reducing the effect of gravity to increase the time directly, e.g., through installation on a drop tower [47], ballistic rocket [59], or satellite [10].

As we will see in future chapters, one of the focal points of this work is the implementation of a vertical optical lattice in our system, with which we could extend the interferometer duration within an atomic fountain. In comparison to our previously horizontal lattice where the interaction times are limited to the time it takes for the atoms to fall through the lattice beams, in a vertical lattice the atoms stay positioned within the center of the beams and the total interferometer time can be made arbitrarily large. This in turn allows for more phase accumulation and, thus, higher sensitivity which directly benefits precision measurement applications.

Finally, due to their large mass and short wavelength (compared with photons) atoms provide high sensitivity as a matter wave source. Additionally, using an interferometer as the metrological instrument innately provides high sensitivity due to the periodic nature of the interfering waves. That is, a meaningful phase measurement must have some finite uncertainty less than 2π, but compared with the phase accrued over an arbitrarily large number of periods the relative phase uncertainty can be made quite small. This is, in fact, the key for using interferometers to make precise measurements.

1.1.1 Mach-Zehnder Interferometer

Of the two atom interferometer geometries we have utilized for our various experiments, the simpler configuration to understand is the well-known Mach-Zehnder interferometer. The geometry of this atom interferometer is depicted in Figure 1.1(a) where the primary constituents are shown to be a splitting $\frac{\pi}{2}$–pulse, a reflection/mirror π–pulse, and a readout $\frac{\pi}{2}$–pulse. As alluded to in the previous section, these applied pulses—also known as atom optics—come from the interaction of atoms with an optical lattice formed by two counter-propagating laser beams. Later chapters will provide more explanation about atom optics, but for now simply understand the language used here as identical to that for a general quantum two-level system represented on a Bloch sphere.

Because the frequency of oscillation in a matter wave is related to the particle group velocity, it becomes convenient to assess the behavior or this interferometer in the momentum basis[2]. In our experiments each of the aforementioned pulses couples the $|0\hbar k\rangle$ and $|6\hbar k\rangle$ momentum states. This particular choice was based on an optimization of experimental parameters to attain the most repeatable interferometer signals[3]. The interferometer signal is obtained by using time-of-flight absorption imaging to measure the number of atoms projected into either of these two states; therefore, the population output with $0\hbar k$ and $6\hbar k$ momentum will be labeled P_0 and P_6, respectively.

These populations can be derived [39, 67] by adding the contributions from the two paths to obtain the total wavefunction, $\psi = \psi_1 + \psi_2$. We can write this in the momentum state basis as the superposition of four matter waves, following the final splitting pulse.

$$\begin{aligned} |\psi(x)\rangle = &\left(-\tfrac{A_1}{2}\mathrm{e}^{-\mathrm{i}\phi_1} - \tfrac{A_2}{2}\mathrm{e}^{-\mathrm{i}(\phi_2+6\phi_R/2)}\right)|0\hbar k\rangle \\ &+ \left(\tfrac{A_1}{2}\mathrm{i}\mathrm{e}^{-\mathrm{i}(6\vec{k}\cdot\vec{x}+6^2\omega_{\mathrm{rec}}t+\phi_1+6\phi_R/2)} - \tfrac{A_2}{2}\mathrm{i}\mathrm{e}^{-\mathrm{i}(6\vec{k}\cdot\vec{x}+6^2\omega_{\mathrm{rec}}t+\phi_2)}\right)|6\hbar k\rangle \end{aligned} \tag{1.1}$$

---

[2]This choice of basis will be reinforced when we consider the system with a Bloch-band approach later in this chapter.

[3]We will address this optimization in relation to controlling the diffraction phases systematic effect in Section 4.3.3.

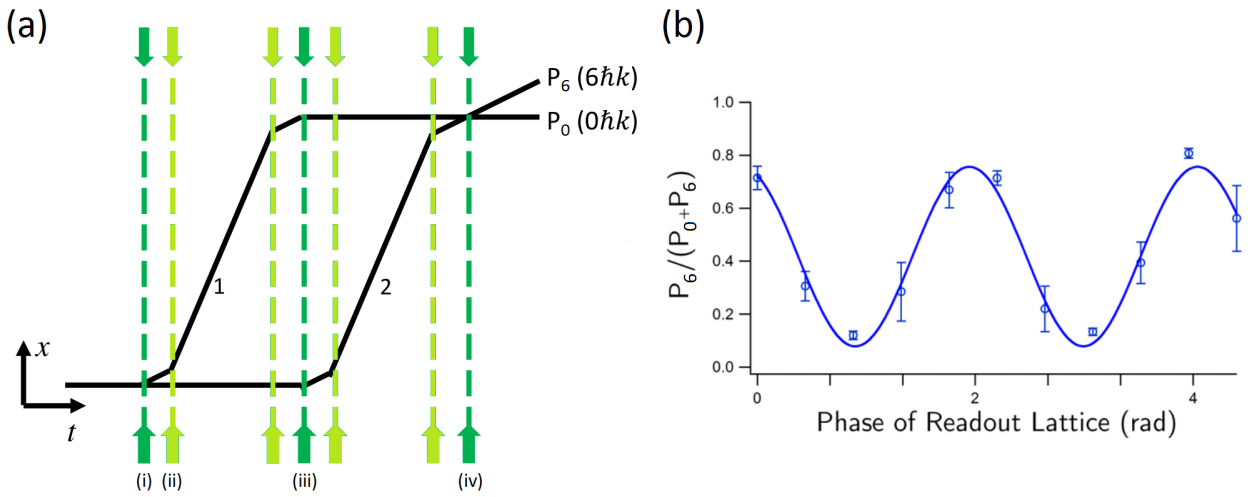

Figure 1.1: Mach-Zehnder atom interferometry. (a) Space-time diagram showing a typical geometry and sequence for a Mach-Zehnder interferometer. (i) The splitting pulse puts the atoms into an equal superposition state between $|0\hbar k\rangle$ and $|6\hbar k\rangle$, sending them along two distinct paths labeled 1 and 2. (ii) Optional acceleration and deceleration pulses will increase the area enclosed by the interferometer, and thereby its sensitivity. (iii) After substantial propagation time, a reflection pulse will exchange the momentum states of the atoms along the different paths. (iv) An equivalent propagation time ensures overlap of the atomic wavefunction. A final splitting pulse is applied to observe the interference between the two paths. (b) A sample interference fringe detected by measuring atom populations (see text), each point obtained from separate runs of the interferometer sequence.

where $\vec{k}$ is the wavevector of the optical lattice and $\hbar\omega_{\text{rec}} = \hbar^2k^2/2m$ is the recoil energy, defined as the kinetic energy of an initially motionless atom after absorbing one photon. For each path i, the amplitude A_i is due to the initial splitting pulse and the phase ϕ_i is accumulated over the duration of the path's trajectory until readout. The phase of the readout lattice is denoted by ϕ_R and is varied over multiple iterations to obtain an interferometer fringe.

From probability conservation $A_1 + A_2 = 1$, and with ideal parameters $A_1 = A_2$. Then computing $P_0 = |\langle 0\hbar k|\psi\rangle|^2$ and $P_6 = |\langle 6\hbar k|\psi\rangle|^2$ we have

$$\begin{aligned} P_0 &= \tfrac{1}{2}\left(1 + \cos(\phi_1 - \phi_2 + 3\phi_R)\right) \\ P_6 &= \tfrac{1}{2}\left(1 - \cos(\phi_1 - \phi_2 + 3\phi_R)\right) \end{aligned} \tag{1.2}$$

which will produce a pair of oscillatory signals with respect to ϕ_R. The $2\pi/3$ periodicity of this expression, demonstrated in Figure 1.1(b), is due to the choice in using $|0\hbar k\rangle$ and $|6\hbar k\rangle$ momentum states. Without loss of generality, a Mach-Zehnder interferometer fringe may be generated with this scheme by interfering $|0\hbar k\rangle$ and $|2N_B\hbar k\rangle$ momentum states, which will exhibit $2\pi/N_B$ periodicity with respect to the phase of the readout lattice.

The two interferometer paths each originate from the same coherent atom source, so intuitively the interference they experience at the end of the interferometer should include the difference in phase evolution between the two paths, $\Delta\phi = \phi_1 - \phi_2$. The path-dependent phase depends on the energy according to $\phi_i = \frac{1}{\hbar}\int E_i(t)\,\mathrm{d}t$; therefore, energetically different paths will be detectable in $\Delta\phi$. This makes the Mack-Zehnder interferometer ideal for measuring potential gradients in applications such as gravimetry [52, 1, 30] or inertial sensing of rotation and acceleration [48]. Alternatively, introducing some localized path-dependent energy shift (e.g. due to a massive object [6], or extraneous optical lattice potentials [40]) will make the interferometer asymmetric resulting in additional sources of detectable phase. This latter technique has been utilized to obtain the results in Chapter 5, where we analyze the lattice-induced phase shift arising from a particular optical lattice.

For the Mach-Zehnder interferometer—in fact, for any two-path atom interferometer—the interference fringe is usually obtained only after multiple runs of the experiment. This

is because the atom wave is not a continuous source and the sequence must be performed anew with each variation to ϕ_R. Many data points thus make up a single oscillatory signal. Unfortunately, due to technical noise in the apparatus the amplitude of this averaged signal follows the form

$$P_{\pm} = \frac{1}{2}\left(1 \pm V\cos(\phi_1 - \phi_2 + 3\phi_R)\right) \tag{1.3}$$

where the visibility, $0 \leq V \leq 1$, captures the reduced ability to produce clear interferometer fringes. One major source of reduced visibility in a two-path interferometer is vibrations, resulting in uncertain ϕ_R and other lattice phases. Vibration effects can be mitigated by setting up a simultaneous conjugate interferometer, or by using a three-path contrast interferometer. Such geometries feature multiple interfering arms which are manipulated by the same diffraction pulses. This allows interferometric measurements in which the vibration effect cancels out as common-mode between two sub-interferometers.

Finally, the sensitivity of this interferometer typically improves with (i) physical path separation for spatially dependent energy shifts and (ii) momentum separation for momentum dependent energy shifts in an asymmetric arrangement. In either case, these parameters may be increased by implementing the optional acceleration (and deceleration) pulses shown in Figure 1.1(a). Indeed, tools for achieving high-momentum interferometry are of significant interest in the field and a central pursuit in our work.

1.1.2 Contrast Interferometer

The development of the contrast interferometer was conceived with the foremost purpose of making atomic recoil measurements, in particular towards precise determination of the fine structure constant [25]. Its unique three-path geometry relieves the system of many problematic systematic effects and allows for a novel single-shot readout method. The geometry of this atom interferometer is depicted in Figure 1.2(a) where the primary constituents are shown to be a splitting pulse, a reflection/mirror π–pulse, and a traveling-wave readout pulse. Whereas all the pulses within the Mach-Zehnder interferometer coupled pairs of momentum

states with optical standing waves, each of these steps in the contrast interferometer acts on the atoms in a different manner.

To generate the three-path geometry, a transient[4] optical standing wave—known as a Kapitza-Dirac pulse—should be applied in the Raman-Nath regime [26] such that a multi-order diffraction pattern is produced from the optical grating felt by the matter wave. The amplitude of this pulse is tuned to make an equal superposition in the 0 and ± 1 diffraction orders, corresponding to $|0\hbar k\rangle$ and $|\pm 2\hbar k\rangle$ momentum states, respectively. The fraction put into higher orders may be suppressed by increasing the duration of this pulse until it lies just on the edge of the Raman-Nath regime. The reflection π–pulse operates in the same manner as the Mach-Zehnder atom optics: it couples two momentum states, namely $|+2\hbar k\rangle$ and $|-2\hbar k\rangle$, and is tailored to perform population inversion of the two states (i.e. a full half-rotation between the two poles around a Bloch sphere). The population of the central path is unaffected during this process[5].

The readout method for a contrast interferometer is unique in that it allows the use of a traveling wave of light rather than the optical standing wave used in the previous atom optics. The rationale for this can be explained by considering the behavior of the atomic wavefunction at the time when the three paths overlap. Qualitatively, one can envision the interference between paths 1 and 2 to form a standing matter wave moving with velocity $v = +1\hbar k/m$ in the lab frame. Likewise, the interference between paths 2 and 3 forms a standing wave moving at $v = -1\hbar k/m$. Finally, as overlap of all three paths occurs simultaneously, a composite standing matter wave is formed which is stationary in the lab frame and has temporal oscillation of its amplitude.

We can show this effect quantitatively [31, 25] by first writing the wavefunction

$$\psi(x) = A_1 \mathrm{e}^{-\mathrm{i}\left(2\vec{k}_{\mathrm{rec}}\cdot\vec{x}+2^2\omega_{\mathrm{rec}}t+\phi_1(T)\right)} + A_2 \mathrm{e}^{-\mathrm{i}\phi_2(T)} + A_3 \mathrm{e}^{-\mathrm{i}\left(-2\vec{k}_{\mathrm{rec}}\cdot\vec{x}+2^2\omega_{\mathrm{rec}}t+\phi_3(T)\right)} \tag{1.4}$$

[4] A short pulse with a frequency bandwidth larger than the recoil frequency, ω_{rec}, which defines the Raman-Nath limit.

[5] The component of the wavefunction pertaining to the center path is not completely unaffected. The optical lattice incurs a momentum-dependent phase shift, a systematic effect that we will investigate in depth when we reach Chapter 4.

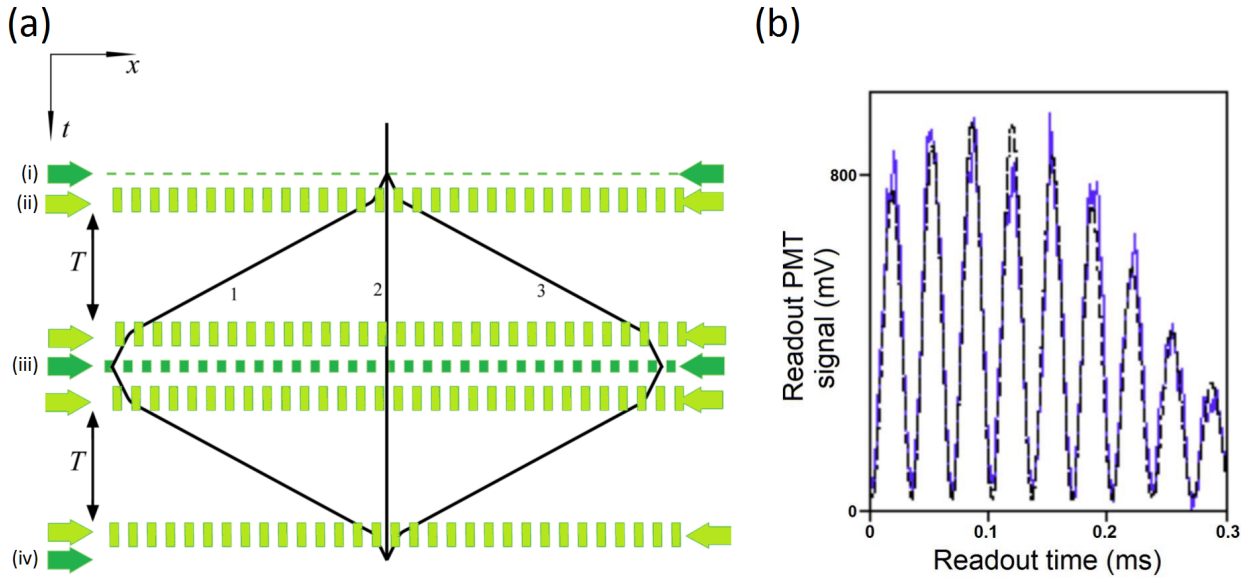

Figure 1.2: Contrast atom interferometry. (a) Space-time diagram showing a typical geometry and sequence for a contrast interferometer. (i) The splitting pulse puts the atoms into an equal superposition state between $|+2\hbar k\rangle$, $|0\hbar k\rangle$, and $|-2\hbar k\rangle$, sending them along two distinct paths labeled 1, 2, and 3. (ii) Optional acceleration and deceleration pulses will increase the area enclosed by the interferometer, and thereby its sensitivity. (iii) After substantial propagation time, a reflection pulse will exchange the momentum states of the atoms along the outer paths. (iv) An equivalent propagation time ensures overlap of the atomic wavefunction. A final traveling-wave (not standing-wave) readout pulse is applied to observe the interference between the three paths. (b) A sample interference fringe detected by the reflection of the readout light on a photomultiplier tube (see text), obtained from an average of 20 runs of the interferometer sequence.

at the time of overlap, $t = 0$, where $k = k_{\text{rec}} = 2\pi/\lambda_{\text{laser}}$ and ω_{rec} is the single-photon recoil frequency as before. Due to the symmetry of a contrast interferometer, the amplitude of the outer paths can be made equivalent such that $A_1 = A_3 \equiv A_{13}$. The density is therefore

$$\begin{aligned}|\psi|^2 &= |A_2|^2 + 2|A_{13}|^2 \\ &+ 2A_2A_{13}\left[\cos(2\vec{k}_{\text{rec}}\cdot\vec{x} + 4\omega_{\text{rec}}t + \phi_1(T) - \phi_2(T)) + \cos(2\vec{k}_{\text{rec}}\cdot\vec{x} - 4\omega_{\text{rec}}t - \phi_3(T) + \phi_2(T))\right] \\ &+ 2A_{13}^2\cos(4\vec{k}_{\text{rec}}\cdot\vec{x} + \phi_1(T) - \phi_3(T))\end{aligned} \tag{1.5}$$

where we can see that the temporal dependence lies solely within the second line of this expression. Using trigonometric identities this may be rewritten as

$$2A_2A_{13}\cos\left(2\vec{k}_{\text{rec}}\cdot\vec{x} + \frac{\phi_1(T) - \phi_3(T)}{2}\right)\cos\left(4\omega_{\text{rec}}t + \frac{\phi_1(T) + \phi_3(T)}{2} - \phi_2(T)\right) \tag{1.6}$$

which elucidates the spatial and temporal oscillatory behavior, with periodicity $2\pi/2k_{\text{rec}}$ and $2\pi/4\omega_{\text{rec}}$, respectively. At times where this standing matter wave exhibits high contrast, the spacing between peaks would be given by $\lambda_{\text{laser}}/2$, which is unresolvable with our imaging system. The preferred method to observe this interference is to treat the standing matter wave as a density grating and perform Bragg scattering with a near-resonant optical traveling wave. In fact, the source for this light may be the same as was used for the atom optics which set the scale of the density grating. The temporal oscillation of the grating contrast will then manifest in the coherently reflected readout light, but with twice the frequency due to the positive-definite nature of contrast. Additionally, the dependence on T can be made explicit by writing $\phi_i(T) = N_i^2\omega_{\text{rec}}2T + \phi_i$ where the momentum of atoms along path i on the interval T is denoted $p_i = N_i\hbar k$. Therefore, the final functional form for a contrast interferometer readout signal is

$$S(t,T) = C(t,T)\cos^2\left(4\omega_{\text{rec}}t + \frac{1}{2}n^2\omega_{\text{rec}}T + \frac{\phi_1 + \phi_3}{2} - \phi_2\right) \tag{1.7}$$

where $n = |N_1| + |N_3|$ is now the momentum separation of paths 1 and 3 on the interval T, the envelope function $C(t,T)$ is related to the coherence length of the atomic wave packet, and the phases ϕ_i account for heretofore unspecified contributions (e.g. magnetic or

gravitational energy shifts, kinetic energies between diffraction pulses, lattice-induced shifts during the pulses). Similar to [66] but different in methodology, the readout signal for a contrast interferometer conveniently displays an entire interference fringe in a single run of the experiment.

The design of the contrast interferometer was drawn from an inclination towards measuring atomic recoil frequencies for obtaining a precise value of the fine structure constant α. This may be seen by the clear dependence on ω_{rec} in Equation (1.7) where the sensitivity of such measurements grows linearly with T and quadratically with n, making the addition of acceleration pulses especially valuable. Due to the relationship between other path-dependent phases $\left(\frac{\phi_1+\phi_3}{2} - \phi_2\right)$ and the symmetry of the contrast interferometer, the signal is insensitive to linear potentials (e.g gravity, linear Zeeman shifts) and vibration effects. However, this interferometer is inherently sensitive to lattice-induced phase shifts because the shifts to ϕ_1 and ϕ_3 have the same sign and are different in magnitude from ϕ_2, a point which we will return to in Chapter 4.

1.1.3 Landau-Zener-Stückelberg Interferometer

While we did not explicitly use it for interference measurements, the Landau-Zener-Stückelberg (LZS) interferometer we employed was technically an atom interferometer as well and shall therefore be introduced within this section. Unlike the previous two interferometers, however, the measurable phase difference is not due to the spatial separation of each path. Instead, the phase difference arises from the different band eigenenergies of the atoms as they traverse an optical lattice through different Bloch bands (see later section). This concept is illustrated in Figure 7.4 within the chapter on LZS interferometry. It may be helpful when reading that content to have a fuller understanding of the Bloch-band approach to atom optics—addressed in the preceding chapters—thus, I will continue here with additional introductory material before proceeding to describe our experiments.

1.2 Measuring the Fine Structure Constant

The fine structure constant, α, can be construed as a representation of the coupling strength between light and matter through electromagnetic interaction. It is not a surprise, therefore, that this quantity is highly relevant to atomic physics, where many experiments involve some application of this light-matter interaction. The fine stricture constant is dimensionless with a value approximately $\frac{1}{137}$, and may be written as the ratio of several other physical constants:

$$\alpha = \frac{e^2}{4\pi\epsilon_0\hbar c} \tag{1.8}$$

where e is the fundamental charge, ϵ_0 is the permittivity of free space, $\hbar$ is the reduced Planck's constant, and c is the speed of light in vacuum.

A particular relevance of α to atomic physics lies in its connection to recoil measurements, while the significance of this relation comes from offering a means to test quantum electrodynamic theory (QED). According to QED the anomalous part of the electron gyromagnetic ratio, $g-2$, may be expressed as a power series in α. Precision measurements of $g-2$ coupled with tenth-order series expansions from QED perturbation theory has led to a value for α with 0.25 ppb accuracy [27, 5]. An atomic recoil measurement would procure a value for the fine structure constant independent of QED, and a comparison between values obtained by the two methods would serve as a test of the QED theory.

Using constants from atomic physics, Equation (1.8) may be rewritten as

$$\alpha^2 = \frac{4\pi R_\infty}{c}\frac{m}{m_e}\frac{\hbar}{m} \tag{1.9}$$

where $R_\infty = m_e e^4/\left((4\pi)^3\epsilon_0^2\hbar^3 c\right)$ is the Rydberg constant with an infinitely massive nucleus, m_e is the electron mass, and m is the mass of our atom of interest. Whereas R_∞ is known to 0.006 ppb [45], the electron mass is known to 0.03 ppb [65], and the atomic mass of most species used in this type of experiment (e.g. ytterbium) is known better than 0.1 ppb [56], the ratio $\hbar/m$ remains the least well-known quantity in this expression. The current best measurement was obtained using a cesium interferometer leading to 0.2 ppb accuracy in α [51]. By the definition of the atomic recoil frequency we know the ratio $\hbar/m = 2\omega_{\text{rec}}/k_{\text{laser}}^2$; thus,

along with good knowledge of the optical lattice wavevector, k_{laser}, an atom interferometer supports the pursuit of precise α measurements through a recoil measurement.

A precision measurement of alpha using Yb is a long-term motivation for much of the work in our lab [25, 32, 33, 54]. More recently, we have begun to broaden our atom optics efforts by exploring the Bloch-band model [24, 40] as a tool for advancing atom optics techniques—in particular, techniques which can enhance the sensitivity of interferometers for various precision measurement applications.

1.3 Bloch-band Model

The characteristics of spatially periodic potentials became well-understood following the investigation of Felix Bloch in 1928 [8], developed at the time to gain an understanding of electron motion in ionic lattices. The eigenstate solutions to this problem give rise to the distinguished band structure model which allowed a proper explanation of electron conductance, the evaluation of electromagnetic properties in crystals, and the prediction of Bloch oscillations. While initially limited to applications in solid state physics, the Bloch-band model may be used in any system with a periodic potential—specifically, ultracold atom systems may very easily be subjected to periodic optical potentials and, due to the high degree of experimental control, become a quantum simulator for solid state lattice structures.

1.3.1 Bloch Solution Derivation

The simplest 1-dimensional example of a periodic potential is a sinusoid, $V(x) = U_0 \cos kx$, which may be realized as an optical potential by an arrangement of counter-propagating laser beams. In this example the lattice has periodicity $a = 2\pi/k$. In order to normalize the wavefunctions, first write each wavefunction as

$$\Psi(x) = \sum_q a_q \mathrm{e}^{\mathrm{i}qx} \tag{1.10}$$

and define periodic boundary conditions $\Psi(x + Na) = \Psi(x)$ within a finite lattice of N sites. Converting the potential into a form with complex exponentials and inserting into the

Schrödinger equation yields

$$\sum_{q'}\left(\frac{\hbar^2 q'^2}{2m}\mathrm{e}^{\mathrm{i}q'x}+\frac{U_0}{2}\mathrm{e}^{\mathrm{i}(q'+k)x}+\frac{U_0}{2}\mathrm{e}^{\mathrm{i}(q'-k)x}\right)a_{q'}=E\sum_{q'}\mathrm{e}^{\mathrm{i}q'x}a_{q'} \tag{1.11}$$

which can subsequently be multiplied by $\mathrm{e}^{-\mathrm{i}qx}/Na$ and integrated over x from $-Na/2$ to $Na/2$. This produces

$$\frac{\hbar^2 q^2}{2m}a_q+\frac{U_0}{2}a_{q-k}+\frac{U_0}{2}a_{q+k}=Ea_q \tag{1.12}$$

showing that some Fourier components with different q couple to each other but only if their difference is k. Here we can identify the concept of quasimomentum, where q is redefined to exist only on the interval $-\pi/a<q\leq\pi/a$ also known as the first Brillouin zone. Therefore, writing the quasimomentum as $q+lk$, where $l\in\mathbb{Z}$, and defining $a_{q+lk}=a_l^{(q)}$ turns Equation (1.12) into

$$\frac{\hbar^2(q+lk)^2}{2m}a_l^{(q)}+\frac{U_0}{2}a_{l-1}^{(q)}+\frac{U_0}{2}a_{l+1}^{(q)}=Ea_l^{(q)} \tag{1.13}$$

Assuming the eigenenergies, E, are significantly smaller than $(\hbar l'k)^2/2m$ it becomes a good approximation to let $a_l^{(k)}=0$ for $|l|>l'$, reducing the eigenvalue problem to a $(2l'+1)$ dimensional space. For example, truncating to five states looks to solve

$$\begin{pmatrix}\frac{\hbar^2(q+2k)^2}{2m} & U_0/2 & 0 & 0 & 0\\ U_0/2 & \frac{\hbar^2(q+k)^2}{2m} & U_0/2 & 0 & 0\\ 0 & U_0/2 & \frac{\hbar^2 q^2}{2m} & U_0/2 & 0\\ 0 & 0 & U_0/2 & \frac{\hbar^2(q-k)^2}{2m} & U_0/2\\ 0 & 0 & 0 & U_0/2 & \frac{\hbar^2(q-2k)^2}{2m}\end{pmatrix}\begin{pmatrix}a_2^{(k)}\\ a_1^{(k)}\\ a_0^{(k)}\\ a_{-1}^{(k)}\\ a_{-2}^{(k)}\end{pmatrix}=E\begin{pmatrix}a_2^{(k)}\\ a_1^{(k)}\\ a_0^{(k)}\\ a_{-1}^{(k)}\\ a_{-2}^{(k)}\end{pmatrix} \tag{1.14}$$

which is a standard eigenvalue problem producing $(2l'+1)$ eigenenergies, $E_n(q)$, where we will now label $n=1,2,...,(2l'+1)$ as the band number and k as the Bloch vector (or reciprocal lattice vector). For a given band index and Bloch vector, the coefficients corresponding to the eigenvalues from Equation (1.14) are denoted by $a_l^{(nq)}$. Using Eqn. (1.10) we then obtain the generalized form

$$\Psi_{nq}(x)=\mathrm{e}^{\mathrm{i}qx}u_{nq}(x)\,,\quad \text{where}\quad u_{nq}(x)=\sum_l a_l^{(nq)}\mathrm{e}^{\mathrm{i}lkx} \tag{1.15}$$

are the well-known Bloch wavefunctions. Note that these solutions have the same periodicity as the lattice potential, except in the case that either $k = 0$ or $a = 0$. In our work we exchange the traditionally labeled band number n for $b + 1$ (to prevent confusion between other uses for n), where $b = 0$ is defined as the ground band and all $b > 0$ are referred to as the excited bands.

1.3.2 Application to Ultracold Atoms

Rather than the eigenfunctions, however, it may be argued that the eigenenergies portray more useful information about the behavior of particles in this system. Figure 1.3(a) shows that the eigenstates separate into regions of allowed and disallowed energies (hence the use of the term "bands"). In ionic crystals this can be used to discern the conducting or insulating properties of the material. With ultracold atoms the connection between different momentum states can be used to transfer or accelerate the atoms. The two primary techniques we use for accelerating atoms rely on a periodic potential provided by an optical lattice, which is the reason for considering the Bloch-band model for understanding our system. I will go into more detail about these methods in Chapter 4, but as I am certain to refer to them before that point, I shall attempt here to provide an introductory understanding of the two techniques: Bragg diffraction and Bloch oscillations.

Define an N_B^{th} order Bragg transition as a $2N_B$ photon process connecting states $|-N\hbar k\rangle$ and $|+N\hbar k\rangle$, corresponding to ground-state atoms with momentum $-N\hbar k$ and $+N\hbar k$, respectively, in the reference frame of the optical standing wave. In this reference frame these energies will always be degenerate and fall within a band gap—understood as an avoided crossing—as shown in Figure 1.3. By considering this as a two-state system (perhaps envisioning the Bloch sphere), it should be evident that such transitions allow full conversion from one state to the other (i.e. a π–pulse) or partial conversion into a superposition state (e.g. a $\frac{\pi}{2}$–pulse). Because a single Bragg process only occurs as a pulse, atoms may only be accelerated to large momentum with this method by applying a sequence of Bragg pulses, each supplying $2N\hbar k$.

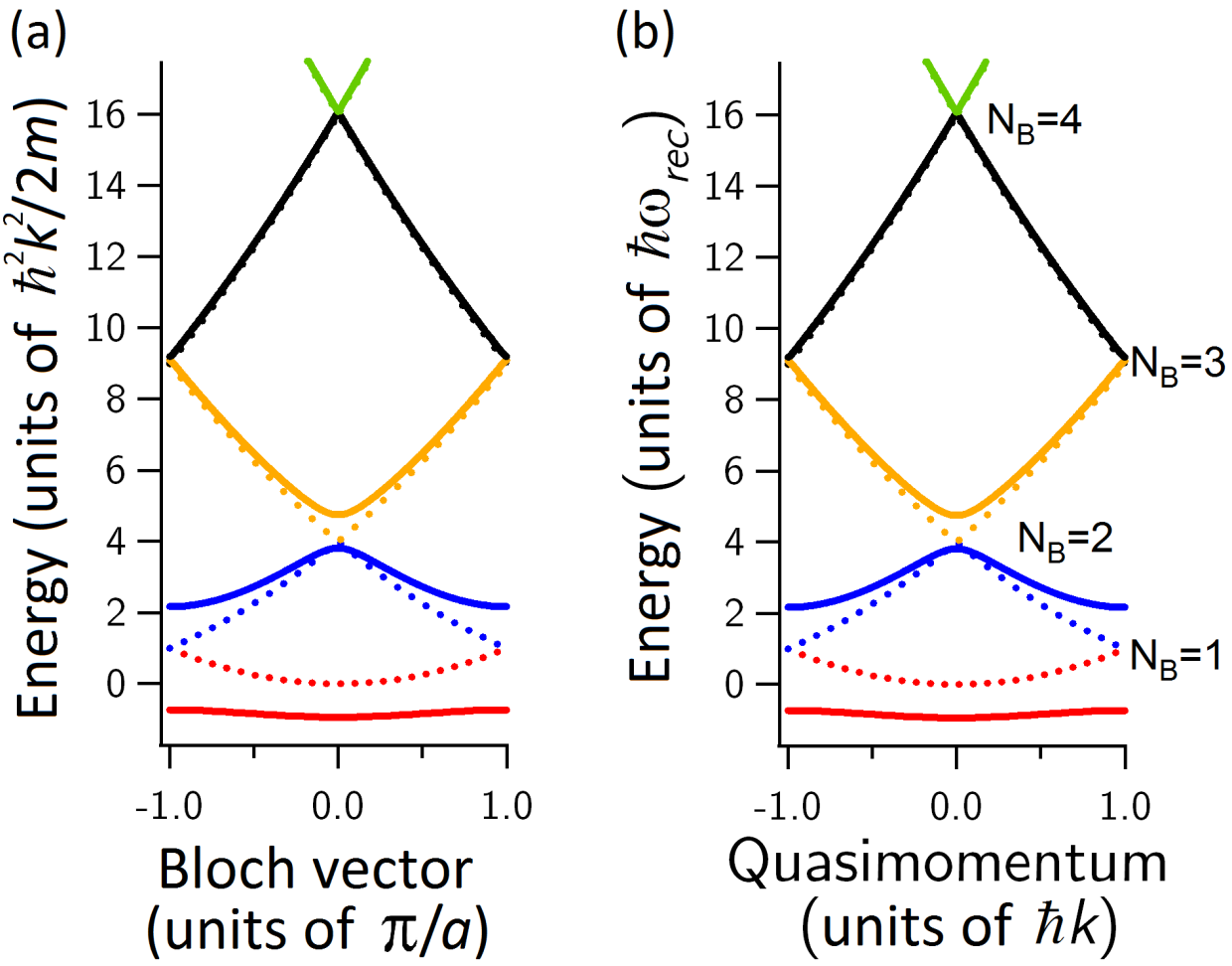

Figure 1.3: (a) Energy bands calculated for Equation (1.13) using $U_0 = 6\hbar^2k^2/2m$ (solid lines) compared with no periodic potential, by letting $U_0 = 0$ (dashed lines). (b) In the context of atom optics, the axes have been converted to units of recoil energy and recoil momentum. Bragg pulses of N_B^{th} order are performed around the designated band gaps (see text), indicated by $N_B = 1$ to 4.

Bloch oscillations, which I will sometimes shorten to BOs, describe the motion of a particle in a periodic potential in the presence of a constant force. In the context of ultracold atoms, the constant force is typically emulated by simply accelerating the optical lattice. Unlike Bragg pulses, a Bloch oscillation sees atoms in only a single band; the atoms' quasimomentum sweeps along a band as the lattice accelerates and, once it reaches the Brillouin zone edge, jumps to the other side of the Brillouin zone and continues accelerating. In this manner performing an integer number, n, of Bloch oscillations in the b^{th} excited band (denoted as n BbBO) will provide $2n\hbar k$ of total acceleration.

Chapter 2

EXPERIMENTAL APPARATUS

It can safely be asserted that experiments with ultracold neutral atoms are at the point where a Bose-Einstein condensate (BEC)-producing apparatus is often a prerequisite of an experiment rather than the featured result. To further illustrate this realization, there are already commercially available BEC machines from companies like ColdQuanta [12]. This is not meant to trivialize the creation of such an apparatus—it is a massive undertaking that often requires multiple years of graduate student work—but since I am several generations past the conception of our laboratory's BEC machine, I intend to focus primarily on my individual contributions and only briefly cover the theory involved for conventional BEC production. Additional details about the apparatus may be found in [53].

The main ingredients for an ultracold atom apparatus are (i) an atomic beam, (ii) a slowing mechanism, (iii) an initial dissipative trap, and (iv) a secondary conservative trapping potential, all of which are contained within an ultra-high vacuum system. In our lab we generate BECs of bosonic ytterbium, ^{174}Yb.

2.1 Ytterbium

Ytterbium is an alkaline-earth-like element from the lanthanide series on the periodic table. The particular isotope we use in all of our experiments is ^{174}Yb, a boson with no nuclear spin. This choice is excellent for us because a nuclear angular momentum and total electron angular momentum of zero means that this isotope is insensitive to magnetic fields in its ground state, resulting in a lack of fine and hyperfine structure. Pertinently this relieves us from the chore of building magnetic shielding to control external fields which would otherwise be a systematic in our interferometric measurements.

Isotope	Mass (u)	Abundance (%)	Nuclear spin
^{168}Yb	167.934	0.12	0
^{170}Yb	169.935	2.98	0
^{171}Yb	170.936	14.09	1/2
^{172}Yb	171.936	21.69	0
^{173}Yb	172.938	16.10	5/2
^{174}Yb	173.939	32.03	0
^{176}Yb	175.943	13.00	0

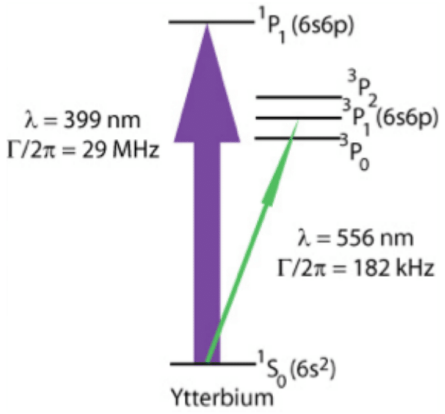

Figure 2.1: Table of ytterbium isotopes and level diagram for bosonic ytterbium, ^{174}Yb.

An additional benefit of using ^{174}Yb is that two closed cooling cycles are available at convenient optical transitions. The 399 nm ($^1S_0 \rightarrow {}^1P_1$) dipole transition has a broad linewidth of $\Gamma = 2\pi\times29$ MHz which makes it ideal for high photon scattering applications, such as Zeeman slowing and absorption imaging. The 556 nm ($^1S_0 \rightarrow {}^3P_1$) intercombination transition has a narrower linewidth, $\Gamma = 2\pi\times182$ kHz, making it useful for reaching low temperature MOTs due to the lowered Doppler limit [16, 42]. Also, the narrow linewidth puts large relative detunings within easy reach of acousto-optic modulators (AOMs) which is useful for low scattering applications like diffraction. Both of these transitions are accessible with commercially available tunable lasers.

Finally, the reasonable abundance of several different ytterbium isotopes allows us to measure the systematic effect of atomic interactions in our precision experiment by switching isotopes. Additionally, we have access to fermionic isotopes which enable new directions for experiments in spin-orbit coupling and multi-dimensional synthetic lattices.

2.2 Zeeman Slower

The first stage in cooling hot atoms towards quantum degeneracy is to slow them down enough to be captured in a trap. Our atom source is made by heating ytterbium to about

350°C then collimating the atoms into a beam aimed at our capture region. The atoms are slowed down by the scattering force from a counter-propagating 399 nm laser, which provides an average net force,

$$F_{\text{scatt}} = (\hbar k)\left(\frac{\Gamma}{2}\frac{s}{1+s+4\delta^2/\Gamma^2}\right), \tag{2.1}$$

equal to the photon momentum $\hbar k$ times the one-photon scattering rate. The spontaneous scattering rate is equal to $\Gamma\rho_{22}$ where ρ_{22} is the fraction of atoms in the excited state which, when solved for in the limit of many scattered photons [16], yields the form shown in Equation (2.1). The direction of emitted photons from each scattering event is random and averages to zero, so only the force from an equivalent number of absorbed photons adds constructively.

Although the scattering rate may be increased by raising the laser intensity ($s = I/I_{\text{sat}}$[1]), it becomes maximized when the laser is resonant with the atomic transition. The resonance condition is met when the detuning $\delta = \delta_{\text{lab}} + kv + \mu_B B/\hbar$ is equal to zero. In this expression kv represents the Doppler shift of a moving atom and $\mu_B B/\hbar$ allows for a compensation of this shift by means of the Zeeman effect. For an effective Zeeman slower the atoms are continuously being slowed, so a spatially varying magnetic field must be designed to correctly counter the Doppler effect at all times.

The design of the Zeeman slower was my first tangible contribution towards BEC production in our laboratory. Assuming a constant deceleration over the length of the slower, the magnetic field in an increasing-field slower should take the form

$$B(z) = B_{\max}\left(1 - \sqrt{1 - z/L}\right) \tag{2.2}$$

where L is the overall slower length. This design constrains the slowing laser frequency to be off-resonant at the capture region, which is less of a disturbance to the trapped atoms. To set the frequency even further from resonance in this region—and to increase the range of velocities addressed by the Zeeman slower[2]—we decided to add an offset to the magnetic

[1]The saturation intensity $I_{\text{sat}} = 60\,\text{mW/cm}^2$ and $0.14\,\text{mW/cm}^2$ for the 399 nm dipole transition and 556 nm intercombination transition, respectively.

[2]Ideally an offset field would not cause this to occur; however, in practice this effect comes from the gradual field growth and the off-resonant slowing in the region before the slower.

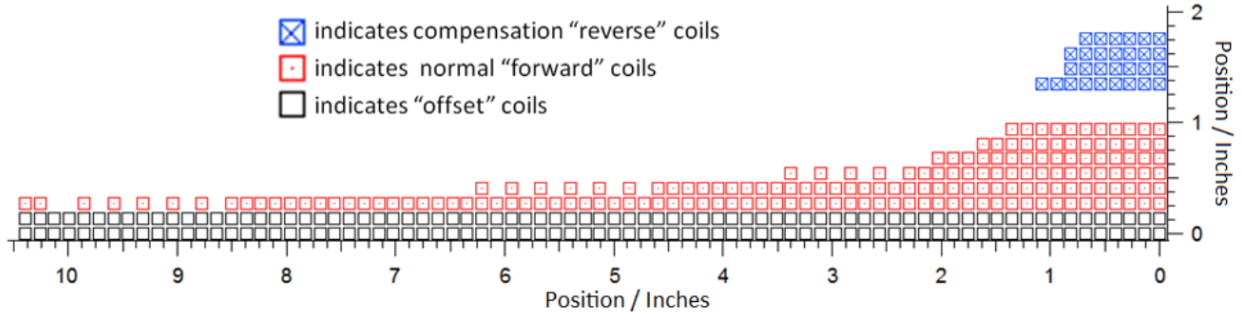

Figure 2.2: Radial cross-section schematic of the final design for the Zeeman slower. In relation to the experiment, atoms would propagate from left to right. Also note that the position on the y-axis is the location relative to the surface of the pipe ($\varnothing 1''$) which the wire was wound around. The reverse coils (blue) are wound with opposite handedness in comparison to the forward (red) and offset (black) coils.

field from Eqn. (2.2). This allowed for a larger laser detuning that would be resonant with atoms in the region before the slower, thereby extending our range of addressable velocities while performing additional slowing in an otherwise inaccessible region.

Optimization of the field shape was performed in Mathematica and aimed to achieve good agreement with the ideal function form while simultaneously having zero field or gradient (i.e. $B = 0$ and $\frac{\partial B_z}{\partial z} = 0$) at the location of the optical trap (so the atoms would be undisturbed by the continuous current).

2.2.1 Winding the Coils

The optimized magnetic field shape was calculated and obtained approximately by wrapping square hollow-core wire around a $\varnothing 1''$ brass pipe in a configuration according to Figure 2.2. The wire used was chosen for its high conductivity, its water-cooling capabilities, its robust thermal insulation, and its unique geometric shape ($^1/_8''$ square copper cross-section with $^1/_{16}''$ square hole cross-section for water flow). In particular the square wire allowed us to more easily pack the coils tightly together.

For additional information on the coil-winding process see [28]. In preparation for wind-

ing the magnetic coils, an aluminum disk was machined to fit over the brass pipe and act as a backstop. Both the pipe and the backstop were then covered with Kapton, a high-temperature insulator, to ensure the wire never shorts to the vacuum chamber. The entire assembly was put on a lathe where the spindle could be rotated by hand as the wire was wound onto the pipe. Prior experience also directed us to fashion a guide for the wire by cutting a square track through a pair of wooden blocks; this served to keep the wire from twisting while also maintaining a enough tension to prevent the wire from unwinding. The guide was placed in the tool holder on the lathe, which allowed us to use an auto-feed feature that would move the guide an axial distance proportional to the angular rotation as we turned the spindle.

There were several physical constraints that dictated how we grouped the coils: (i) a single length of wire should not be so long as to have significant electrical resistance or reduce coolant flow; (ii) the use of an aluminum backstop required that all leads extend from the opposite side (left side in Fig. 2.2); and (iii) to adhere to the design and thus achieve an optimal magnetic field, leads had to be included where it was infeasible to otherwise have continuity between layers (e.g. in Fig. 2.2, between layers 3 and 4 or layers 4 and 5). Abiding by these rules, we settled on the following arrangement. The offset coils were wound as a single wire. The forward coils were subdivided into two groups: layers 3 to 4 and layers 5 to 8. Two layers of wire filled the gap to support the reverse coils, which were wound as another single group. (Although these filler coils serve no purpose electrically, we will still include them in the water cooling circuit to assist in keeping the adjacent active coils at low temperature.) All four layers of reverse coils were wound together as the final group.

All wire leads were cut to about 1 meter in length[3] and the lead beginning each set was held with a hose clamp to keep from slipping, using ample protection to prevent damage of the wire insulation and taking care not to bend the wire too severely lest the hollow core

[3]This length ended up being sufficient, but just barely. It can be seen in Fig. 2.3 that the shortest lead only made it to the top of the water cooling panel and the remaining distance to the manifold had to be bridged with excess tubing. In future undertakings, it would be advisable to cut even longer leads.

become pinched. Thermally conductive epoxy was applied periodically throughout the entire winding process, and then applied liberally again at the end. After everything was dry, the aluminum backstop was removed and the wires were checked to ensure that there were no electrical shorts or constricted waterlines. The resistance of each was measured to be $< 0.3\Omega$, which is approximately the sensitivity limit of the ohmmeter used.

2.2.2 Water Cooling

The water cooling panel was designed with an overabundance of valves, both as a safety measure and to allow channel partitioning for easier flow diagnostics. Nearly all of the coolant is directed through $^1/_4''$ clear tubing (easier to see obstructions) with various ferrule-based or NPT-threaded Swagelock connections. All of these connectors, valves, manifolds, etc. are made of brass—this was much later discovered to be an unintended feature, after learning that the aluminum manifolds were corroding and forming particulates in the water cooling system in our neighboring lab.

A homemade two-component coupler was built to interface the electrical circuit with the cooling liquid circuit. The design is modeled after the couplers used in the aforementioned neighboring lab, described in [28] and visible in Fig. 2.3. The first component is a copper block machined with a square grove to make contact with three sides of the hollow core wire and a round hole for No. 4 AWG wire which is used for the remainder of the electronic circuit. A set screw holds this wire in place while the square wire is clamped between the block and a clear plastic panel. The second coupling component is a modified Swagelock terminator, cut with a square hole on the end cap and brazed onto the hollow wire.

The coolant is sourced from the building's chilled water system, as opposed to the standard building water supply. Not only is this water colder, but it is also contained in a closed loop which decreases the likelihood of foreign particles entering the system and clogging the hollow-core wires. The chilled water loop has a typical pressure of 45 PSI at the front end of our cooling panel. Note there is also about 10 PSI of pressure at the back end, which may be useful if the system ever needs flushed out in the reverse direction.

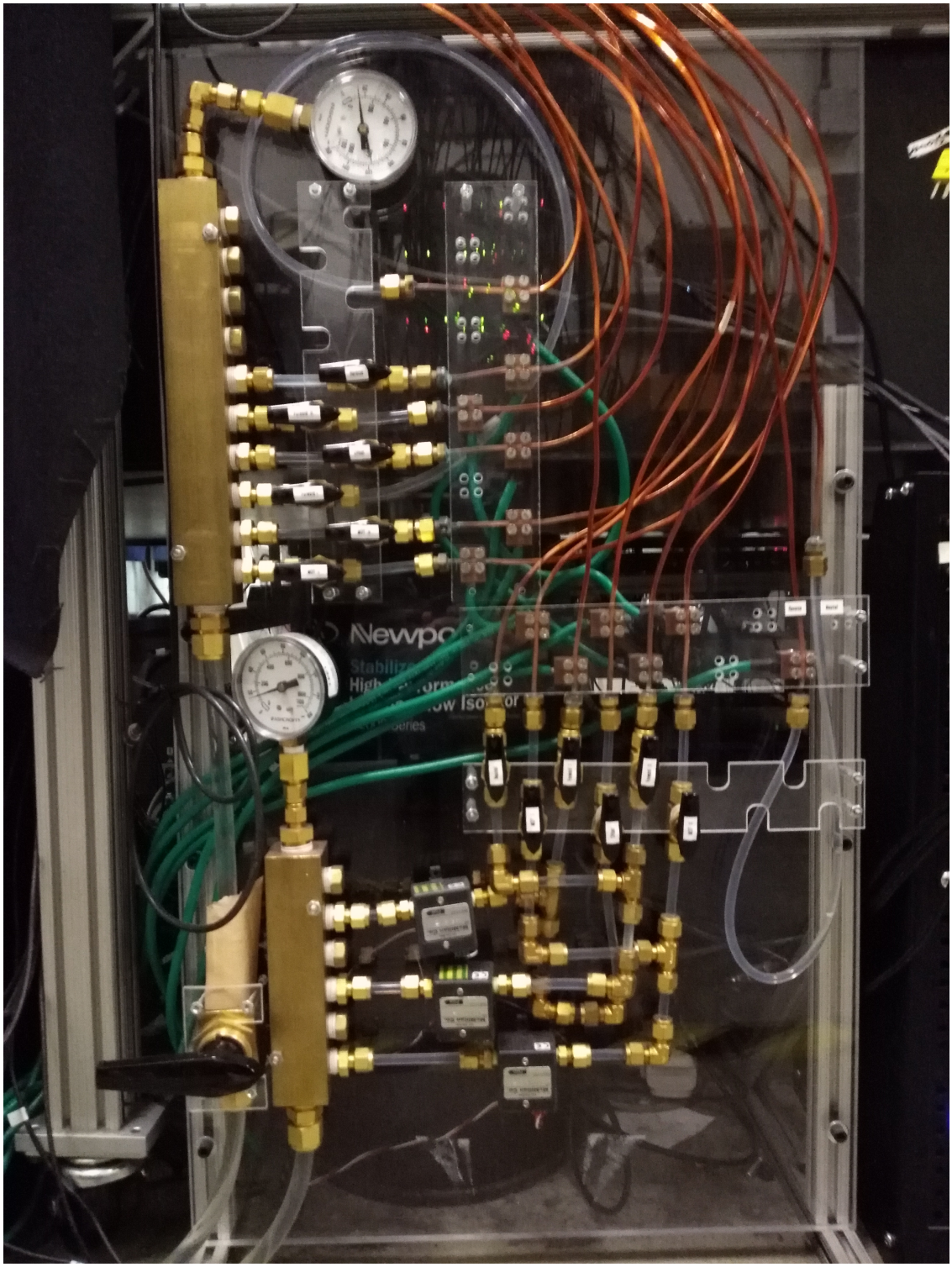

Figure 2.3: Photo of the water cooling control panel and coupling to hollow-core wires for the magnetic coils. Water flows in through the master valve into the large manifold on the left and out from the lower, smaller manifold on the right.

2.2.3 Interlock System

Incorporated into the water panel are three McMillan 101-M002 flowmeters for measuring the water flow through our cooling system. If there is ever a blockage preventing cooling of the electromagnetic wires, we would like to have an interlock in place to automatically shut off the current and prevent overheating. These flowmeters output a voltage proportional to the flow rate and pass that information to such an interlock. Each interlock circuit consists primarily of (i) a comparator to check the flowmeter voltage against an adjustable setpoint value, (ii) a Crydom MOSFET to stop the current to the coils when the flow rate drops below the setpoint, and (iii) a bi-color LED to visually indicate with green/red when the rate is above/below the setpoint.

The three channels of the interlock are for controlling the offset, slower, and MOT coils. The forward and reverse coils of the slower had been optimized with the same current and therefore share a single current supply. However, putting the entire Zeeman slower on a single water line would not permit a high enough flow rate for sufficient cooling, so the separate coil windings were broken up and organized as follows. The flow through the forward coils is split into two water lines which fully control the slower interlock. The flow through the offset and reverse coils together regulate the offset interlock, although the reverse coil current is still managed by the slower interlock. The MOT coils, which are used to make a magnetic field gradient for the magneto-optic trap (described later in this chapter), are completely separate from the other two channels.

2.2.4 High Power Nichia Diode

The optics for the Zeeman slowing laser source are described in [53], much of which remains unchanged. One notable improvement, however, is that the injection diode for main slowing beam has been upgraded. Sometime near the end of 2019 we began to be unsatisfied with the power and shape of our slower beam, which came from an injection-locked ThorLabs diode, ML320G2. Fortunately we had on-hand a spare high-power Nichia diode, NDV4B16,

which we tested and deemed a suitable replacement.

The old diode was rated for a power output of 120 mW while the new diode is rated at 300 mW, so we initially hoped for a 2.5× improvement; however, we found that we could not get improvement of this magnitude. Despite both diodes having a nominal central wavelength of 405 nm, the Nichia diode is actually farther from the desired 399 nm than the old diode[4]. This difference means that we need to cool our new diode more—to 12.5°C in comparison to 19°C prior—but nonetheless the power output at 399 nm is much less than the 300 mW free-running output. To keep a clean injection we decided to operate at power only slightly higher than the old diode, but the beam shape is now much better as well.

2.2.5 Crossed-beam

Ben Plotkin-Swing pioneered the technique of crossed beam slowing [53, 55] which has since been utilized in other experiments [38, 60] with great success. This method was developed as a simplified modification to the core-shell MOT [37]. It was only until recently, however, that we have endeavored to fully optimize and characterize the effectiveness of crossed-beam slowing within our apparatus.

Briefly, this technique seeks to improve the loading rate of the magneto-optic trap (MOT), and thereby increase the number of atoms available for use in an experiment. For certain atoms with a broad dipole transition and narrow intercombination transition[5], it is typical to use the broad line for slowing and the narrow line for trapping in a MOT. One major limitation of this arrangement is the low MOT capture velocity, since the laser cooling force is proportional to the linewidth. The core-shell MOT mitigates this by surrounding the usual narrow line MOT with trapping beams using the broad transition. The crossed beam

[4]ThorLabs used to quality check their diodes and wavelength select for customers those which were farthest below the nominal 405 nm, sometimes as low as 400 nm. This was our old ML320G2. They no longer perform this service, however, so all of our newer diodes have central wavelengths between 402 and 406 nm.

[5]Specifically, for atoms in which the velocity distribution width after the Zeeman slower, $\Delta v \approx \Gamma_{\text{broad}}/k_B$, is not too much greater than the capture velocity of the narrow-line MOT.

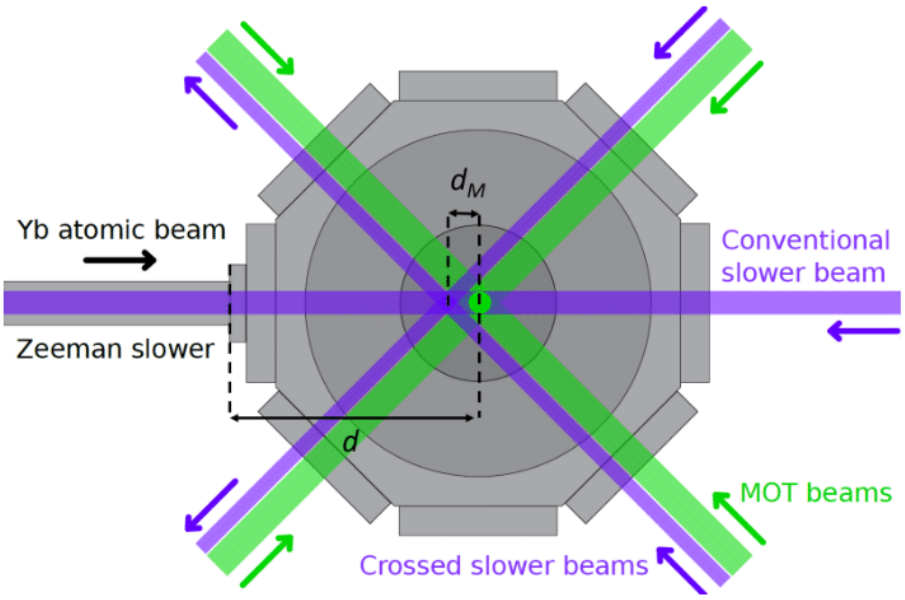

Figure 2.4: Crossed beam slower configuration. The crossed slower beams are set as close to the MOT beams as possible without disturbing the MOT itself, resulting in $d_M \approx 1$ cm. The distance from the end of the Zeeman slower coils to the MOT center is $d \approx 10$ cm.

configuration effectively raises the capture velocity in the same manner, but only using beams located on the front side of the MOT (see Fig. 2.4).

Increasing the capture velocity will lead to a direct increase in the loading of atoms; however, a subtle secondary benefit is that the atom velocity out of the Zeeman slower may be manipulated to decrease the "blooming" effect. This occurrence stems from nonzero transverse velocities which cause the atoms to spread out as they travel from the Zeeman slower to the MOT. This effect is exacerbated by minimizing the longitudinal velocity out of the slower—incidentally the very goal during that slowing stage. By optimizing the Zeeman slower current together with the crossed beam power, as shown in Fig. 2.5, we can find the best improvement to MOT loading rate in our apparatus.

The effectiveness of this design may be slightly less, but is significantly easier to implement, than the core-shell MOT because (i) fewer beams are needed, (ii) the beam placement

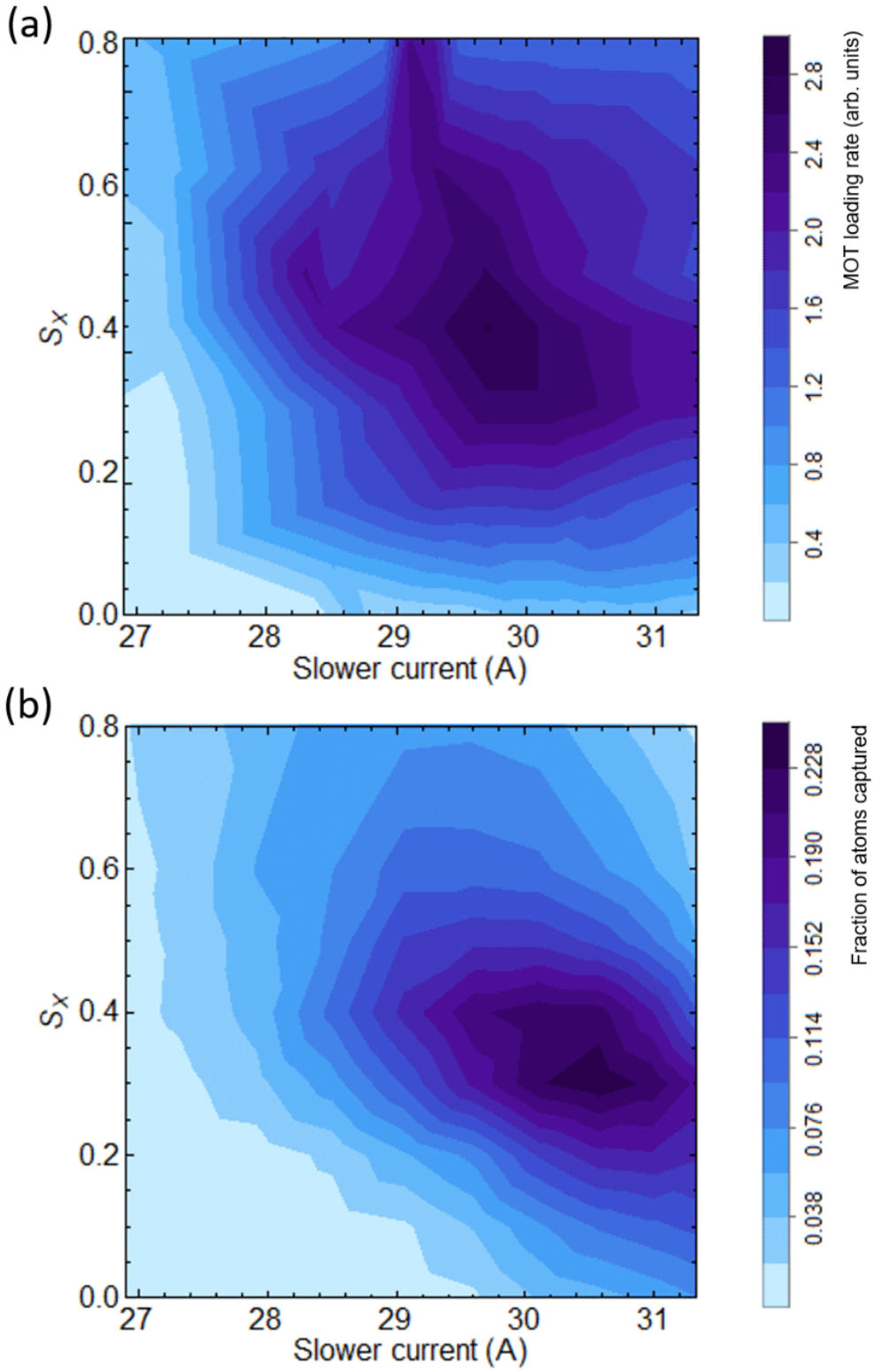

Figure 2.5: Optimization of crossed-beam cooling parameters. (a) MOT fluorescence at various Zeeman slower currents and crossed-beam intensities. (b) Simulated results for the fraction of atoms exiting the Zeeman slower which are captured by the MOT.

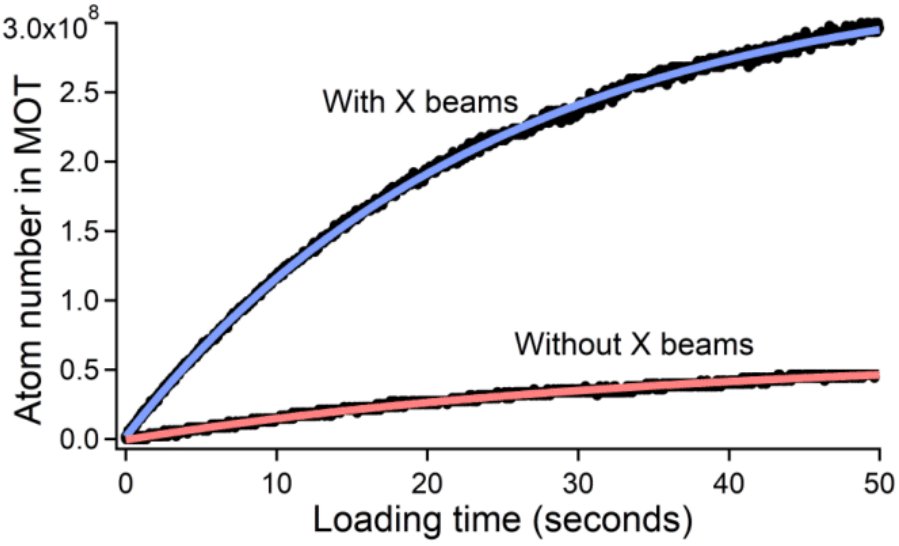

Figure 2.6: Loading rates measured by MOT fluorescence. The data (black) are fit to exponential loading curves for optimized arrangements with crossed beams (blue) and without crossed beams (red). The loading rates are given by the initial slopes which are different by a factor of 6.

is more forgiving, (iii) expensive dichroic polarization optics are not required, and (iv) there is no need to match magnetic field gradients between MOT layers. We have demonstrated a factor of 6 improvement in atom number after optimization of the crossed-beam cooling parameters.

2.3 Optical Trapping

Now that we have developed a slowing mechanism, the next stage towards ultracold atom production is capturing the atoms in an optical trap where they may be contained and further cooled. Generally the first stage of trapping is done with a magneto-optic trap, as alluded to in the previous sections; however, this trap alone is not able to reach temperatures low enough to obtain BECs. The final stage of cooling is typically performed by evaporation in either a magnetic trap or an optical dipole trap. Because ground state ytterbium is insensitive to magnetic fields, we use an optical trap to reach quantum degeneracy.

2.3.1 Magneto-Optic Trap

A mangneto-optic trap (MOT) manipulates atoms with the same scattering force used for slowing (Eqn. (2.1)) but acts in all directions with a configuration of six orthogonal laser beams. It is important to note that alone the MOT beams provide only a dissipative force ($F = -\alpha v$), but with the addition of a magnetic field gradient an accompanying restorative force ($F = -\beta x$) spatially contains the atoms. The MOT coils were wound using the same technique described above in Section 2.2.1, then placed around the main vacuum chamber in anti-Helmholtz configuration. The actual magnetic field gradient generated is variable during MOT production, but exhibits 0.64 G/cm per amp provided by the current source.

The Doppler-limited temperature attainable in a MOT is achieved under the condition $s \ll 1$ and is given by $T_D = \hbar\Gamma/(2k_B)$ where k_B is the Boltzmann constant. This is proportional to the linewidth of the cooling transition, Γ, which is why MOTs are typically made using a narrow-line transition—to more easily reach lower temperatures. For ^{174}Yb the intercombination line at 556 nm has a width of $2\pi \times 182$ kHz and a MOT using this transition has a Doppler temperature of 4.4 μK. In practice, however, we only achieve MOT temperatures as low as $\approx 30\,\mu$K.

2.3.2 Optical Dipole Trap

To cool beyond the Doppler limit we load the atoms into an optical dipole trap (ODT) where we perform evaporative cooling. Like the scattering force applied in MOTs, the dipole force used in ODTs is well-understood and a meticulous derivation can be found in Section 9.6 of [16], an excellent reference for general atomic physics. By rearranging Eqn. (9.43) of [16] to look more like our Eqn. (2.1), we obtain

$$F_{\text{dipole}} = -\frac{\hbar\delta}{2}\left(\frac{\partial s/\partial z}{1 + s + 4\delta^2/\Gamma^2}\right) \tag{2.3}$$

is proportional to the laser intensity gradient (recall $s = I/I_{\text{sat}}$), where δ is the single-photon detuning. Unlike the MOT, the ODT can be treated as a conservative trapping potential,

and in the limit of large detuning we find

$$U_{\text{dipole}} \simeq \frac{\hbar\Gamma^2}{8\delta}\frac{I}{I_{\text{sat}}}\,. \tag{2.4}$$

In this type of trap it is undesirable to have resonant scattering as it would be counterproductive to the cooling process. When comparing U_{dipole} to the scattering rate ($R_{\text{scatt}} \simeq \frac{\Gamma^2}{8\delta^2}\frac{I}{I_{\text{sat}}}$ from Eqn. (2.1) in the high-detuning limit) one can see a benefit from operating at as large of a detuning as possible, assuming enough laser power is available to maintain a sufficient ODT trap depth.

The evaporative process conducted within the ODT is similar to the everyday concept of evaporation—the hottest particles escape, resulting in an on-average colder sample. One key difference here is that the trap depth is lowered throughout the process, which leads to successively lower and lower temperatures as the atoms continue to evaporate.

We use an 18 W laser at 532 nm for our ODT. Following a set of AOMs for frequency and amplitude control, the total available power is closer to 12 W split between a vertical and horizontal trapping beam. In our most recent experiments, we have made use of a motorized waveplate rotation stage (RSC-103E by Pacific Laser Equipment) to allocate all of the power to the horizontal beam at the beginning of evaporation then transfer the unused power to the vertical beam at the end of the process. This serves to keep the atom density high enough for easier condensation (see next section).

Although our ODT beams have undergone several revisions since [53], they have generally maintained the same size specifications: approximately 20 μm horizontal beam waist and 60 μm vertical beam waist. The choice of waist size should be a balance between being large enough to capture a significant fraction of atoms from the MOT and small enough to sustain evaporation (e.g. with high densities and collision rates) even at low trap depths. It is now a standard technique in our lab to choose a small waist to satisfy the latter condition and dynamically "paint" the beam to satisfy the former.

This method of using AOMs for generating a time-averaged optical potential to increase the size of an ODT has been around for several decades [44, 18, 2, 29, 58, 57]; however, we have

recently been employing the technique for other purposes (e.g. reducing trap frequencies, compensating gravitational tilt). I will expand upon these applications shortly, in Section 2.5, but before increasing the trap size we must first utilize the small beam waist to obtain a Bose-Einstein condensate.

2.4 Bose-Einstein Condensates

The BEC state can be casually defined as the macroscopic population of a single quantum state. Bose-Einstein condensation will begin to occur at the critical temperature, which can be expressed as

$$T_C \approx \frac{\hbar^2 n^{2/3}}{m k_B} \tag{2.5}$$

where n is the particle density and m is the mass of a ^{174}Yb atom. As one can observe in this equation, it is important to maintain high density for condensation. This requirement is complemented with a need for sufficient collision rates for the continuation of evaporation. This is often achieved by making a small waist in the ODT beam.

In the context of atom interferometry, two desirable characteristics of a BEC are (i) the narrow momentum spread and (ii) the small spatial extent. Not only does the narrow momentum distribution increase the coherence length of the BEC—this is especially significant during momentum-dependent diffraction pulses—but it also means that the density of the cloud does not drop as severely after a long time of flight. This, coupled with the small initial size, means that the region of diffraction beams sampled by the BEC is small compared with the beam size and may be better approximated as plane waves.

The tiny ODT waist contributes greatly towards the small spatial extent, but due to interaction effects the atoms' momentum spread can not be made as narrow as we would like (ideally $\Delta v \ll v_{\text{rec}}$). Therefore after a sufficient fraction of atoms condense into the BEC state, we once again employ painting to widen the trap which lowers the density of atoms and consequently the momentum spread. The widened trap is often characterized by the trap frequency. For our early experiments, the trap frequencies at the end of evaporation

and repainting were measured to be $\omega_x = 2\pi \times 16\,\text{Hz}$, $\omega_y = 2\pi \times 200\,\text{Hz}$, and $\omega_z = 2\pi \times 80\,\text{Hz}$, resulting in an average $\bar{\omega} = 2\pi \times 63\,\text{Hz}$.

2.5 Gravity Compensation

Following BEC formation, we are able to prepare the atoms for optimal use in an interferometer. Although a condensate will already have a significantly reduced momentum spread in comparison with a thermal cloud, it can be narrowed even further by continuing to lower the trap frequencies. One option is to simply reduce the ODT power, as done during evaporation, but this eventually becomes limited by the trap's ability to contain the atoms against the force of gravity. We have employed two means of reducing the trap frequency past this point, both of which rely on painting.

The first method we tried had been well-established, using painting to increase the trap volume while maintaining the depth by increasing the beam power. Painting with a triangle waveform will create a roughly flat-bottomed time-averaged potential which should most dramatically reduce the trap frequency. If there is concern that the harmonic trap approximation will break down, then one can paint with a unique arbitrary waveform to generate a parabolic time-averaged potential (as shown in [57]). It is important to note that the painting frequency must always be much higher than the trap frequency for the dynamic trap to act as a time-averaged potential.

For all of our experiments prior to those involving vertical interferometry, we painted our ODT in the horizontal plane. In these experiments the dimension with the highest trap frequency, and thereby the largest momentum spread, was that along the direction of gravity. When we began rearranging our optics to comply with vertical diffraction requirements, we realized that this dimension was actually the one to optimize such that we could obtain the strongest interferometer signals. This eventually proved to be an incredible technical challenge, due especially to the fact that ground-state ytterbium (a Group II atom) is insensitive to magnetic fields[6].

[6]For typical vertical atom interferometers a magnetically sensitive atom is used. This allows the use of a

2.5.1 Polarization Constraints

There were several difficulties in implementing painting along the vertical direction, the first of which was related to the laser polarization. I determined that the simplest means for changing the painting orientation would be to rotate the periscope (as opposed to rotating the AOM) which brings the horizontal ODT beam up to the level of the main chamber. While this did succeed in painting along the correct axis, the incidental rotation of the polarization negatively impacted us in multiple ways: (i) the beam-sampling optic used for feedback control is polarization dependent and no longer provided sufficient power, (ii) the leakage through the final mirror before the beam dump became dangerously high, and (iii) the two ODT beams then shared polarization axes which would cause the undesired formation of a lattice, albeit a very fast-moving one. Needless to say, I simply added a half-waveplate to correct the issues; however, these points should all be considered in the case of any similar future scenarios.

2.5.2 Painting Waveform

The remainder of our journey towards painting along the direction of gravity was unexpectedly arduous and time-consuming. Initially painting was done using the simple triangle waveform with which we were able to reach kinetic temperatures[7] of approximately 20 nK. This corresponds to a velocity distribution width on the order of $^1/_4\, v_{\mathrm{rec}}$ which is inadequate for efficient Bragg diffraction. Furthermore, this limitation was likely due to the fact that the flat bottom of our painted potential becomes tilted with the addition of gravity. We wanted to increase the width of our trap—a proxy for trap frequency—to reduce the temperature;

---

magnetic field gradient to cancel the background linear potential due to gravity, thus lifting the constraint on the ODT size which otherwise results in the undesired large velocity spread. In this section we will discuss several similar methods for gravity compensation within the ODT, but further success will be found in an alternative dynamic cooling technique (see Section 6.2)

[7]While not entirely accurate, the term temperature here still describes the expansion rate (i.e. momentum distribution) of the BEC but only along a particular direction, since the cloud will not expand isotropically like a thermal gas.

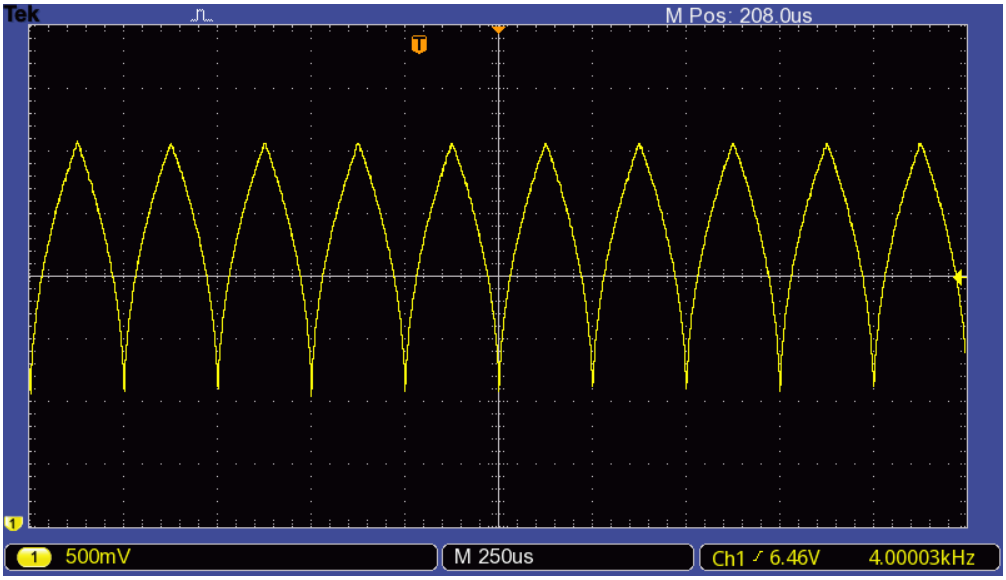

Figure 2.7: Painting waveform for ODT gravity compensation. The settings used here are consistent with the requirements of the secondary beam employed solely for gravity compensation (see Section 2.5.3).

however, the width was limited to $U_0/(mg)$ which could only be increased at the cost of raising the trap depth, U_0, but this would in turn heat the atoms instead.

The first attempt to solve this problem was with a modified painting waveform for generating a tilted potential. Then, with tuning of relevant parameters, the tilt could be adjusted to compensate for gravity. I set out to make a trapezoid-shaped trap to simultaneously hold atoms and cancel gravity. It would have width h, minimum intensity I_0, and an intensity gradient c which could be used to cancel the gravity potential gradient. To create a beam with this intensity profile, $I(x) = I_0 + cx$ where $0 < x < h$, following the procedure in the appendix of [57] yields the painting waveform

$$\xi(t) = \frac{I_0}{c}\left(-1 + \sqrt{1 + \frac{2c}{I_0}\frac{\omega}{\pi}\left(\frac{c}{2I_0}h^2 + h\right)t}\right) \tag{2.6}$$

in which $\xi(t)$ is the positional displacement of the painted beam, ω is the angular painting frequency, and t is defined over one half-period. The second half-period will be the reverse waveform to minimize electronic attenuation as well as appeal to symmetry (see Fig. 2.7).

With this we were able to paint the ODT into the shape we desired; however, problems continued to abound. The BEC temperature in the vertical dimension remained limited to 20 nK. The ODT beam power was dynamically controllable, but painted beam size and intensity gradient were not; this meant that it was impossible to maintain both gravity compensation and low trap depth throughout the adiabatic enactment of painting.

2.5.3 Anti-gravity Beam

Next we decided to attempt gravity compensation using another beam, separate from the ODT, to provide the linear optical potential while the ODT alone would provide the trapping force. We were reluctant to try this at first, because it would require significant modifictations to the existing ODT optics. Incidentally, it was around this same time that we learned of another experimental group that had recently demonstrated exactly what we were trying to achieve [61]. With reassurance that this could be the key to success, we began adding optics for what would be known as the anti-gravity beam (AGB).

The 532 nm laser power is already fully divided between the two existing ODT beams, so we utilized the unused zero-order light from the vertical beam AOM for the AGB. The AGB light passes through a 200 MHz AOM (in contrast with the 80 MHz ODT AOMs) and is aligned onto the path of the horizontal ODT beam with a polarizing beam splitter. This keeps the beams at different frequencies and polarizations to prevent them from forming any undesired lattices. The painting waveform for the AGB is obtained by reducing Eqn. (2.6) in the limit of $I_0 = 0$.

$$\xi(t) = h\sqrt{\frac{\omega}{\pi}t} \tag{2.7}$$

where $0 < t < \pi$ as before. The painting frequency, ω, should be chosen to be simultaneously larger than the ODT trap frequency and lower than the bandwidth of the RF driver electronics (to avoid attenuation and thereby a misshapen waveform). After optimization of our AGB we chose to operate with a painting frequency of 4 kHz.

Optimization of the AGB was performed using two approaches, both of which leave the

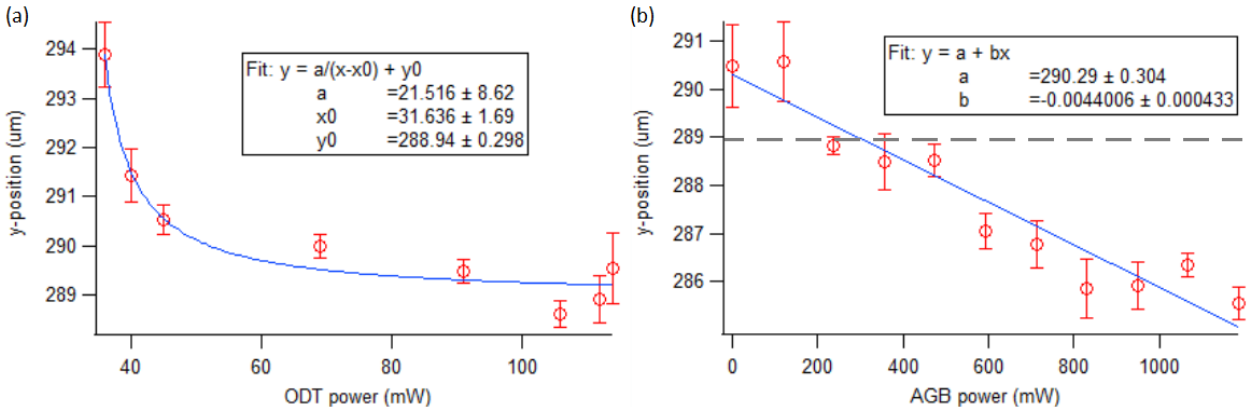

Figure 2.8: Achieving gravity compensation in the ODT with use of a secondary anti-gravity beam. (a) Measured BEC position in the trap with no AGB. At higher powers the gravitational sag becomes negligible and can be approximated as the true center of the trap. (b) The BEC position shifts linearly with the strength of the AGB potential, an effect that is more visible at the lowest possible ODT power. The horizontal dashed line represents position corresponding to the asymptote of the fit from part (a), at which point gravity has been precisely canceled by the AGB.

painted width, h, fixed and only vary the total AGB power. The first (shown in Fig. 2.8) was based on the concept of gravitational sag: the background linear potential shifts the center position of a bound state in a trapping potential. The total tilt of the linear potential can be adjusted with the AGB power, resulting in a linear shift to the BEC position (as expected from the dipole interaction in Eqn. (2.4)). This method enables us to determine the true trap center at high ODT power as well as optimize the AGB for gravity cancellation at low ODT power.

The second, less rigorous, method performed was simply to vary AGB power and minimize the BEC temperature. Final optimization of the AGB using both of these techniques yielded temperatures as low as 20 nK along the direction of gravity. While I would prefer even lower temperatures—we had observed 1 nK in dimensions orthogonal to gravity—this was deemed adequate[8] and we continued with setting up the vertical diffraction optics.

[8]We eventually further improved upon this temperature with the delta-kick cooling technique, described in detail in Section 6.2

Chapter 3

ATOM OPTICS CONTROL

3.1 Diffraction Beams

As detailed in Ben's thesis [53], the placement of our diffraction beam optics went through multiple iterations before settling on our final arrangement for the horizontal optical lattice. Much of the data I will present later was obtained using this horizontal geometry; however, we eventually reoriented our optical lattice along the direction of gravity so that we could extend our interrogation times in a vertical interferometer.

The frequency control of our lattice beams is managed prior to coupling through a fiber and therefore common to both of the aforementioned lattice orientations. A pair of 200 MHz acousto-optic modulators (AOMs) are used to set the detuning of the lattice, as well as to manipulate the lattice depth through controlling the amplitude of applied RF power. For each of our experiments using the horizontal lattice, the diffraction beams were detuned from the 556 nm intercombination transition ($^1S_0 \rightarrow {}^3P_1$) by $+3500\Gamma$ or $+1300\Gamma$ and this value is noted with each data set presented. This frequency shift was obtained by taking either the $+1$ or -1 order from a single pass of an AOM, then coupling that light into a polarization-maintaining (PM) fiber. The fiber output couplers were chosen from the ThorLabs line of triplet collimators, designed to produce well-collimated beams of a specified waist size. Our diffraction beams produced with these optics have waist of 1.8 mm.

The exact arrangement of optics following the output couplers differed between our horizontal and vertical setups but both configurations included a few common components: a linear polarizer, a beam sampler, and a feedback photodiode. Despite using a PM fiber, we wanted to ensure that the relative polarization of the two lattice beams was as stable as

possible. To this end we included a linear polarizer (i.e. polarizing beam-splitting cube[1]) to clean up any polarization noise and turn it into intensity noise which could be subsequently removed with our feedback control system. Therefore, immediately after the cube we placed a beam sampler—a low reflectance optic with minimal polarization dependence—which directed a pickoff of the diffraction beam into the feedback photodiode for stabilization.

3.1.1 Amplitude Control

The depth of our optical lattice is controlled directly with an AD8368, a variable gain amplifier (VGA) from Analog Devices, for adjusting the RF power and thereby the efficiency of the AOM. This VGA was chosen over our usual choice of variable voltage attenuator, ZX73-2500+, because it satisfies the requirement for our diffraction pulses to operate faster than 100 μs. The VGA is itself managed by the output of a feedback control system. The feedback electronics (Fig. 3.1) consist primarily of a comparator taking the difference between the feedback photodiode voltage and an externally provided setpoint, and then feeding that into an integrator to correct for that difference over some characteristic time[2].

The bandwidth of the feedback circuit is limited by the integrator components, which had to be selected carefully to maximize the speed of our feedback while avoiding resonant ringing at high frequencies. In our homemade circuit board, we obtained a bandwidth of approximately 100 kHz and avoided ringing by operating at sufficiently low setpoint and photodiode voltages. This was made easier with the ability to adjust the gain on our ThorLabs switchable gain Si Amplified Photodetectors, as well as using optical filtering elements to further control the voltage entering the feedback circuit.

The actual setpoint controlling the diffraction beam amplitude is managed within our timing software, Cicero. In conjunction with the analog output for pulse shaping, Cicero also

[1]For the vertical contrast interferometer, the alternate port on this cube was also available to use for the readout beam and photon collection for a contrast interferometer signal.

[2]These are the same feedback control circuits used to stabilize the MOT, ODT, and AGB. Amplitude stabilization is reliable to the percent level.

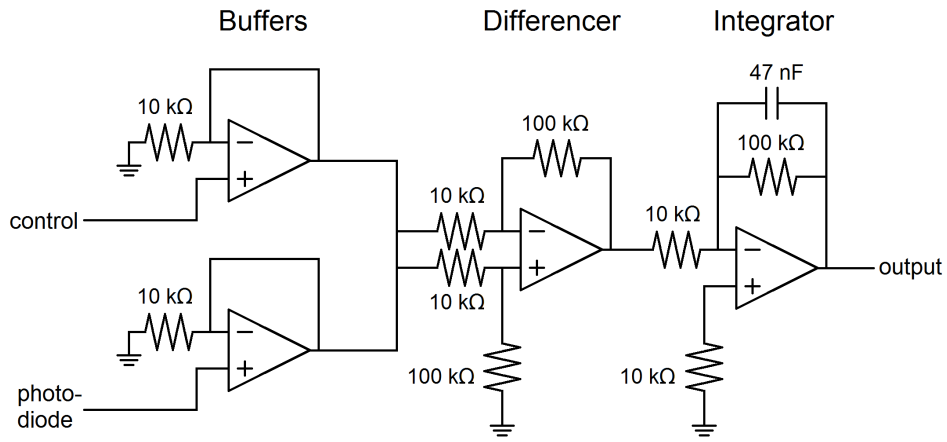

Figure 3.1: Schematic for our feedback electronics, composed of op-amp buffer circuits followed by a comparator and integrator. Component values shown are those chosen for the MOT feedback, but these were tailored individually for each system, since some require much faster response times (e.g. diffraction/lattice beam feedback) but less long-term stability.

uses a digital output to turn the diffraction beams on and off. When setting up the vertical contrast interferometer, we incidentally discovered with our readout collection optics that the diffraction AOMs were still outputting a small amount of light (e.g. a few nanoWatts) even when everything was nominally off. This led to the installation of a Crydom MOSFET switch in addition to the usual RF switch to ensure that we can achieve absolutely zero lattice light when desired.

3.1.2 Horizontal to Vertical Lattice

The two diffraction beams are positioned to enter the main chamber through opposite viewports such that they form a single 1-dimensional optical lattice. This counter-propagating configuration is described in Ben's thesis [53] and the placement of optics is unimpeded when aligning the lattice horizontally. For a vertical alignment, however, the optical access has to be shared with both the MOT and readout collection optics. The first key for this development was to install electro-mechanical flipper mirrors to enable the MOT when lowered, then to move aside and allow access to the diffraction and readout beams. Also, I believe

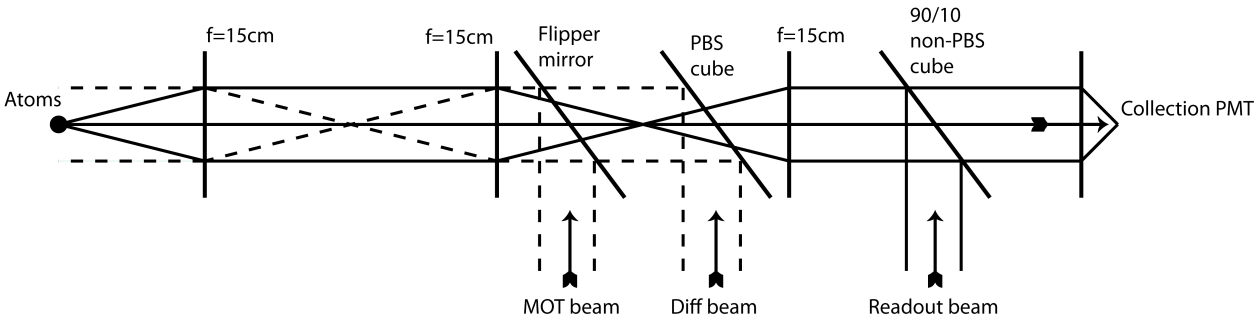

Figure 3.2: Key elements for arranging the MOT, diffraction, and readout optics all along a shared vertical axis (neglecting mirrors) during initial installation of the vertical lattice. In this figure at the atoms gravity points to the right. A more detailed configuration of the readout optics will be supplied in Section 6.4.1, along with an update to the readout beam characteristics (e.g. spot size, divergence angle) upon incidence on the 90/10 beamsplitting cube which were later found to be more suitable.

it is important that these flipper mounts contain MOT optics rather than diffraction optics, since the MOT alignment is much more forgiving of imperfect repeatability of the flippers.

3.1.3 Alignment Procedures

For both horizontal and vertical optical lattice arrangements, the task of aligning the diffraction beams to the atoms begins with resonant blasting. This process involves using a picked off bit of MOT light (before the shutter) which can be directed into a diffraction fiber with a manually operated mechanical flipper mirror. Initial alignment to the atoms is optimized by maximizing the heating of the atom cloud; final alignment is done by maximizing the diffraction observed following a Kapitza-Dirac pulse. The two lattice beams can then be aligned to each other by optimizing the light passing backwards through the opposite fiber.

Vertical interferometry includes an additional requirement that the optical lattice be as closely aligned along the direction of gravity as possible. To this end we installed three tall pedestals under the main chamber to allow easy placement of a water-filled "bowl" attached to a cardboard sheet. The water serves as a reflective surface perpendicular to the direction of gravity; therefore, with the help of an iris one can achieve rather good vertical alignment

for the optical lattice. Iterations between this and the other alignment techniques ensure that the lattice is optimally aligned to both the atoms and the direction of gravity.

3.2 Direct Digital Synthesis

The prevalence of acousto-optic modulators (AOMs) in the field of atomic physics implies that there is also a high demand for function generators capable of supplying the RF frequencies required for driving the AOMs. Commercially available function generators may be the instinctual choice, as they are the best option in terms of simplicity and user interaction design; however, they are also often expensive and sometimes lack the specific control options necessary for a particular experiment. For this reason it is quite common in laboratories such as ours to construct our own RF drivers. A majority of these drivers in our lab are made with analog components: a voltage-controlled oscillator (VCO), an RF switch, and a variable-voltage attenuator (VVA). The frequency and amplitude of the output waveform can be controlled through applying an analog voltage to the VCO and VVA, respectively. Furthermore, for dynamic control of frequency and amplitude during the experiment, we supply these analog control voltages using a set of National Instruments PCI 6713 cards powered via our sequence timing software, Cicero. This is entirely sufficient for the control of most of our AOMs, but the 2 μs timebase of Cicero and the 10 kHz frequency stability of the VCOs do not meet the requirements[3] for diffraction experiments. To achieve this end we ventured into the realm of digital waveform generation.

3.2.1 DDS Technology

Direct digital synthesis (DDS) is a method of producing an analog waveform with a system of digital components. Due to the nature of digital electronics, DDS RF drivers often have several features unavailable to analog VCOs: programming, repeatability, and synchronization. Additionally, the frequency resolution and phase stability are limited solely by the

[3]For a typical third-order Bragg π–pulse with Gaussian 1/e full-width 54 μs, the frequency stability should be much better than the corresponding Fourier width of the pulse, about $1/54\,\mu\text{s} \approx 18.5\,\text{kHz}$.

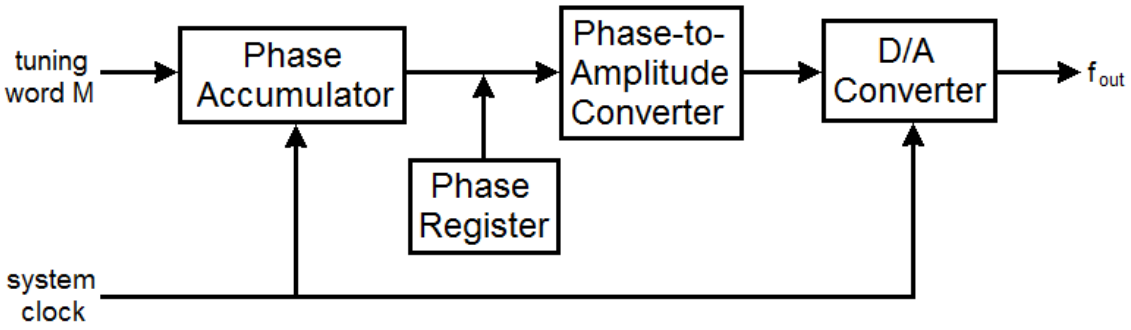

Figure 3.3: Block diagram for a typical DDS layout.

source clock running the device.

A complete DDS package is composed primarily of a phase accumulator, a sine look-up table, and a digital-to-analog converter (see Fig. 3.3). The phase accumulator will keep track of the waveform phase which, for a fixed frequency, should simply increment linearly in time. This phase updates once every cycle of the system clock by an amount dictated by the frequency tuning word (FTW). For a phase accumulator with a resolution of 2^N bits, the FTW can be written as $M = 2^N(f_{\text{out}}/f_{\text{sys}})$ where f_{sys} is the system clock frequency and f_{out} is the desired waveform frequency. This effect can be understood visually through the concept of a phase wheel. The accumulator step size determines the output frequency, and the larger the step size the higher the frequency. From this picture one can also see that the maximum output frequency is limited by the Nyquist theorem to approximately $f_{\text{sys}}/2$. Likely it is best to just use as fast of a system clock as possible, but this is still an important consideration when deciding the system clock frequency for our DDS because we don't want to limit our available frequency range.

Following the phase accumulator is some form of phase-to-amplitude conversion. This is typically a sine look-up table in which each phase value from 0 to (2^N-1) has a corresponding amplitude which is then output through the digital-to-analog converter (see Fig. 3.4). Note that DDS technology is not limited to purely sinusoidal outputs—some DDS devices have look-up tables for square- or triangle-wave outputs; however the general waveform shape

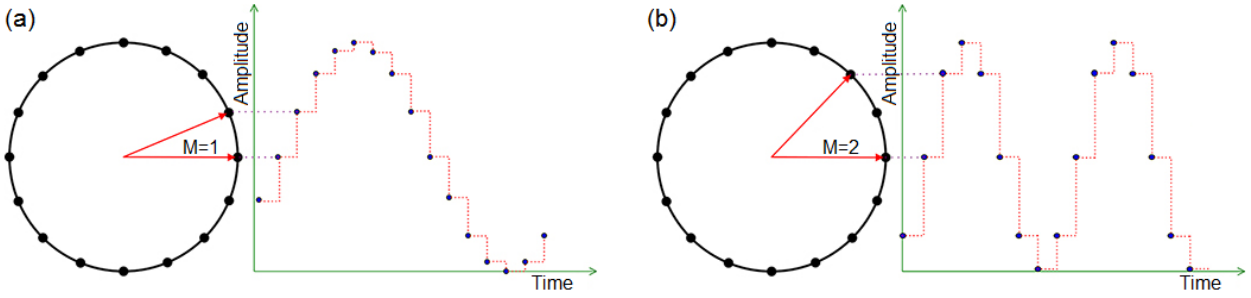

Figure 3.4: An example of a 4-bit phase accumulator with FTW equal to (a) one and (b) two as well as the corresponding output from a sinusoidal phase-to-amplitude converter and digital-to-analog converter.

must be decided upon prior to selecting a DDS as rewriting these look-up tables is not possible for the end user.

Finally, it typical that a DDS package with a sinusoidal output will include some passive filtering components to clean up the resultant waveform. Unfortunately digital-to-analog conversion may still lead to some spurious frequency components in addition to potential Nyquist image frequencies. A good DDS package will include further filtering (e.g. inverse sinc filter) to ensure a quality product.

3.2.2 AD9910

Based on our current and projected requirements for both frequency and timing, I decided that the Analog Devices AD9910 would be a suitable DDS. The AD9910 has a 32-bit phase accumulator and a 14-bit digital-to-analog converter. This means that for our diffraction AOMs with center frequency of 200 MHz we can expect to have frequency resolution below 50 mHz and amplitude control 100 times better than the ability of our feedback circuit. The system clock can run up to 1 GHz so our typical output will be sufficiently below the Nyquist limit, but the device has inverse sinc filtering to take care of this issue regardless. If lacking a source clock of 1 GHz, the AD9910 has a phase-locked loop circuit to multiply a lower frequency source up to any desired system clock frequency. This DDS allows independent

control of the frequency, amplitude, and phase through a large variety of control modes, not all of which we use in our lab. For amplitude control we use the OSK module. For frequency control we use the DRG and FTW profile modules. We do not have direct phase control implemented at this time.

Amplitude control through output shift keying (OSK) can be placed in either manual or automatic mode. In our configuration the default is manual mode, in which case it performs a function identical to an analog RF switch. This input is may be used for toggling between an "on" and "off" state, but continuous amplitude control is managed by a separate feedback circuit.

Our AD9910 devices are configured to allow two options for frequency control, but can only operate in one mode at a time[4]. If frequency ramping is required (e.g. for Bloch oscillations, gravity compensation) then the digital ramp generator (DRG) must be enabled; otherwise, it is often more convenient to use the discrete frequency profiles (e.g. for Bragg pulse sequences). The AD9910 can store up to eight pre-programmed frequency profiles in the form of FTWs, each of which may be accessed by a single 3-bit input derived from three of Cicero's digital channels. These profiles are ignored when the DRG is enabled, in which case the frequency may take on values between the programmed lower and upper limits. When the frequency ramp digital channel is set high (low) the frequency will step up (down) by the corresponding Δf in intervals Δt associated with the positive (negative) ramp, until it reaches the upper (lower) limit and stays at that value. A second digital channel may be used to hold the frequency at a value between the extreme limits; however, this value is obtained by correctly timing the holding trigger within a frequency ramp, rather than programming an exact frequency value. Therefore if this holding technique is used, more accurate results will be attainable with slower frequency ramps.

---

[4]Unlike the analog and digital channels in Cicero, the RS232 channels are not output with the reliable 2 μs timebase. Instead these commands sent to the Arduino for programming the DDS have a timing based on Windows software operations, which is unreliable to the 100 ms level. Therefore it may be useful to include the RS232 outputs in the beginning of an experimental sequence, but the DDS programming cannot be changed between diffraction pulses within the same sequence.

	DDS Signal Control Parameters					
	Frequency		Phase		Amplitude	
Priority	**Data Source**	**Conditions**	**Data Source**	**Conditions**	**Data Source**	**Conditions**
Highest Priority	RAM	RAM enabled and data destination is frequency	RAM	RAM enabled and data destination is phase or polar	OSK generator	OSK enabled (auto mode)
	DRG	DRG enabled and data destination is frequency	DRG	DRG enabled and data destination is phase	ASF register	OSK enabled (manual mode)
	Parallel data port and FTW register	Parallel data port enabled and data destination is frequency	Parallel data port	Parallel data port enabled and data destination is phase	RAM	RAM enabled and data destination is amplitude or polar
	FTW register	RAM enabled and data destination is phase, amplitude, or polar	Parallel data port concatenated with the POW register LSBs	Parallel data port enabled and data destination is polar	DRG	DRG enabled and data destination is amplitude
	FTW in active single tone profile register	DRG enabled and data destination is phase or amplitude	POW register	RAM enabled and destination is frequency or amplitude	Parallel data port	Parallel data port enabled and data destination is amplitude
	FTW in active single tone profile register	Parallel data port enabled and data destination is phase, amplitude, or polar	POW in active single tone profile register	DRG enabled and data destination is frequency or amplitude	Parallel data port concatenated with the ASF register LSBs	Parallel data port enabled and data destination is polar
	FTW in active single tone profile register	None	POW in active single tone profile register	Parallel data port enabled and data destination is frequency or amplitude	ASF in active single tone profile register	Enable amplitude scale from single tone profiles bit (CFR2[24]) set
Lowest Priority			POW in active single tone profile register	None	No amplitude scaling	None

Figure 3.5: Excerpt from page 21 of the AD9910 datasheet [3], showing mode priority for frequency, phase, and amplitude control of the AD9910. For frequency control we use DRG and FTW register, depending on whether we want to sweep or hop the DDS frequency. For amplitude control we use ASF register (OSK in manual mode).

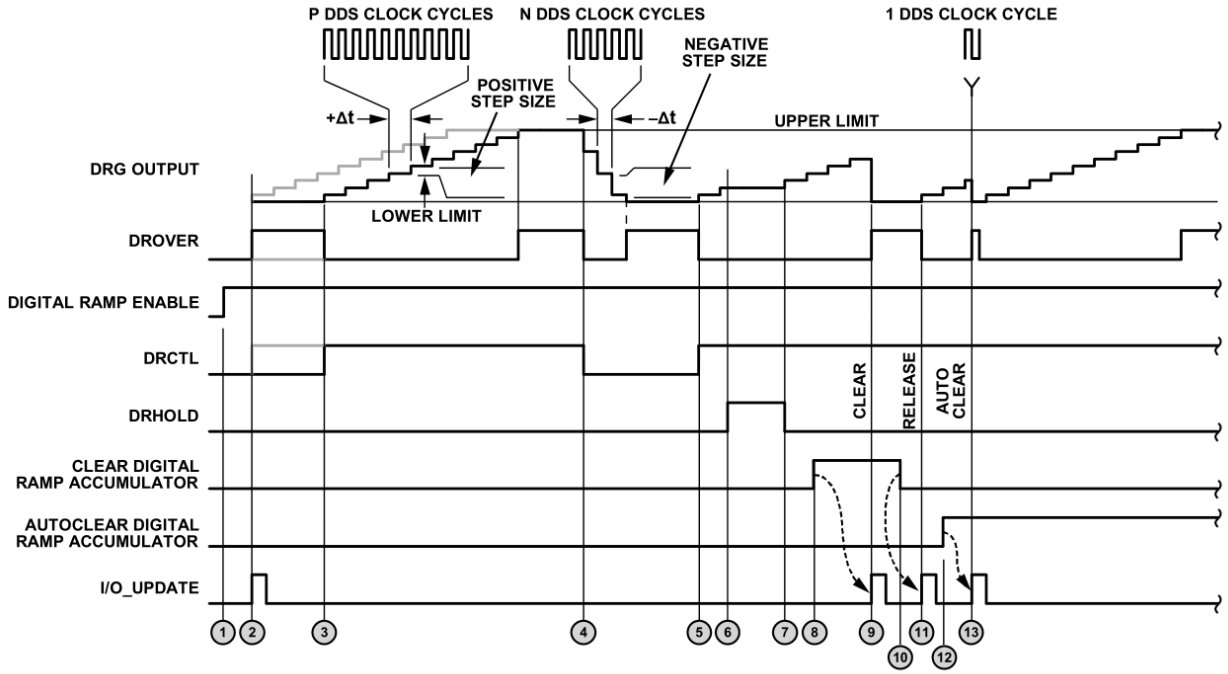

Figure 3.6: Excerpt from page 30 of the AD9910 datasheet [3], showing a sample sequence demonstrating DRG control. Frequency ramping is performed using the DRG, which is initiated with programming (see Appendix A) in step 1. At steps 2 or 3 the DRCTL digital pin is brought high, beginning the upward frequency ramp. The frequency reaches the maximum value and remains there until step 4, where the DRCTL pin is made low and the downward ramp begins. (Note that the values P, $+\Delta t$, N, and $-\Delta t$ may be freely chosen independent of each other.) The DRHOLD digital pin is brought high for the interval 6 to 7, during which time the frequency is held constant. The remaining portions of the sequence describe actions not used in our experiment, but full details for this image may be found with the original source if needed.

3.2.3 AD9910 Electronics

After settling on the AD9910 as our optimal DDS, I initially intended to purchase the AD9910 chip alone at a low price of $35 and to build an RF circuit board around it. I am not an RF electronics specialist, unfortunately, so I never got a single indication that any of my design worked. Shortly afterwards we decided to instead purchase the "plug-and-play" AD9910 PCBZ evaluation board for $500, which has been our working solution to this day. This option still requires some on-board soldering, however, for components which depend on the chosen system clock frequency and the reference clock sampled by the PLL multiplier. For the conditions detailed below, the calculated values for these surface-mount components (size 0603) should be as follows: C13 = 100 pF, C15 = 22 pF, and R37 = 2.7 kΩ.

The AD9910 PCBZ requires both 3.3 V and 1.8 V power supplies to function. It also has an onboard local oscillator to serve as the system clock, but we chose to use a much more stable 10 MHz external reference source and multiply that up to 1 GHz for our system clock. This reference source is obtained from Symmetricom 5071A, a cesium clock primary frequency standard. Because all of our DDSs use the same source clock as a reference they are guaranteed to be frequency-locked; however, we did not deem it necessary for our experiment to phase-lock the devices using multichip synchronization.

3.2.4 Connection to the Arduino DUE

Each DDS is programmed directly by an Arduino DUE microcontroller through its serial peripheral interface. This model of Arduino was chosen because it operates on 3.3 V digital logic—to match that of the AD9910—and has a relatively fast system clock of 84 MHz. The DUE is configured in both hardware and software to communicate with up to three DDS devices, although this could be expanded in the future if necessary. The code on the Arduino is designed to interpret user commands from Cicero (see Appendix A), perform any relevant mathematics or conversions, and pass the intended programming to the specified DDS. Finally, a segment of startup code ensures that reasonable parameters are loaded onto

each DDS when the devices are powered on, but these typically still need to be rewritten before nearly any experimental sequence.

3.2.5 Connection to Cicero

The Arduino DUE receives communication along a single serial data channel from the RS232 port on the Cicero PC. The amplitude and polarity of these devices do not match, however, so I built a small op-amp circuit to make the electronics compatible. To reprogram one of the DDSs, one should navigate to the RS232 tab in Cicero and perform the following steps.

1. Open an existing RS232 group or create a new one.

2. Type a single command into the available field. See Appendix A for options.

3. Update, or "output", the command.

When entering the command, there are two field options: *raw* and *parameter*. If raw has been selected then simply type the full command as dictated in Appendix A. Parameter will change the field entry to allow for variable inputs, which can be quite convenient, but it is as important as ever not to mess up the command syntax when using this (e.g. a space at the end of the first text field and a sole semicolon in the second). Cicero only has one-way communication with the Arduino, so there is no error notification if the command syntax has been broken.

There are subsequently two available methods for updating the DDS programming. The first should be immediately obvious as a large "Output Now" button integrated into Cicero's RS232 tab layout. The second option is to include the RS232 group in a sequence timestep so that the command will be sent to the Arduino each time the experimental sequence is run. Currently this second method is predominately used and all the DDS programming is done during the MOT loading steps.

3.3 Gravity Compensation

We have previously discussed how in a vertical optical lattice configuration the diffraction beams must be aligned precisely along the direction of gravity such that the atoms stay in the center of the beams as they fall. Additionally, the frequency difference between the two lattice beams must be chirped during each diffraction pulse to compensate for the Doppler shift as the atoms accelerate due to the linear gravitational potential. Fortunately this only requires a linear frequency ramp, which is easily handled by the DRG module of the AD9910.

In the next chapter I will cover more about optical lattices and the Bloch-band model, but for now I will state that the frequency ramp required to compensate for gravity is

$$\dot{\delta} = \frac{g}{v_{\text{rec}}} \frac{2\hbar k^2}{m} = 2gk \tag{3.1}$$

where g is the acceleration due to gravity, $v_{\text{rec}} = \hbar k/m$ is the recoil velocity, k is the wavenumber of the diffraction beams, and m is the mass of a ytterbium atom. In our 556 nm optical lattice this sweep rate is equal to $2\pi\times$35.3 kHz/ms. Note that for driving an AOM, the RF should be simply equal to the frequency, not the angular frequency, so exclude the 2π when programming the DDS.

3.4 Lattice Depth Calibration

The depth of our optical lattice was most often calibrated using Kapitza-Dirac diffraction[5], conducted by applying a few-microsecond square pulse. For such short pulses we may approximate the wavefunction $|\psi_0\rangle$ is diabatically subjected to a sinusoidal potential, after which the wavefunction is given by

$$|\psi\rangle = |\psi_0\rangle \, \mathrm{e}^{-\frac{\mathrm{i}}{\hbar}\int_{\text{pulse}} U(z,t')\,\mathrm{d}t'} = |\psi_0\rangle \, \mathrm{e}^{-\frac{\mathrm{i}}{2\Delta}\Omega_R^2\tau} \mathrm{e}^{\frac{\mathrm{i}}{2\Delta}\Omega_R^2\tau\cos(2kz)} \tag{3.2}$$

where τ is the duration of the pulse, Δ is the single-photon detuning, and Ω_R is the single-photon Rabi frequency (defined in the upcoming chapter). With a useful Bessel function

[5]This is the same type of pulse used as the beam splitter in a contrast interferometer; however, the calibration pulse is necessarily very short so as to be safely within the Raman-Nath regime, unlike the lengthier splitting pulses mentioned in Section 1.1.2.

identity, we can rewrite the wavefunction as

$$|\psi\rangle = |\psi_0\rangle \, \mathrm{e}^{-\frac{\mathrm{i}}{2\Delta}\Omega_R^2 \tau} \sum_{n=-\infty}^{\infty} \mathrm{i}^n J_n \left(\frac{\Omega_R^2}{2\Delta} \tau \right) \mathrm{e}^{\mathrm{i}2nkz} \tag{3.3}$$

in which J_n are Bessel functions of the first kind and each $\mathrm{e}^{\mathrm{i}2nkz}$ represents a distinct momentum state $|g, 2n\hbar k\rangle$. States with momentum $2N\hbar k$ will be populated according to

$$P_N = J_N^2(\theta) \, , \quad N = 0, \pm 1, \pm 2, ... \tag{3.4}$$

where $\theta = \frac{\Omega_R^2}{2\Delta}\tau$ is the pulse area, proportional to both pulse time and lattice depth.

The calibration process, therefore, includes a measurement of each substantially populated state through time-of-flight absorption imaging. These values are normalized and plotted against the recorded pulse areas (in units of *optical power* $\times$ *time*), then fit to $J_N^2(A\theta)$ as per Equation (3.4). The resultant fit parameter A provided easy determination of any subsequent lattice depths by turning them into a simple power measurement. Typical uncertainty in our lattice depth is around 2%.

A secondary method of depth calibration was sometimes performed by measuring Rabi oscillations on a Bragg resonance, a technique which I will come back to in Section 4.2.3 once the underlying concepts have been introduced in the beginning of the upcoming chapter.

Chapter 4

BLOCH-BAND APPROACH TO ATOM OPTICS

The implementation of atom optics, as discussed in the previous chapter, allows for the coherent manipulation of atoms using highly tunable optical standing waves. Widely applicable in experiments incorporating coherent atomic center-of-mass motion, we shall focus on the use of such diffraction elements in atom interferometers. There are several well-established techniques for performing interferometric operations like beam-splitting, reflection, and acceleration—the one we shall discuss at length in this chapter is the Bragg pulse, which can be applied in any of these situations. In addition there is (i) the Kapitza-Dirac pulse, used for beam splitting in a contrast interferometer, as well as (ii) Bloch oscillations, typically used to accelerate an atomic wave packet.

An intuitive understanding of atom optics can come from considering individual photons interacting with an atom. In an optical lattice, which is made up of counter-propagating laser beams, an atom in the ground state may undergo stimulated absorption from one beam and stimulated emission into the other resulting in an addition of $2\hbar k$ of momentum, where k is the lattice wavevector. Higher number of photons may participate to accelerate the atom, but for processes where the internal state of the atoms remains unchanged, the external change in momentum must be some integer multiple of $2\hbar k$.

It has been customary to derive the behavior of such systems by considering the light wave as a periodic potential that connects the initial state with the target state. Recently our lab has begun utilizing the energy band structure of the Bloch-band model to interpret physical observations. It goes without saying that a suitable model which accurately describes the relevant physics is desirable for optimizing an experiment; in the realm of atom interferometry this means obtaining efficient diffraction amplitudes and controlling lattice-induced

phase shifts.

4.1 Bragg Pulses

The primary method we use for coherent manipulation of the atoms' momentum is through the Bragg transition. As recently mentioned, it is perhaps the most versatile atom-optics element. Prior to discussing a view of Bragg pulses with the Bloch-band approach, I will first work out the expected behavior of atoms in a weak optical potential and obtain the commonly-used simplified formulae.

The periodic potential of an optical lattice comes from the oscillatory behavior of the electric field. For two counter-propagating plane waves,

$$\begin{aligned}\vec{E}(z,t) &= E_0 f(t)\cos(\omega t - kz)\hat{e} + E_0 f(t)\cos(\omega t + kz)\hat{e} \\ &= 2E_0 f(t)\cos(kz)\cos(\omega t)\hat{e}\end{aligned} \tag{4.1}$$

with temporal envelope $f(t)$, a standing wave of light is formed which will interact with the atoms according to $\mathcal{H}_{\text{int}}(t) = -\vec{\mu}\cdot\vec{E}(t)$ in the dipole approximation. The dipole matrix element $\vec{\mu} = \langle e|e\vec{r}|g\rangle$ describes the coupling strength between $|g\rangle$ and $|e\rangle$, the internal ground and excited states of the atom, respectively. We can expand our Hilbert space to include external momentum states such that a single photon from the lattice may operate on an atom in either ground or excited state according to

$$\mathrm{e}^{\pm \mathrm{i}k\hat{z}}\,|g(e), n\hbar k\rangle = |g(e), (n\pm 1)\hbar k\rangle \tag{4.2}$$

which yields the interaction Hamiltonian,

$$\mathcal{H}_{\text{int}}(t) = -\mathrm{i}\mathrm{e}^{-\mathrm{i}\omega t}\frac{\hbar\Omega_R}{2}\left(|e,0\rangle\langle g,-1| - |e,0\rangle\langle g,+1|\right) + \text{h.c.} \tag{4.3}$$

The terms shown in Eqn. (4.3) portray photon absorption events while the Hermitian conjugate contains the terms responsible for stimulated emission. Also introduced in this equation is the single-photon Rabi frequency,

$$\Omega_R = \frac{\mu E_0}{\hbar} \tag{4.4}$$

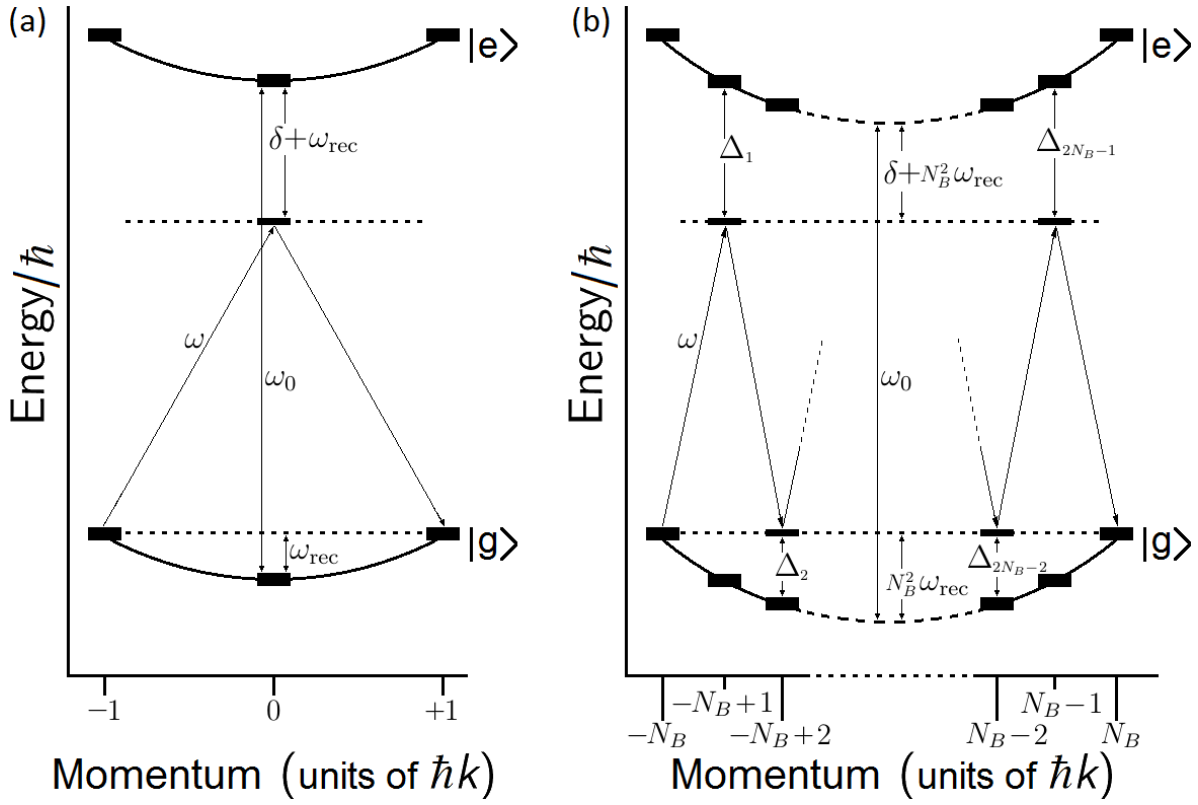

Figure 4.1: Energy diagram depicting (a) 1st-order and (b) N_B^{th}-order Bragg transitions in the frame of a stationary optical lattice. The energies fall onto a parabolic dispersion according to the free-space kinetic energy, $N_B^2\hbar^2k^2/2m = N_B^2\hbar\omega_{\text{rec}}$. The ground and excited states are separated by $\hbar\omega_0$, while the lattice photons have energy $\hbar\omega$.

which is the rate of oscillation between the two internal states connected by a single photon. With this the full Hamiltonian, $\mathcal{H}(t) = \mathcal{H}_0 + \mathcal{H}_{\text{int}}(t)$, where

$$\mathcal{H}_0 = \hbar\omega_0 \left|e,0\right\rangle \left\langle e,0\right| + \hbar\omega_{\text{rec}} \left(\left|g,-1\right\rangle \left\langle g,-1\right| + \left|g,+1\right\rangle \left\langle g,+1\right|\right) \tag{4.5}$$

includes the diagonal terms. As can be seen in Fig. 4.1(a), the excited state has energy of $\hbar\omega_0$ while the two ground states both have energy equal to the recoil frequency, $\hbar\omega_{\text{rec}} = \hbar^2k^2/2m$.

To understand the time dependence of the population amplitude for each external momentum state, insert the wavefunction

$$\left|\Psi(t)\right\rangle = c_{-1}(t)\mathrm{e}^{-\mathrm{i}\omega_{\text{rec}}t}\left|g,-1\right\rangle + c_0(t)\mathrm{e}^{-\mathrm{i}\omega_0 t}\left|e,0\right\rangle + c_{+1}(t)\mathrm{e}^{-\mathrm{i}\omega_{\text{rec}}t}\left|g,+1\right\rangle \tag{4.6}$$

into the Schrödinger equation. Some simple derivation and substitution will yield two coupled second-order differential equations:

$$\ddot{c}_{\pm 1}(t) - \mathrm{i}(\omega - \omega_0 + \omega_{\mathrm{rec}})\dot{c}_{\pm 1}(t) + \frac{\Omega_R^2}{4}\left(c_{\pm 1}(t) - c_{\mp 1}(t)\right) = 0\ . \tag{4.7}$$

For simplicity we will label $\Delta = \omega - \omega_0 + \omega_{\mathrm{rec}}$ as the single-photon detuning for this Rabi process. To avoid spontaneous scattering effects, it is important to make $\delta = \omega - \omega_0$ large (not to be confused with δ, the detuning between lattice beams); however, we will continue by also approximating $|\Delta| \gg \Omega_R$. This allows us to ignore the small effects of the additional ground states which may be considered negligible within this regime. We will later see how the limitations from this approximation of low lattice depth[1] are absent when using the Bloch-band approach and the superior reach of that approach will be discussed in the following sections of this chapter.

Now let us suppose that at $t = 0$ we have an initially pure ground state with a particular external momentum—without loss of generality this can be $|g, -1\rangle$, giving us boundary conditions $c_{-1}(0) = 1$ and $c_0(0) = c_{+1}(0) = 0$. Solving the differential equations produces

$$c_{-1}(t) = \mathrm{e}^{-\mathrm{i}\frac{\Omega_R^{(2)}}{2}t}\cos(\frac{\Omega_R^{(2)}}{2}t) \tag{4.8}$$

$$c_{+1}(t) = \mathrm{i}\mathrm{e}^{-\mathrm{i}\frac{\Omega_R^{(2)}}{2}t}\sin(\frac{\Omega_R^{(2)}}{2}t) \tag{4.9}$$

where we define the two-photon Rabi frequency, $\Omega_R^{(2)} = \frac{\Omega_R^2}{2\Delta} \approx \frac{\Omega_R^2}{2\delta}$, assuming large detuning in comparison with the recoil frequency, $|\delta| \gg \omega_{\mathrm{rec}}$. This result describes a two-photon interaction which causes the atoms to oscillate between states $|g, -1\rangle$ and $|g, +1\rangle$. If we call this a first-order Bragg transition, then it can be conceived that a $2N_B$-photon interaction would connect states $|g, -N_B\rangle$ and $|g, +N_B\rangle$, which we will call an N_B^{th}-order Bragg transition.

These higher order Bragg process would involve $2N_B - 1$ intermediate states, each with a different detuning, Δ_n, because all of the photons come from a single optical lattice. From

[1] In Equation (4.4) we see that the Rabi frequency, Ω_R, is proportional to the electric field strength. From the dipole force, the optical potential (Eqn. (2.4)) is proportional to intensity and thereby E_0^2 and Ω_R^2 as well. This equates a small Rabi frequency with a low lattice depth.

Figure 4.1(b)) one should be able to reduce the detuning to a simplified form,

$$\Delta_n = \begin{cases} \delta + (2N_B n - n^2)\omega_{\text{rec}} \,, & n \text{ odd} \\ (2N_B n - n^2)\omega_{\text{rec}} \,, & n \text{ even} \end{cases} \tag{4.10}$$

which may be inserted into an expression for the $2N_B$-photon Rabi frequency [22, 26], taken to be the product of two-photon constituent transitions through each of the intermediate states:

$$\Omega_R^{(2N_B)} = \Omega_R \prod_{n=1}^{2N_B-1} \frac{\Omega_R}{2\Delta_n} = \frac{[\Omega_R]^{2N_B}}{2^{4N_B-3}\left[(N_B-1)!\right]^2 \delta^{N_B}\omega_{\text{rec}}^{N_B-1}} \,. \tag{4.11}$$

Once the Rabi frequency for a particular Bragg process has been obtained, the temporal envelope from Equation (4.1), $f(t)$, may be chosen to achieve a desired population output following the pulse. Continuing the first-order Bragg example above, a square pulse of duration τ will produce population in $|g,+1\rangle$ according to $P_{+1}(\tau) = \sin^2\left(\frac{\Omega_R^{(2)}}{2}\tau\right)$. Therefore, when $\Omega_R^{(2)}\tau = \pi$ the atoms will experience maximal transfer from $|g,-1\rangle$ to $|g,+1\rangle$; this is how a mirror pulse works within an atom interferometer. Additionally, when $\Omega_R^{(2)}\tau = \pi/2$ the atoms will go into an equal superposition of $|g,-1\rangle$ and $|g,+1\rangle$; this is an example of a beamsplitting pulse.

Finally, this derivation so far has only shown that Bragg pulses can be applied to reverse the momentum of atoms traveling at $\pm N_B\hbar k$ in the lab frame. To use Bragg pulses for accelerating atoms to larger values of momentum, simply use this same process in a moving reference frame—this can be achieved rather easily by modifying the lattice beam frequencies to create a moving standing wave. In the frame of the optical lattice the counter-propagating laser beams must exist at the same frequency, but this can be shifted into the atoms' reference frame, $v = N_B\hbar k/m$. The Doppler effect results in a frequency shift of

$$\Delta\omega = \frac{\Delta v}{c}\omega = \Delta v k = \frac{N_B\hbar k^2}{m} \,, \tag{4.12}$$

although, since the lattice is comprised of two beams which undergo equal and opposite frequency shifts, the actual frequency difference (i.e. lattice detuning) should be

$$\delta_{N_B} = 4N_B\omega_{\text{rec}} \,. \tag{4.13}$$

Now we have changed the situation to imparting momentum to atoms at rest with a moving lattice; however, the linear relationship between atom velocity and lattice detuning should trivialize conversions for accelerating atoms in any frame.

4.2 Bloch-band Model

Atomic physics, ultracold atoms in particular, has borrowed much from the work done in solid state physics. The availability of a precisely controllable, albeit significantly smaller, experimental platform caters to tasks such as quantum simulation where crystal lattice structures and many-body systems may be recreated with individual atoms or single sites in optical lattices. Viewing such systems through the lens of the Bloch-band model grants an intuitive understanding of the behavior of atom optics used in these experiments [24].

The Bloch-band model, as discussed in Section 1.3, provides the solution to neutral atoms existing in the periodic potential formed by an optical lattice. The periodicity in physical space allows a reduction of the infinite domain of the complementary 'momentum' space to a finite range of 'quasimomentum'.[2] Figure 4.2 shows this reduction to the first Brillouin zone where the original parabolic energy dispersion wraps around the zone edges. This leads to a set of energy crossings which, in the presence of the periodic potential, experience level repulsion which is clear from second-order perturbation theory—these avoided crossings split the energy dispersion into distinct 'bands'.

4.2.1 Adiabaticity Criterion

The eigenstates of this system are no longer the free-particle momentum states, $|\vec{p}\rangle$, but rather states labeled by the quasimomentum and band number, $|\vec{q}, b\rangle$. As long as the optical lattice is turned on adiabatically, there should be a one-to-one mapping between states in these two bases. (An exception to this statement exists at the avoided crossings, which will be addressed shortly). For an optical potential, $U(z,t) = U_0(t)\sin^2(kz)$ with lattice depth

[2] This notion also appears in Floquet theory, where temporal periodicity leads to a natural usage of the finite 'quasienergy' domain.

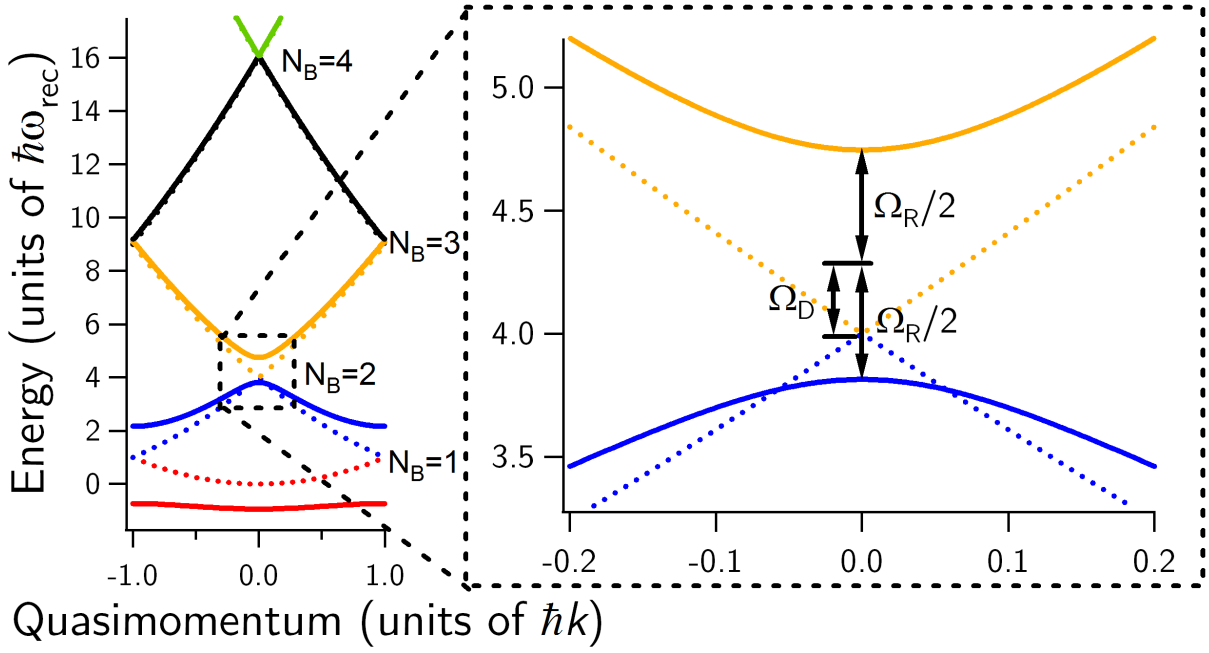

Figure 4.2: Calculated atomic energy bands in quasimomentum space for a sinusoidal optical potential with a lattice depth of $U_0 = 6\hbar\omega_{\text{rec}}$ (solid lines). The free-particle dispersion, $U_0 = 0$, is provided as a reference (dashed lines). The first- through fourth-order Bragg transitions are shown on the left, indicated by $N_B = 1$ to 4. On the right is an expanded view of $N_B = 2$, where Ω_R and Ω_D correspond to the frequencies of Rabi flopping and diffraction phase evolution (see text), respectively.

$U_0(t)$, the adiabaticity criterion can be written as

$$\frac{1}{U_0}\frac{\partial U_0}{\partial t} \ll \Delta E(q)/\hbar \tag{4.14}$$

where $\Delta E(q)$ is the energy difference between our state of interest and the nearest eigenstate in an adjacent band. Note that in higher bands the adiabaticity criterion becomes easier to satisfy since the band separation grows linearly due to the band structure being based on an originally quadratic dispersion.

The amplitude of a pulsed optical lattice must go to zero as $t \to \pm\infty$; therefore, the band gap at an avoided crossing also goes to zero and each of the corresponding states $|\pm N_B\hbar k\rangle_p$ will diabatically load into an equal superposition state of the two associated bands, $N_B - 1$

and N_B. This wavefunction,

$$|\Psi_{\pm}(t)\rangle = \tfrac{1}{\sqrt{2}}\left(|q, N_B - 1\rangle_{q,b} \mp \mathrm{e}^{-\mathrm{i}\Omega_R^{(2N_B)}t}\,|q, N_B\rangle_{q,b}\right)$$
$$\text{where} \quad q = \begin{cases} 0\,, & N_B \text{ even} \\ \pm 1\,, & N_B \text{ odd} \end{cases} \tag{4.15}$$

shows explicitly the Rabi oscillations observed in an N_B^{th}-order Bragg pulse. For example, when the pulse amplitude and duration satisfy $\int \Omega_R^{(2N_B)} t\,\mathrm{d}t = \pi$ the parity of the wavefunction will flip and the output state in the free-particle basis will be $|\mp N_B\hbar k\rangle_p$, effectively performing a Bragg π–pulse.

The adiabaticity criterion is not radically different for Bragg transitions, however—simply change $\Delta E(q)$ in Equation (4.14) to represent the energy separation from the eigenstate nearest to our *two* states of interest. For a Bragg pulse under typical experimental conditions using a smooth pulse profile (e.g. Gaussian) with width τ, the inequality from Eqn. (4.14) becomes

$$\tau \gg \frac{1}{4(N_B - 1)\omega_{\text{rec}}} \tag{4.16}$$

for $N_B > 1$. Due to the quadratic free-particle dispersion the limiting energy separation $\Delta E(q)$ comes from the band beneath the corresponding avoided crossing, but $N_B = 1$ has a unique feature in that there is no band below the avoided crossing. The adiabaticity criterion specific to first-order Bragg pulses is then $\tau \gg \frac{1}{8\omega_{\text{rec}}}$. Adhering to these adiabatic conditions will serve to minimize the population in undesired momentum states beyond the two coupled through the Bragg transition. As alluded to in Section 4.1, significant detuning from the single-photon transition (i.e. $|\Delta| \gg \Omega_R$) will also suppress population of the virtual intermediate states, reducing this to a two-state Rabi problem with an analytic formula for generalized Rabi frequencies; however, this limits the predictive power to the perturbative regime which will be discussed in the following section.

4.2.2 Measuring Rabi Frequencies

The Bloch-band model neatly describes Bragg transitions as occurring at the avoided crossings in quasimomentum space. As shown from Equation (4.15), the population of the $|\pm N_B\hbar k\rangle$ states in the free-particle basis oscillate sinusoidally and out of phase with each other at angular frequency Ω_R. In the Bloch-band picture, this oscillation frequency is equivalent to the band separation between the two bands that arise from the avoided crossing (see Fig. 4.2 inset). To establish the validity of this approach to atom optics we made Rabi frequency measurements and showed the predictive power of this model beyond the perturbative regime.

These experiments were conducted by applying horizontally oriented diffraction beams to a BEC, where the single-photon detuning was set at $\Delta = +3500\Gamma$ and the lattice frequency differential was chosen according to Equation (4.13). For each Rabi frequency measurement, the diffraction pulse intensity was constructed to have a Gaussian rise and fall with an intermediate flat region of variable extent (Fig. 4.3(a)). The Gaussian 1/e time for each iteration was $\tau_{1/e} = 27\,\mu$s to ensure adiabaticity. The populations of the two relevant momentum states were monitored with time-of-flight absorption imaging and the fractional population in the final state was fit to a sinusoid, $P(t) = \sin^2[\frac{1}{2}\int_{t_0}^{t}\Omega_R^{(2N_B)}(t')\,\mathrm{d}t']$, as demonstrated in Figure 4.3(b). The only free fit parameters were the amplitude, phase[3], and frequency of the signal.

The final part of Figure 4.3 shows that our data have excellent agreement with the Bloch-bands calculation, while the commonly-used analytic Rabi frequency formula in Equation (4.11) clearly breaks down at larger lattice depths. Operation of such pulses at large depths involves a stronger contribution from the virtual intermediate states; namely, the perturbation to these states is large enough that each unique Δ_n in the original derivation becomes inaccurate. Note that the model curves have no fit parameters.

---

[3]Any phase shift arising from nonzero diffracted fraction at zero pulse duration is due exclusively to the pulse rise and fall.

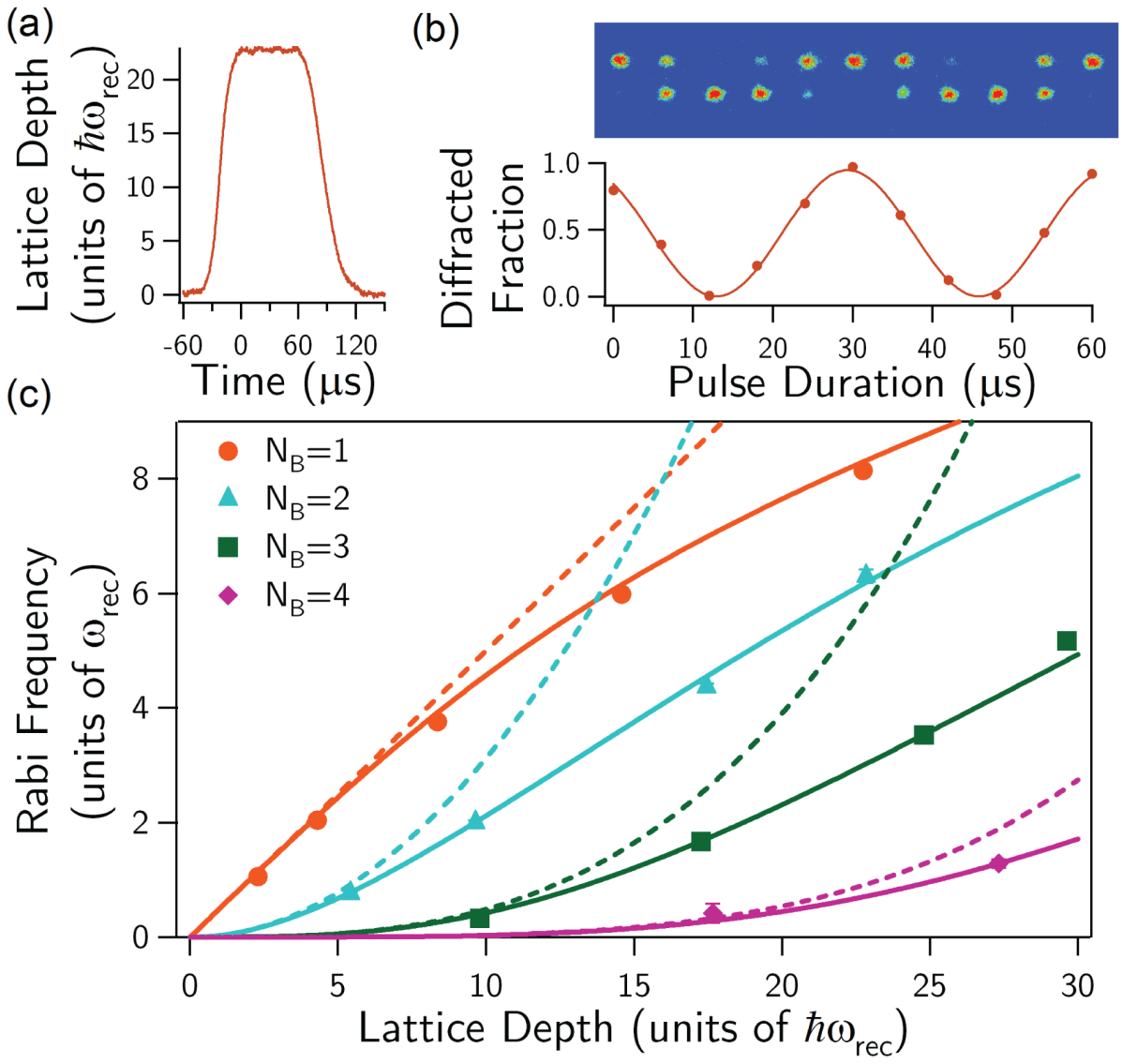

Figure 4.3: Measurement of Rabi frequencies and comparison with predictive models. (a) Sample pulse profile. (b) Rabi oscillations for $N_B = 1$ with a lattice depth of $U_0 = 22.7\hbar\omega_{\mathrm{rec}}$. Sample set of time-of-flight absorption imanges and sinusoidal fit to population data. Pulse duration is defined as the flat region of constant intensity, excluding the Gaussian rise and fall. (c) Measured Rabi frequencies for various lattice depths and for $N_B = 1, 2, 3, 4$. Comparison of the Bloch-band calculation and the commonly-used perturbative formula from Eqn. (4.11) are shown as the solid and dashed lines, respectively. The single-photon detuning of the diffraction beams for this data set was $\Delta = +3500\Gamma$.

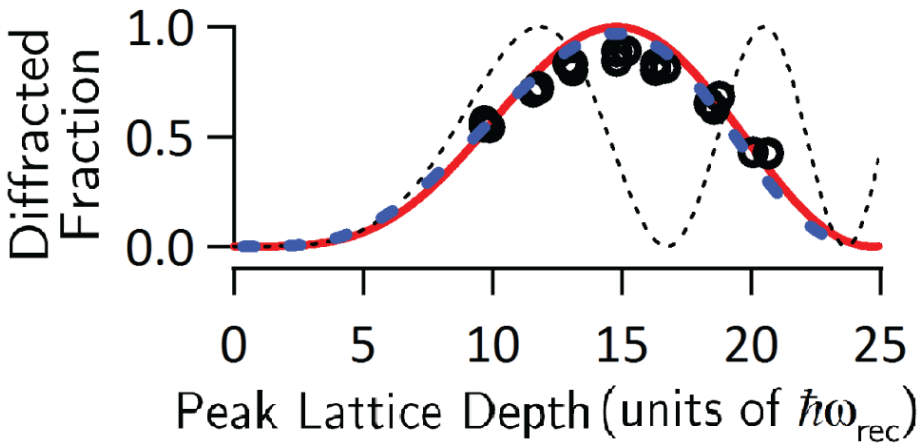

Figure 4.4: Population in the final state after a π–pulse at $N_B = 2$, using a Gaussian pulse profile with 1/e radius of 27μs. Measured data are represented by black circles, Bloch-band calculation is the red line, conventional Rabi formula (Eqn. (4.11)) is the thin black dotted line, and a full numerical integration in the free-space momentum basis is shown by the blue dashed line. As discussed in the text, the analytic Rabi formula breaks down at large lattice depths, despite the necessity to operate at those depths to perform a π–pulse under these conditions. The single-photon detuning of the diffraction beams for this data set was $\Delta = +3500\Gamma$.

4.2.3 Diffraction Amplitudes

The usefulness of accurate Rabi frequencies provided by the Bloch-band model is found primarily in its application to population amplitude in the two momentum states of interest. In many ultracold atom experiments it is desirable to execute efficient π–pulses or accurate $\frac{\pi}{2}$–pulses. While these conditions may simply be determined experimentally, the model for predicting the correct lattice depth to perform such a pulse should more often be the Bloch-band model due to its robustness at larger lattice depths. In interferometric sequences, the duration of necessary atom optics is typically minimized to increase the available interaction times for making sensitive phase measurements. Consequently the Bragg pulses require larger Rabi frequencies—and thereby larger lattice depths—to retain the appropriate π– or $\frac{\pi}{2}$–pulse condition.

One useful application that takes advantage of accurate diffraction amplitude measure-

ments is the calibration of optical lattice depth. This is an alternative method to Kaptiza-Dirac diffraction, mentioned at the end of the previous chapter, and may be used as a substitute or as a complementary calibration measurement. Such a procedure is identical to that used to obtain all of the data in Figure 4.3, but is paired with a power measurement of the optical lattice beams with the same amplitude as they had during the Rabi oscillation measurement. The solid theory curves in Fig. 4.3(c) would then relate a depth to the corresponding measured power and, as with the other technique, all subsequent power measurements could be converted to depth using this linear relationship.

4.3 Lattice-induced Phase Shifts

An additional benefit of the Bloch-band approach to atom optics is that it properly explains lattice-induced phase shifts—a particularly important systematic effect in precision interferometry that may be understood and suppressed using these methods. The fact that the band dispersion differs from the free-particle energy dispersion leads to an expectation that an atomic wavefunction will evolve phase differently while in an optical lattice; however, the customary derivation for understanding Bragg transitions (back in Section 4.1) is completely in the perturbative regime and fails to account at all for the existence of such phase shifts. This is an important consideration for atom interferometers, where the momentum-dependent phase shift on an atomic wave packet traveling in the lattice goes as

$$\Phi_D = \frac{1}{\hbar}\int_{\text{pulse}} \left(\bar{E}(q, U_0) - E_f(q)\right)\, \mathrm{d}t \tag{4.17}$$

and E_f is the free-particle energy and $U_0 = U_0(t)$. For a free particle loading adiabatically into a single band, $\bar{E}(t)$ is simply the energy of that band at the associated quasimomentum. For a Bragg pulse, the free-particle state loads into an equal superposition of band states (Eqn. (4.15)) and therefore $\bar{E}(t) = E_f + \hbar\Omega_D(t)$ is the average of the two band energies at the band gap (see Figure 4.2 inset). For this reason we will refer to Φ_D in the context of Bragg transitions as the 'diffraction phase' and in other contexts (e.g. Bloch oscillations) as the more general 'lattice-induced phase shift'.

4.3.1 Contrast Interferometer

All of the experiments pertaining to diffraction phase in this chapter were performed within a contrast interferometer, which was introduced back in Section 1.1.2. Our reported measured phases are typically the total interferometer phase, Φ, obtained from fitting $S(t) = C(t)\cos^2(4\omega_{\text{rec}}t + \Phi)$ to the interference signal where $t = 0$ occurs at the nominal point of overlap between the three paths. The total phase Φ will include contributions besides the particular Φ_D we are interested in, but these are kept sufficiently constant so as to be treated as an overall phase offset which may be ignored. Because Φ_D is momentum dependent, we must apply the Bloch-band model to each interferometer path independently to calculate an expected $\Phi = \frac{\phi_1+\phi_3}{2} - \phi_2$ for each experiment. All Bragg pulses in the interferometer had a Gaussian temporal profile with 1/e radius of 27 μs.

4.3.2 Diffraction Phase Measurement

To observe diffraction phase effects in an interferometer, the optical lattice depth was varied for a Bragg pulse chosen within the interferometer; however, coinciding with the lattice-induced phase shift is Rabi oscillation. This means as we make large changes to the Bragg pulse that (i) the π–pulse condition is no longer fulfilled, (ii) there is a smaller amplitude that gets reflected, and (iii) our interferometer signal deteriorates. In fact, the diffraction phase data in Fig. 4.5(b) and the diffraction amplitude data in Fig. 4.4 were obtained simultaneously from the same collection of experimental iterations. Later we will employ a technique[4] which measures diffraction phase without loss of atoms to extraneous momentum states; however, for now we continue with measurements using existent interferometer pulses.

For a given lattice depth the lattice-induced phase shift is greatest for atoms in the bottom band. This makes the reflection/mirror pulse the best candidate for initial observation of diffraction phase effects since the three paths have the lowest possible energies in the lattice frame during this pulse (path 2 is in the bottom band and paths 1 and 3 are at $N_B = 2$).

[4]See Section 4.4.

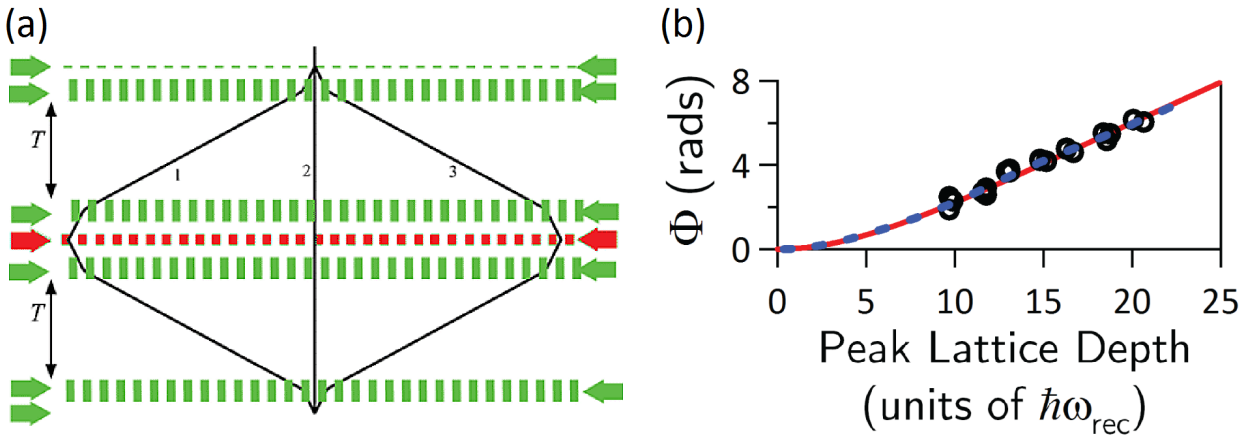

Figure 4.5: Demonstration of diffraction phases in a contrast interferometer through variation of the optical lattice depth for the mirror pulse. (a) Space-time diagram for a contrast interferometer. The pulse highlighted in red performed an $N_B = 2$ Bragg transition, connecting the $|\pm 2\hbar k\rangle$ momentum states. (b) Total contrast interferometer phase as a function of lattice depth for the highlighted pulse. Measured data are represented by black circles, the Bloch-band calculation is the red line, and a full numerical integration in the free-space momentum basis is shown by the blue dashed line. The single-photon detuning of the diffraction beams for this data set was $\Delta = +3500\Gamma$.

Figure 4.5 shows the results for such a measurement, which match well with the Bloch-band calculation.

4.3.3 Controlling Systematic Diffraction Phases

As was just demonstrated, diffraction phases are dependent on lattice depth and thereby laser intensity. This implies that interferometry experiments may then be susceptible to diffraction phase fluctuations as a result of intensity noise. To reduce diffraction phase noise it is not quite necessary to "remove" diffraction phase by finding a condition where $\Phi_D = 0$, but rather the objective should be to minimize $\delta\Phi_D = \delta U_0 \partial\phi/\partial U_0$. From the characterization of our laser intensity noise we found $\delta U_0 \propto U_0$ and therefore deemed $U_0\partial\phi/\partial U_0$ a suitable figure of merit as well.

We investigated the strength of diffraction phase shifts by measuring $U_0\partial\phi/\partial U_0$ for Bragg

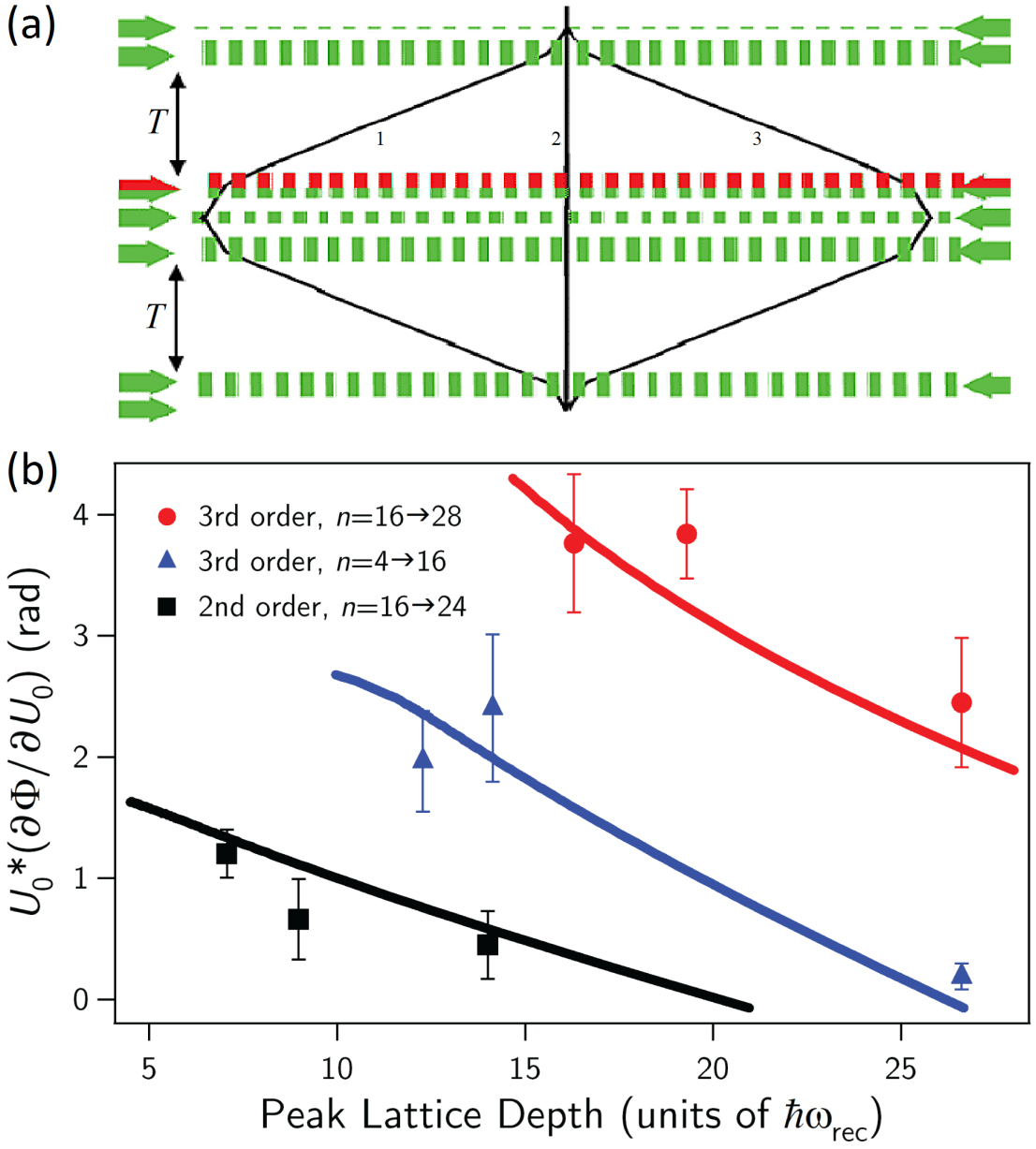

Figure 4.6: Suppression of diffraction phase fluctuations as a function of momentum and lattice depth. (a) Space-time diagram for a contrast interferometer. The deceleration step partially highlighted in red denotes a sequence of Bragg π–pulses bringing the high $|\pm 2N\hbar k\rangle$ momentum states to $|\pm 2\hbar k\rangle$. (b) Only one pulse in the deceleration sequence was used to manipulate diffraction phase effects (see text). This pulse either connected $|\pm 8\hbar k\rangle$ to $|\pm 2\hbar k\rangle$ (blue triangles), $|\pm 12\hbar k\rangle$ to $|\pm 8\hbar k\rangle$ (black squares), or $|\pm 14\hbar k\rangle$ to $|\pm 8\hbar k\rangle$ (red circles). The Bloch-band calculations are shown with solid lines. The single-photon detuning of the diffraction beams for this data set was $\Delta = +3500\Gamma$.

acceleration pulses at operating conditions within the contrast interferometer. These were second- and third-order Bragg pulses with the typical Gaussian temporal profile and intensities chosen around the π–pulse condition, i.e. 'π–point'. (In earlier work [54] we had found optimal momentum transfer with these settings, which was the basis for our choice here.) For each measurement we varied the lattice depth of a single pulse to find the π–pulse condition (similar to Fig. 4.4), then fit the corresponding Φ_D data (similar to Fig. 4.5) to determine the slope at the π–point. This slope multiplied by the lattice depth at that point gave us $U_0 \partial\phi/\partial U_0$ which has good agreement with the Bloch-band theory, as shown in Figure 4.6(b).

The contribution to this diffraction phase effect comes from all three paths of the interferometer, where the total phase $\Phi = \frac{\phi_1+\phi_3}{2} - \phi_2$. Recall that the individual path-dependent phase ϕ_i is momentum dependent and eventually becomes negligible as the band number increases. That is to say, at sufficiently high momentum separation the path which predominately contributes to the diffraction phase shift is that which undergoes the Bragg transition. The impact of other interferometer paths in nearby bands can be seen in the difference between the red and blue data points in Figure 4.6(b). The ϕ_i from the accelerating atoms should be the same there, but the atoms in the other two paths change relative momentum—and thereby band number—when considered in the frame of the moving optical lattice.

4.3.4 Diffraction Phase in Deep Lattices

We can also see in Fig. 4.6(b) that the value $U_0 \partial\phi/\partial U_0$ decreases with increasing lattice depth. This suggests an advantage to operate Bragg pulses with deeper lattices; however, the adiabaticity criterion puts a limit on the peak lattice depth in the form of a minimum pulse duration. In fact, the loss of adiabaticty leads to a reduced transfer efficiency in favor of population of undesired momentum states, which coincides with the regime where the Bloch-band theory is no longer able to accurately model either diffraction amplitude or diffraction phase. Because high transfer efficiency is typically desirable, it may be reasonable to state that the Bloch-band model is therefore sufficient to describe typical experimental operating

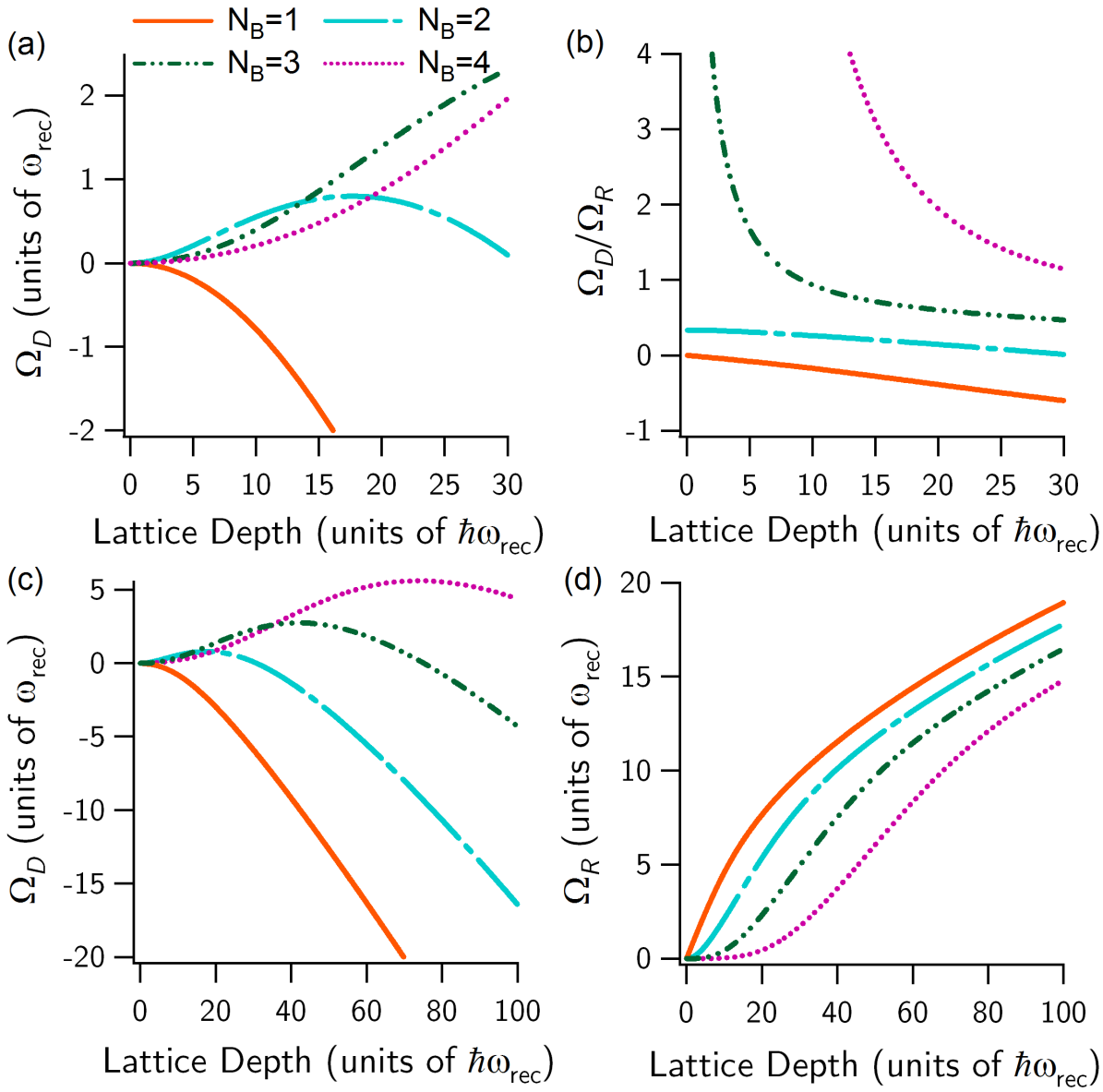

Figure 4.7: Bloch-band model in the limit of deep optical lattice potentials. (a) The frequency of diffraction phase evolution Ω_D as a function of lattice depth, shown for $N_B = 1$ to 4 Bragg transitions. (b) The ratio Ω_D/Ω_R as a function of lattice depth. The behavior of (c) Ω_D and (d) Ω_R at large lattice depths.

conditions.

Return to our definitions for Ω_R and Ω_D as, respectively, the splitting and average shift of bands at an avoided crossing for a Bragg transition. These can be derived from the Bloch-bands calculations and are shown in Figure 4.7. Consider for a simple square pulse that the quantity $\Omega_R\tau$ is fixed, but in general one can then see the diffraction phase goes as $\Phi_D \propto \frac{\Omega_D}{\Omega_R}$ (shown in Fig. 4.7(b)). Beyond a certain lattice depth these curves flatten out, reinforcing our earlier presumption that diffraction phase fluctuations are reduced at larger depths.

In Fig. 4.7(c) we see an interesting behavior of Ω_D with the presence of a single local maximum for each $N_B > 1$. This can be intuitively understood by considering the behavior of the bands as arising from 'level repulsion': as the perturbation increases (i.e. for deeper lattices) the strength of the repulsion grows. Due to the quadratic free-particle dispersion, each band will experience a net shift upwards in the weak-lattice regime since the band above is farther away than the band below. In the deep-lattice regime, on the other hand, the repulsion from an infinite number of higher bands eventually leads to a net shift downwards. The exception is the bottom band, which only ever experiences a negative shift. At depths beyond these maxima, the diffraction phase $\Phi_D \propto \frac{\Omega_D}{\Omega_R}$ regains sensitivity to depth fluctuations; however, the locations of these maxima are all in the diabatic regime for Bragg π–pulses and thus outside of typical experimental operating conditions.

Finally, the Bloch-band model predicts in the deep-lattice limit that the band gaps for all Bragg orders (i.e. Ω_R, shown in Fig. 4.7(d)) approach the harmonic oscillator spacing of $2\sqrt{U_0\omega_{\mathrm{rec}}/\hbar}$ as would be expected from a tight-binding model.

4.4 Measuring Band Structure

Depending on the application of certain interferometers, such as those which aim to measure recoil frequencies, diffraction phases will be treated as a problematic experimental systematic. But interferometers that are sensitive to diffraction phases can take advantage of this lattice-induced effect to interrogate the lattice itself, or even another arbitrary lattice (known or unknown). For example, consider atoms along a particular path loaded into a single band

eigenstate of the lattice dispersion (as opposed to the previously discussed Bragg transitions, which load into a superposition state). Then for a square pulse according to Equation (4.17) the band energy, $\bar{E}(q, U_0) = E_f(q) + \Phi_D\hbar/\tau$, may be determined as a function of quasimomentum, q, and pulse duration, τ. In such an implementation the momentum separation of the paths should be great enough that the unaddressed paths load into Bloch states with sufficiently high band number. This will make the lattice-induced phase shift negligible along these paths, resulting in an interferometer phase which primarily reflects the energy shift of the single band corresponding to the targeted path.

In our system the band structure was evaluated for the middle path in the bottom band (band 0), while the outer paths had been accelerated to $|\pm 8\hbar k\rangle$ thus loading into bands 7 and 8. We controlled the quasimomentum in the lattice frame by precisely manipulating the frequency difference, δ, of our diffraction beams in the lab frame. Following from Equation (4.13) we can generically write

$$q = \left(\frac{\delta}{4\omega_{\text{rec}}} - 2N\right)\hbar k \,, \qquad (4.18)$$
$$\text{where} \quad N \in \mathbb{Z} \quad \text{and} \quad -\hbar k < q \leq \hbar k$$

choosing N so that the quasimomentum remains within the first Brillouin zone. Figure 4.8(b) shows the shift to the interferometer phase as a function of lattice depth at $q = 0$. For this data the nondiffracting optical lattice was pulsed on with the usual Gaussian temporal shape, having $\tau_{1/e} = 27\,\mu$s and recording the depth at the pulse center. The Bloch-band theory curve, which only includes lattice-induced phase shift from the target path, has good agreement with the data.

Until this point all of our measurements of 'diffraction phase' shifts—recall these are specific to Bragg transitions—have necessarily occurred at an avoided crossing which diabatically places the atoms into a superposition of two band states. This most recent measurement of lattice-induced phase shift required that the atoms load into a single band, a task most easily accomplished in the bottom band at $q = 0$ where the adiabaticity criterion is most relaxed. The challenge in measuring the full structure of a band at various quasimomentum arises from the inclination of atoms to load into multi-band states at q near the avoided crossing.

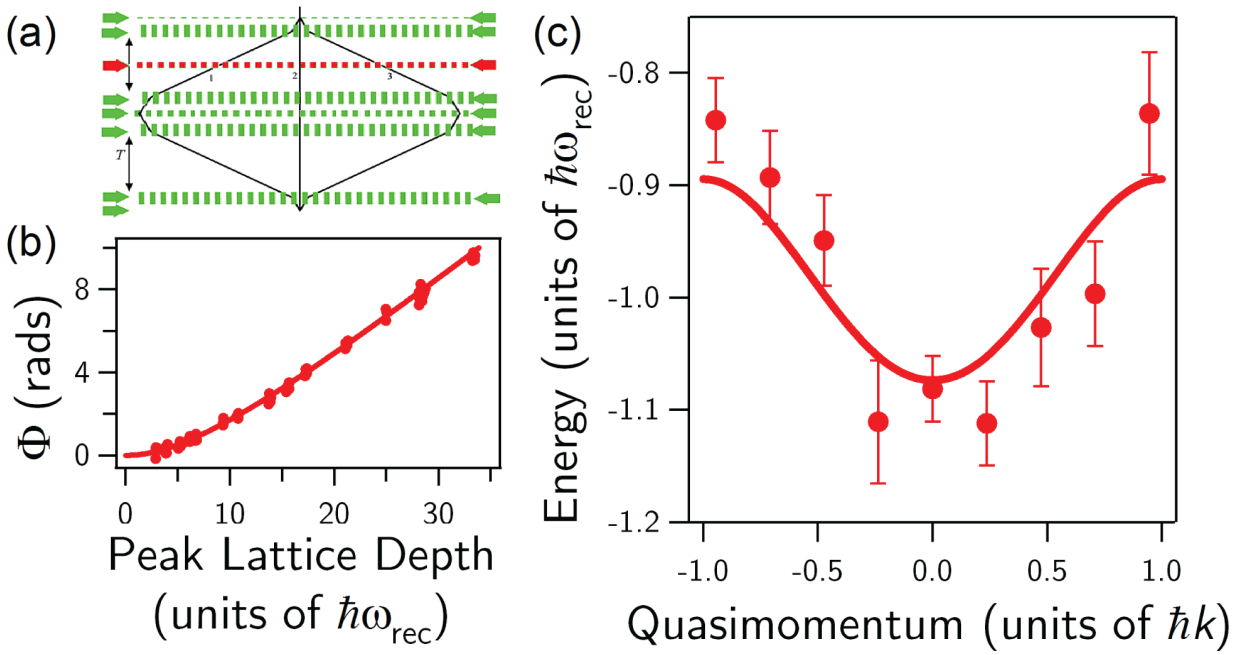

Figure 4.8: Determination of band structure from interferometric phase measurements. (a) Space-time diagram for a contrast interferometer. The pulse highlighted in red imparted the band structure to be determined and performed negligible population transfer in all interferometer paths. (b) Total contrast interferometer phase at $q = 0$ for various lattice strengths. (c) Measurements and theory for the ground band dispersion of an optical lattice with a depth of $6.5\hbar\omega_{\mathrm{rec}}$. The single-photon detuning of the diffraction beams for this data set was $\Delta = +3500\Gamma$.

Additionally, because the band energy $\bar{E}(q, U_0)$ is both a function of quasimomentum and depth, applying a set duration of fixed U_0 embedded within a specially tailored pulse would realize the most direct observation of the band structure. Therefore, the following sequence was conceived as a means for observing arbitrary q in a single band while keeping all other lattice-induced phase shifts either negligible or constant.

First we adiabatically turned on the nondiffracting lattice at $q = 0$, reaching a depth of $6.5\hbar\omega_{\mathrm{rec}}$ via a 150 μs cubic spline temporal shape. This lattice depth was kept constant during subsequent steps and had been measured at the 2% level using the calibration techniques mentioned in Section 3.4. Next we linearly ramped the frequency difference between the

diffraction beams, δ, arriving at $q = -0.95\hbar k$ after $56\,\mu$s. Then we swept the frequency detuning at the same rate in the opposite direction, stopping at the desired q for $100\,\mu$s, and continuing on to eventually reach $q = +0.95\hbar k$. Finally the frequency difference was brought back to zero (i.e. $q = 0$) and the lattice was turned off with the same cubic spline shape.

This method provided us a way to directly observe Φ_D as a function of quasimomentum. Using Equation (4.17) we converted Φ_D to an energy shift and added the calculated free-particle energy to obtain the band energy, $\bar{E}(q, U_0) = E_f(q) + \Phi_D\hbar/\tau$, which produced the ground band dispersion. In the sequence detailing our specially tailored pulse, all of the lattice-induced phase shifts accrued during each intensity ramp and frequency ramp were common between experimental iterations, resulting in a uniform phase offset. This became an energy offset to our ground band dispersion data which we determined by fitting with one free parameter (the constant offset) to the calculated energy dispersion for a lattice with a depth of $6.5\hbar\omega_{\mathrm{rec}}$. The resultant band dispersion is shown in Fig. 4.8(c) and exhibits good agreement with the Bloch-band theory.

Measurements of the lattice-induce phase shift provides an alternative method for determination of atomic band dispersion in an optical lattice, complementary to earlier methods [34, 21]. While we only demonstrated this technique for atoms in the ground band, a similar sequence may be applied to determine band structure in higher bands. Finally, this method is not limited to sinusoidal lattices and may be used to determine band structure in any arbitrary periodic potential, as well as to higher-dimensional and time-dependent (e.g. Floquet) lattices [19].

Chapter 5

BLOCH OSCILLATIONS AND MAGIC DEPTHS

Before interferometry even began on the BEC machine in our lab we had intentions of using Bloch oscillations (BOs) to accelerate the outer arms of the interferometer. The prospects of rapid and efficient momentum transfer led us to expect considerable gains in our recoil measurement sensitivity, which scales strongly with momentum separation. Our initial tests saw acceleration to momenta over $100\hbar k$ with a transfer efficiency of 99.9% per $\hbar k$ [53], but upon implementation of these acceleration pulses in the interferometer we discovered an immediate problem. The readout phase was no longer repeatable.

At the time we determinedly pressed forward, instead using Bragg pulses as our means for acceleration and demonstrating our first scale up of a symmetric three-path contrast interferometer to large momentum separation ($112\hbar k$) on this apparatus [54]. Our maximum attainable momentum separation was limited by the Bragg pulse efficiency[1], however, so we would eventually return to the idea of Bloch oscillations for large momentum interferometry. With our coincident investigations of atom optics using the Bloch-band picture, we were able to explain how the unacceptable phase instability of our original BO-based interferometer arose from intensity noise of the atom optics as well as demonstrate a novel BO technique for suppressing the lattice-induced phase noise.

5.1 Momentum Transfer with Bloch Oscillations

Bloch oscillations were initially predicted to be the result of particles accelerating in a lattice potential due to an external force. In quasimomentum space (in the lattice frame) this

[1] In our experiments optimal third-order Bragg pulses had an efficiency of 98.5% per $\hbar k$ [54]. For an interferometer with $112\hbar k$ separation this results in approximately 4% of atoms remaining along the outer paths that might contribute to the readout signal.

looks like movement left or right along the band. Upon reaching the Brillouin zone edge, a particle "reflects" to the opposite zone edge and continues its trajectory along the same direction in q-space. Therefore, the particle undergoes oscillations in both position- and momentum-space, with net zero displacement for an integer number of oscillation periods. If instead of applying an external force we consider that the lattice potential is accelerating (in the lab frame), then each subsequent Bloch oscillation will keep the particles within the same band in the lattice frame which corresponds to an acceleration in the laboratory frame. That is, the atoms end up with the same average acceleration as the standing optical lattice. This is especially pertinent in the context of ultracold atoms as a means for reaching large momentum.

Bloch oscillations are now a ubiquitous tool for imparting large momentum to neutral atoms [7, 41, 50, 20] with an accelerating lattice generated by sweeping the frequency difference between the lattice beams. One reason it is such a choice technique is that the efficiency and speed of momentum transfer can be made very high. The attainable efficiency for such processes can be understood by considering the various final states the atoms can take after passing through an avoided crossing, at the Brillouin zone edge or otherwise. We have already established that if the atoms remain in the original band, then they will have changed momentum in the lab frame. If the atoms tunnel across the band gap at the avoided crossing, then they will end up in an eigenstate of an adjacent band which corresponds to unchanged momentum in the free-space basis. This tunneling process is called Landau-Zener tunneling. As Bloch oscillations move into the diabatic regime Landau-Zener transitions become more prevalent. The Landau-Zener probability for a transition occurring between two bands [68, 14], b and $b+1$, is equal to

$$P_{\mathrm{LZ}} = \exp\left(-\pi \frac{\Omega_{\mathrm{BG}}^2}{4bka}\right) \tag{5.1}$$

where $\hbar\Omega_{\mathrm{BG}}$ is the band gap at the avoided crossing and $a = \dot{\delta}/2k$ is the acceleration of the atom in the lab frame. The lattice is formed by beams having approximately equal wavevectors, k, with a small relative frequency difference which varies in time as $\dot{\delta}$.

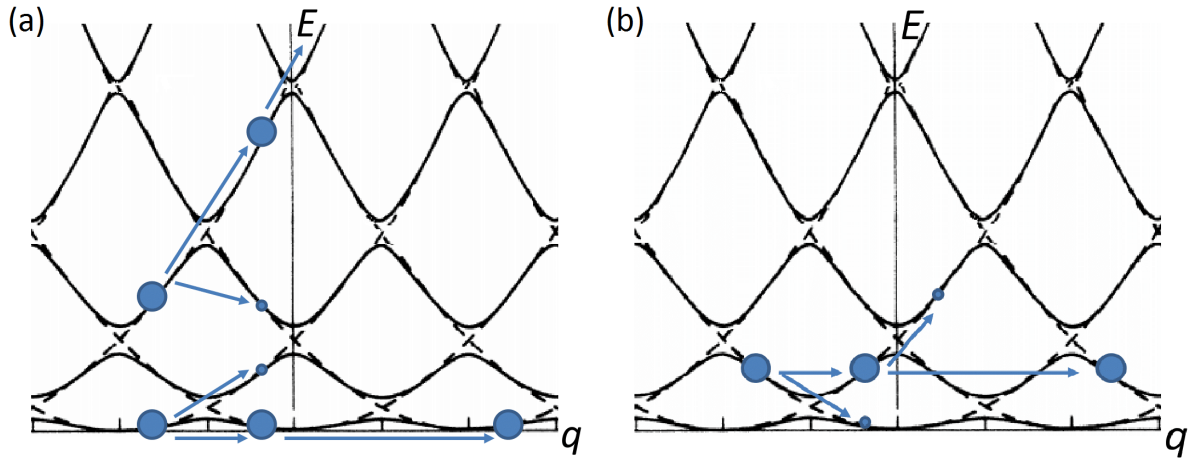

Figure 5.1: Bloch oscillations and Landau-Zener transitions in the Bloch-band picture, depicted over three Brillouin zones for clarity. (a) Atoms in the bottom band ($b = 0$) are swept adiabatically, performing Bloch oscillations with only small Landau-Zener losses. Atoms in an excited band—perhaps a separate path in an interferometer—dominantly experience Landau-Zener tunneling due to the smaller gaps between the higher bands. (b) Atoms may also undergo Bloch oscillations in an excited band, but with losses to both adjacent bands and more stringent adiabaticity criteria.

In the bottom band there is only a single band gap that atoms traverse; therefore, the probability of undergoing N Bloch oscillations would be $(1 - P_{\mathrm{LZ}})^N$.[2] For each of the excited Bloch bands, however, there are two avoided crossings within the first Brillouin zone, making the probability of each Bloch oscillation $(1 - P_{\mathrm{LZ1}})(1 - P_{\mathrm{LZ2}})$. According to Equation (5.1) these probabilities, i.e. efficiencies, may be improved by either increasing Ω_{BG} or decreasing $\dot{\delta}$. Because the band gaps diminish monotonically with band number, the intuitive best choice would be to operate in the bottom band where one can achieve the greatest efficiency and ramp speed.[3] This is also beneficial for interferometry, where we may want to simultaneously accelerate one path (by Bloch oscillations in a low band) while leaving the other path alone

[2]This assumes uncorrelated processes at each avoided crossing. We will find out in Chapter 7 that this expression needs to be corrected due to amplitude interference through the Landau-Zener-Stückelberg effect.

[3]Additional effects not considered here, such as spontaneous scattering and lattice-induced phase shifts, will lead to an optimal band choice. This will be addressed at the end of the chapter.

(which Landau-Zener tunnels to higher and higher bands). An example of this is shown in Figure 5.1(a). Operation of BOs in excited bands nonetheless remains an option which we will soon investigate more deeply in regard to the lattice-induced phase shifts.

5.1.1 Fixed Momentum Transfer

One may consider that the free-space momentum states coupled at excited-band avoided crossings will be $2N_B\hbar k$, exactly equal to the Bragg momentum transfer. Then one might suppose that Bloch oscillation in excited bands will cause atoms to be accelerated more quickly for a fixed lattice sweep rate due to larger momentum increments. Upon further consideration, however, it should be evident that the secondary avoided crossing encountered in each excited band removes $2(N_B - 1)\hbar k$, resulting in a net momentum change of $2\hbar k$ per BO regardless of band number. This effect is demonstrated in Figure 5.2 which compares the average momentum in bands 0 and 1 as the atoms undergo a sequence of three Bloch oscillations.

The fixed rate of $2\hbar k$ per BO was disappointingly low, so we sought for a method which would allow us to keep the $2N_B\hbar k$ momentum gain while skipping the $2(N_B - 1)\hbar k$ loss. Bragg pulses would meet this criteria but they lack the high efficiency observed in Bloch oscillations. In an attempt to merge the concepts of Bragg and BO we investigated the combination of adiabatic rapid passage and multiphoton Bragg diffraction [35]; however, the requirement to adiabatically turn on and off the lattice for each $2N_B\hbar k$ pulse meant that this option lacked the high speeds accessible with Bloch oscillations.

In interferometry, high efficiency and high speed are often desirable in order to reach large momentum separation quickly enough before decoherence of the interferometer signal. In particular, this allows for adequate "free evolution" interferometer evolution times for practical applications, e.g., sensing of external forces or evolving recoil phase. For this reason as well as its general applicability, we pursued the exploration of Bloch oscillations (rather than an alternative) in atom optics as a coherent beam splitter.

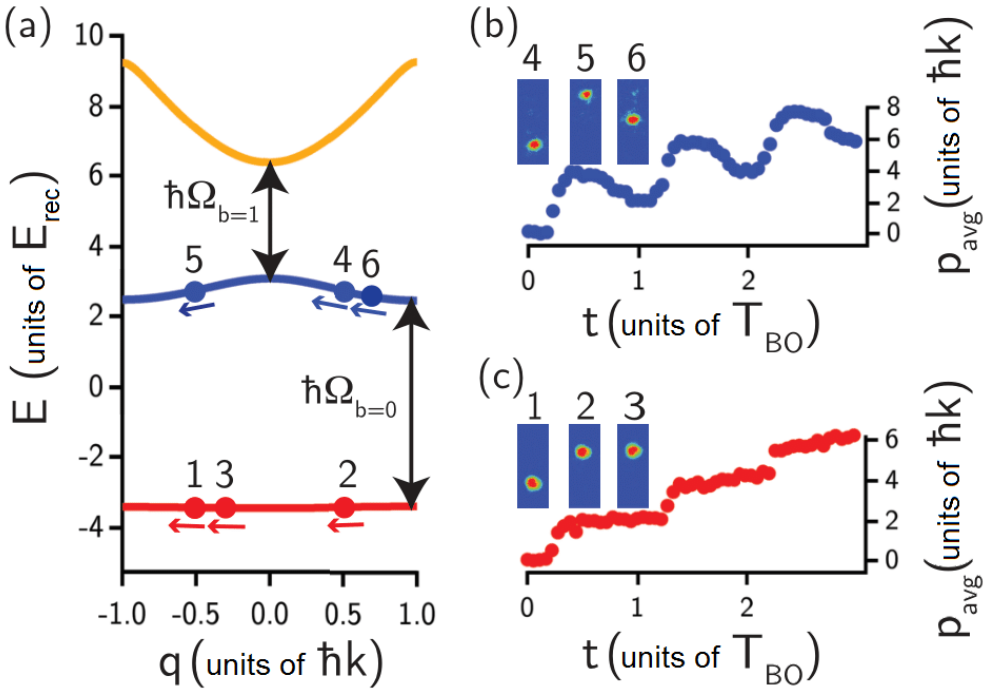

Figure 5.2: Behavior of average momentum for atoms performing Bloch oscillations in the ground- and first-excited band. (a) Bloch state trajectories for an atom during one BO in a lattice with a depth of $13.6\hbar\omega_{\mathrm{rec}}$. (Recall $E_{\mathrm{rec}} \equiv \hbar\omega_{\mathrm{rec}}$.) In the ground band ($b = 0$) the atom begins at position 1, then traverses the avoided crossing at the Brillouin zone edge where it gains $2\hbar k$ in the lab frame. It progresses past position 2 at at constant momentum until it completes the Bloch oscillation at 3. In the first excited band ($b = 1$) the atom begins at 4, then moves past the avoided crossing at $q = 0$ where it gains $4\hbar k$. From position 5 it progresses through the next avoided crossing where it loses $2\hbar k$ and emerges from the opposite Brillouin zone edge, completing the BO at position 6. (b) Average atom momentum after a non-integer number of Bloch oscillations in band 1, plotted as a function of sweep duration in units of the BO period, T_{BO}. The frequency sweep for BOs was $\dot{\delta} = 2\pi \times 83$ MHz/s and the intensity ramp for turning the lattice on and off was 300 μs. (c) Average atom momentum after traversal of band 0, with a frequency sweep of $2\pi \times 83$ MHz/s and an intensity ramp time of 600 μs. Insets in (b) and (c) show representative time-of-flight absorption images for the positions denoted in (a). The single-photon detuning of the diffraction beams for this data set was $\Delta = +3500\Gamma$.

5.1.2 Frequency Ramp Implementation

During a BO, the frequency ramp of a single lattice beam is controlled with its corresponding DDS (see Section 3.2) while the opposing lattice beam is kept at a constant frequency. To most easily satisfy the adiabatic shift from a free-space momentum state to a single Bloch-band state, the lattice beams are turned on with a fixed frequency difference chosen to place the atoms at a quasimomentum farthest from any avoided crossings on the relevant band. That is, for ground-band Bloch oscillations the atoms are 'loaded' into the lattice at $q = 0$, but for all excited-band BOs the atoms will begin and end at $q = \pm 0.5\hbar k$. At these positions on the Bloch-band dispersion an intensity ramp speed is selected such that the atoms primarily load into the target band, with minimal population in adjacent states. Following the same derivation used to obtain Eqn. (4.13), the frequency difference between lattice beams for loading stationary atoms into band b near $q = \pm 0.5\hbar k$ should be

$$\delta(t=0) = \begin{cases} \pm 4(b + |q|)\omega_{\text{rec}} \,, & b \text{ even} \\ \mp 4(b + (1 - |q|))\omega_{\text{rec}} \,, & b \text{ odd} \end{cases} \tag{5.2}$$

where $t = 0$ is taken to be the start of the frequency sweep $\dot{\delta}$. For $|q| = 0.5\hbar k$ this reduces to $\delta = \pm 4(b + 0.5)\omega_{\text{rec}}$. Note that this formula applies specifically in the frame of the atoms; in the laboratory frame an additional frequency shift of $\pm 4N\omega_{\text{rec}}$ should be included to address atoms already moving at $\pm N\hbar k$.

For demonstrations such as in Fig. 5.2, the choice in the sign of loading quasimomentum ($\pm 0.5\hbar k$) is insignificant. In an interferometer, however, we would like to place the unaccelerating atoms into as high a band as possible—this requires a careful selection of loading frequency difference. As an example, we will later see an interferometer with atoms in $|0\hbar k\rangle$ and $|6\hbar k\rangle$. In preparation to accelerate the $|6\hbar k\rangle$ atoms with $b = 1$ BOs, we may load into a lattice with relative detuning of either $4.5 \times 4\omega_{\text{rec}}$ or $7.5 \times 4\omega_{\text{rec}}$. These options place the $|0\hbar k\rangle$ atoms into $b = 4$ or $b = 8$, respectively; therefore, the latter choice is preferred since P_{LZ} will be higher (due to smaller Ω_{BG}) and the untargeted atoms will experience less disturbance.

Finally, the frequency ramp will be implemented using the DRG module (see Section 3.2.2)

with Δf and Δt programmed (see Appendix A) to have values that approximate a sufficiently smooth linear ramp in addition to achieving efficient Bloch oscillation. When increasing momentum separation between interferometer paths, the ramp direction naturally sends the unaccelerating atoms into higher and higher bands via Landau-Zener transitions. On the other hand, care should be taken when decreasing the momentum separation[4] that the untargeted atoms do not reach a band low enough to begin experiencing undesired Bloch oscillation. (e.g. This is why BOs can never be used as a mirror pulse to exchange momentum states of separate paths.)

5.2 Magic Depth

Without the proper motivation, excited-band BOs are perhaps just a novel, less efficient application of the Bloch oscillation technique. As was stated earlier, Bloch oscillations have often been attributed with ruining interferometer signals through uncontrollable phase noise. This effect is typically exhibited from BOs in the ground band, however, and the Bloch-band model suggests that operation of BOs in excited bands may—under special conditions—produce comparably less phase noise. In the following sections we will examine how a "magic depth" arises for all excited Bloch-bands and offers a regime for BOs where fluctuation of lattice-induced phase shifts (due to laser intensity noise) is suppressed.

5.2.1 Mach-Zehnder Interferometer

All of the experiments pertaining to BO lattice-induced phases in this chapter were performed within a simple Mach-Zehnder interferometer, which was introduced back in Section 1.1.1. Our reported measured phases are typically the total interferometer phase, Φ, obtained from fitting $S(\phi_R) = \frac{1}{2}(1 + V\cos(3\phi_R + \Phi))$ to the quantity $P_6/(P_0 + P_6)$ from the two output ports. Recall that ϕ_R is the lattice phase during the readout $\pi/2$–pulse.[5] All Bragg pulses

[4]This will at some point be necessary to close any interferometer which has used acceleration to increase the path separation.

[5]Briefly noted earlier, we do not have the AD9910 enabled to perform direct phase manipulation. The workaround we used was to shift the frequency for a variable time before the readout pulse. This allowed

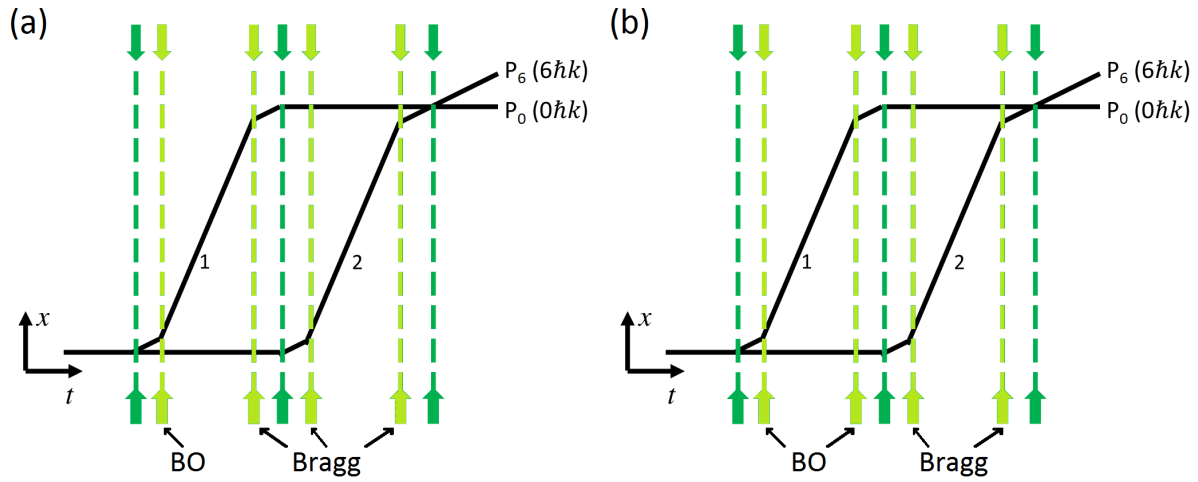

Figure 5.3: Asymmetric Mach-Zehnder interferometer geometry. (a) For most of the experiments in this chapter BOs were used only in the first acceleration sequence. (b) For our later demonstration of 20 BOs in band $b = 1$, the first Bragg deceleration sequence was replaced by Bloch oscillations.

in the interferometer had a Gaussian temporal profile with 1/e radius of 27 μs. Our typical BOs had a frequency sweep rate of $2\pi \times 83$ MHz/s, corresponding to $T_{\mathrm{BO}} = 360$ μs, but the specific value will be noted with each experiment.

The total interferometer phase $\Phi = \phi_1 - \phi_2$ should not include contributions that appear equally in each path. As a result, Mach-Zehnder interferometers are not naturally sensitive to lattice-induced phase shifts since the momentum-dependent Φ_D (from Eqn. (4.17)) is the same along paths 1 and 2 due to symmetry. Thus to observe such effects the symmetry of the interferometer must be broken, as shown in Figure 5.3. Unfortunately because the phase of our signal $S(\phi_R)$ is a function of the readout lattice phase, Mach-Zehnder interferometers are especially susceptible to mirror vibrations which add an unknown shift to ϕ_R. This undesired effect becomes worse for total interferometer times above a few milliseconds[6], hence, the following experiments were limited in the quantity of BOs that could be applied

us to adjust the lattice phase in a predictable manner without needing to overhaul our DDS electronics.

[6]Physical vibrations not suppressed by the optical table are typically on the order of a kilohertz or less.

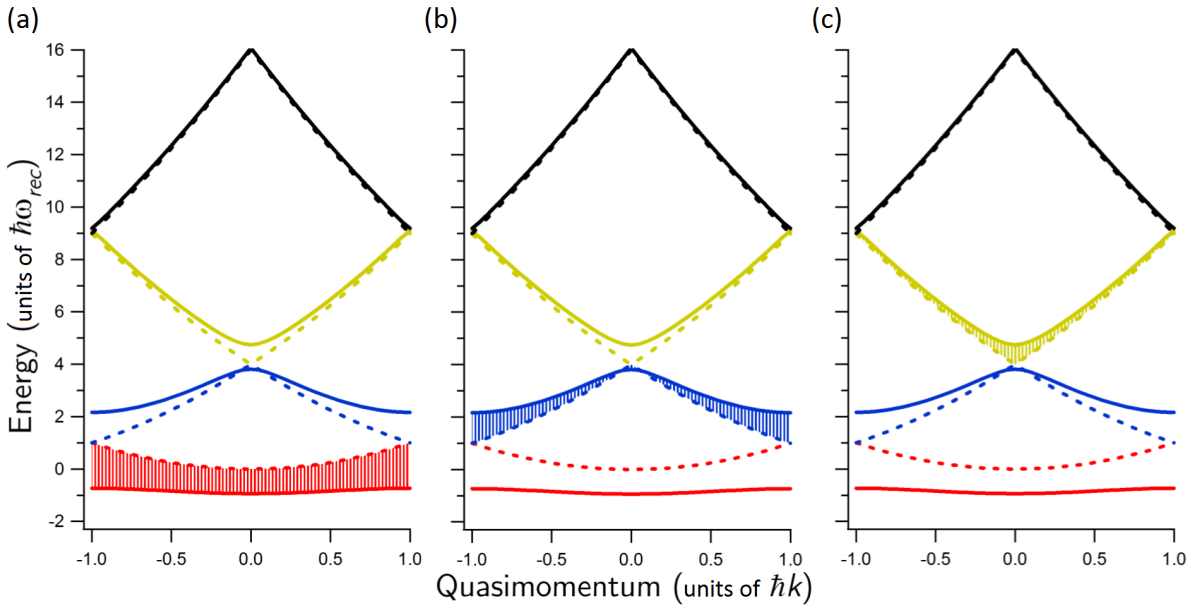

Figure 5.4: Examples of area in $E-q$ space, which relates to the lattice-induced phase shift accrued during Bloch oscillations. Depicted band structure is for a lattice depth of $6\hbar\omega_{\mathrm{rec}}$. The phase Φ_{BO} for a single BO is proportional to the highlighted area shown for a full traversal of (a) the ground band, (b) the first excited band, or (c) the second excited band.

in that time frame.

In order to apply Bloch oscillations to one path and not the other, the momentum separation realized from the splitting pulse needs to be great enough such that the unaccelerated atoms begin in a sufficiently high band. We found that $6\hbar k$ separation from a third-order Bragg pulse was enough to leave the untargeted path unaffected.

5.2.2 Phase Stability and Magic Depth

The general formula for a lattice-induced phase shift was given in Equation (4.17), and during Bloch oscillations $\bar{E}$ is just the eigenenergy of the band in which the BOs are performed. Additionally, when the lattice is accelerated using a linear frequency sweep, the phase shift for each Bloch oscillation becomes

$$\Phi_{BO} = \frac{1}{\hbar}\frac{\mathrm{d}t}{\mathrm{d}q}\int_{-\hbar k}^{+\hbar k}\left(\bar{E}(q,U_0) - E_f(q)\right)\,\mathrm{d}q \tag{5.3}$$

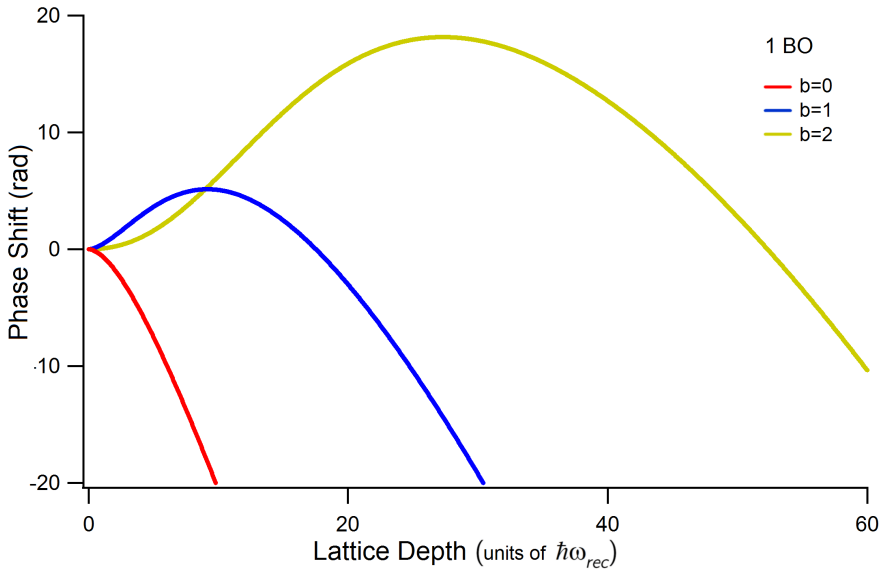

Figure 5.5: Prediction of magic depths for a single Bloch oscillation using Equation (5.3), assuming our typical frequency sweep of $2\pi \times 83$ MHz/s corresponding to $T_{\mathrm{BO}} = 360$ μs. Note that the function form and the x-axis are independent of BO parameters—only the y-axis changes scaling with frequency sweep rate. Additionally, these results are identical for all atoms and all wavelengths for diffraction when normalized to units of the recoil frequency.

which is proportional to the area between the Bloch-band and free-space dispersions in quasi-momentum space. This area (shaded regions in Figure 5.4) is a function of only the lattice depth and the quantity $\frac{\mathrm{d}q}{\mathrm{d}t} = \frac{m\dot{\delta}}{2k}$ is a constant set by experimental parameters. Alternatively we can write $\frac{\mathrm{d}q}{\mathrm{d}t} = \frac{2\hbar k}{T_{\mathrm{BO}}}$, which lets us express $\Phi_{BO} = \frac{1}{\hbar} T_{\mathrm{BO}} \langle \bar{E}(U_0) - E_f \rangle$ in terms of average energies.

Recall from the previous chapter how the level repulsion in these Bloch bands results in the following behaviors due to the quadratic free-space dispersion: (i) The ground band is pushed downward monotonically as the lattice depth increases. (ii) All excited bands are initially pushed up, then eventually stop, turn around, and move continuously downward with increasing lattice depth. Thus in a similar manner to Figure 4.7(c), the phase $\Phi_{BO}(U_0)$ in Figure 5.5 will exhibit exactly one maximum for every excited band but none for the ground band. Unlike for Bragg pulses, however, operation at these maxima may be conducted in

the adiabatic regime simply by reducing $\dot{\delta}$. This means that performing BOs in an excited band offers a suppression in lattice-induced phase noise to the second-order in intensity fluctuations, i.e. $\frac{1}{2}\left|\frac{\partial^2\langle\bar{E}\rangle}{\partial U_0^2}\right|_{U_{MD}} U_{MD}^2$, when operating at the magic depth U_{MD} which is defined at $\left|\frac{\partial\langle\bar{E}\rangle}{\partial U_0}\right|_{U_{MD}} = 0$. Note that because E_f has no depth dependence we need to evaluate these derivatives only for the average band energy.

5.2.3 Magic Depth Measurements

Our first demonstration of magic depth was in the lowest excited band $b = 1$ (see Fig. 5.6(a)) where a single BO was applied in a manner according to Figure 5.3(a). The visibility, as defined in Eqn. (1.3), was around 80% for each interference fringe contributing in this data set [40]. In comparison the ground band exhibited only about 10% visibility, a consequence attributed to the substantial sensitivity to depth fluctuations in this band. While there is no magic depth for $b = 0$, when operated at depths similar to the $b = 1$ magic depth ($\approx 10\hbar\omega_{\text{rec}}$) we can expect percent-level intensity noise to produce phase noise on the order of a radian per BO under the same conditions used in the figure.

At this point it is important to note that the model for producing the theory curves in Figure 5.5 only accounts for the phase accumulated by the atoms undergoing Bloch oscillations. Furthermore, the phase accounted for is only accrued during the BOs, neglecting to add the contribution from the intensity ramp when the lattice is turned on and off. Given these considerations, the total lattice-induced phase shift measured by our interferometer should be

$$\Phi_D = \phi_{1,I} + \phi_{1,f} - \phi_{2,I} - \phi_{2,f} \tag{5.4}$$

where $\phi_{i,I}$ is the phase accrued on path i during the intensity ramp and $\phi_{i,f}$ is the phase accrued on path i during the frequency sweep. This effect is exemplified in Figure 5.6(b), which clearly shows the impact of the intensity ramp on a magic depth calculation. More subtle is the significance of the second interferometer path, but its influence on the phase shift becomes greater with smaller momentum separation (e.g. zero BO in $b = 1$). In the

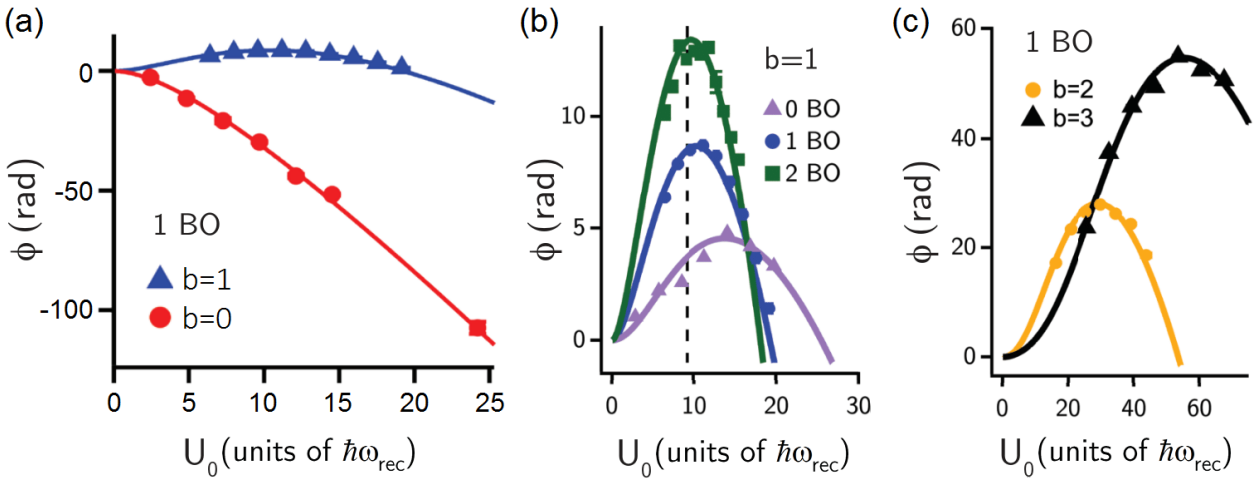

Figure 5.6: Magic depth measurements as a function of BO quantity and band number. (a) Interferometer phase shift as a function of lattice depth for one BO in the ground- or first-excited band, showing good agreement with full Bloch-band calculations using Eqn. (5.4). (b) Phase shifts for various quantities of BOs in the first-excited band, again showing good agreement with the model. The dashed-line denotes U_{MD}. (c) Demonstration of magic depths in the second- and third-excited band. For all data shown, the frequency sweep was $\dot{\delta} = 2\pi\times 83$ MHz/s and the intensity ramp time was 300 μs. The single-photon detuning of the diffraction beams for the data in (a) was $\Delta = +3500\Gamma$ and in (b) and (c) was $\Delta = +1300\Gamma$.

limit of infinite Bloch oscillations, the intensity ramp becomes negligible and the momentum separation is large; therefore, the magic depth approaches a value denoted by the dashed black line in the figure—a value equivalent to the magic depth predicted by the corresponding maximum in Figure 5.5. This we refer to as U_{MD}, in agreement with our definition above.

Our next magic depth measurements were performed with Bloch oscillations in higher excited bands. These data show good agreement with the model up to the third-excited band. We did not go to higher bands because we lacked the intensity in our diffraction beams to reach the expected magic depth for the fourth-excited band. In fact, our laser intensity was also not enough to reach the $b = 3$ magic depth, so we instead decreased the single-photon detuning in order to produce the last panel[7] of Figure 5.6. To actively pursue

[7]Technically, though it does not fit the order of this narrative, the data in Fig. 5.6(c) were taken before the data in Fig. 5.6(b). Consequently the lattice remained at a lower detuning for the middle panel as well.

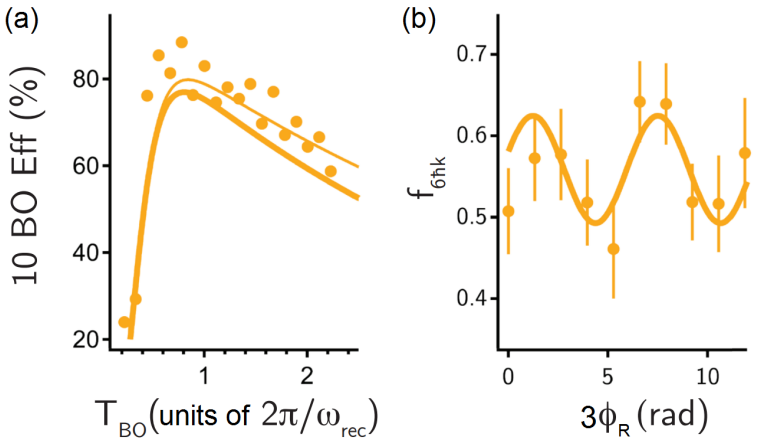

Figure 5.7: Using $b = 2$ BOs to achieve $20\hbar k$ momentum separation in an interferometer. (a) Total transfer efficiency of 10 BOs preformed in $b = 2$ with a lattice depth of $27.5\hbar\omega_{\mathrm{rec}}$, which fits well with simple theoretical models (see Section 5.2.4). (b) Interferometer signal for a sequence of 20 total BOs in $b = 2$ at $27.5\hbar\omega_{\mathrm{rec}}$, allocating 10 for acceleration and 10 for deceleration in accord with Figure 5.3(b). The frequency sweep in the interferometer was $\dot{\delta} = 2\pi \times 248$ MHz/s, corresponding to $T_{\mathrm{BO}} = 120$ μs. For all data shown, the intensity ramp time was 300 μs and the single-photon detuning of the diffraction beams was $\Delta = +3500\Gamma$.

magic depths in bands $b \geq 4$ within our apparatus, we would need to decrease the size of our diffraction beams; however, this solution comes with a variety of problems. Additionally, even lower detuning would lead to unacceptable levels of spontaneous scattering. Each of these effects will be addressed in the following section.

Finally, we tested the limits of our system which allowed implementation of up to 20 Bloch oscillations in the second-excited band while maintaining a deterministic interferometer phase. The visibility of this signal was 13% based on the sinusoidal fit (see Figure 5.7(b)). This equates to about 0.57 radians of phase noise as returned by the fit error in the phase; however, this is significantly higher than our expected 40 mrad bound on phase uncertainty due to intensity fluctuations [40]. Since the total time for this particular interferometer was 6.7 ms, we attribute the remaining majority of our observed phase noise to mirror vibrations.

5.2.4 Limitations to Operating in Higher Bands

Although the predicted phase noise per BO mildly increases with band number[8], the biggest reason to use a higher band in interferometers is the decrease in optimal T_{BO}. While the Bloch oscillation period is a freely tunable parameter, we define the optimal value to be that which yields the most efficient momentum transfer. For the demonstration of 20 BOs within an interferometer we show the optimization of T_{BO} in Figure 5.7(a). We measured the efficiency by counting the fraction of atoms in each momentum state after time-of-flight absorption imaging. A simple intuitive model including only Landau-Zener losses and spontaneous scattering (thick line in the figure) agreed with the data rather well. The efficiency of performing N Bloch oscillations

$$\varepsilon_N = (1 - P_{\mathrm{int}})^2 \times [(1 - P_{\mathrm{LZ}}) \times \exp(-R_s T_{\mathrm{BO}})]^N \tag{5.5}$$

contains a single maximum, indicating a clear optimal T_{BO}. Here P_{int} is the probability of spontaneous scattering during the intensity ramps, P_{LZ} is defined from Equation (5.1), and $\exp(-R_s T_{\mathrm{BO}})$ is spontaneous scattering losses during one BO. Because the lattice beam intensities are relatively low ($\frac{I}{I_{\mathrm{sat}}} \ll \frac{4\Delta^2}{\Gamma^2}$) the spontaneous scattering rate is $R_s \simeq \frac{U_0}{8\hbar}\frac{\Gamma}{\Delta}$, which may be adjusted by altering the lattice depth or the single-photon detuning.

While this parameter-free model does indeed capture the data quite well, it slightly underestimates the observed peak efficiency of 99.4% per $\hbar k$. This can be partly accounted for by noting that a blue-detuned lattice such as ours will cause the atomic wavefunction to have a greater amplitude at the lattice antinodes. This will decrease the effective laser intensity for our determination of the scattering rate, thereby decreasing the calculated R_s as well. The correction to spontaneous scattering produces improved agreement with the data (thin line in the figure) and a detailed comparison of the two models may be found in [39].

In preparation for obtaining large momentum separation in a BO-based interferometer,

[8]For an analysis of parameters scaling with band number, see [40]. For an even more detailed discussion, see [39].

we analyzed how the phase noise would scale with band number. Most of this work was done by Katie, who provides simulated data and explanation for the observed trends (again in [39]). Regardless of experimental parameters, the magic depth and the relevant band gaps at the magic depth increase monotonically with band number. Despite the flatness being greater for higher bands at U_{MD}, the quantity $\frac{1}{2}\left|\frac{\partial^2\langle\bar{E}\rangle}{\partial U_0^2}\right|_{U_{MD}} U_{MD}^2$ actually increases monotonically as well. The Bloch oscillation decreases with band number, likely due to the increasing band gaps; however, because the efficiency is dependent on single-photon detuning the exact values of T_{BO} are also affected. For a given detuning the efficiency exhibits a shallow maximum while the phase noise has a mild growth with band number (mentioned above). These final two parameters should be the most relevant when choosing a band for conducting BOs, but the weakness of their dependence on band number allows us to instead decide based on the BO period (which clearly suggests higher bands are better for interferometry). Typically diffraction beams are limited to a finite achievable intensity, so to reach U_{MD} for arbitrarily high bands (and short T_{BO}) one must reduce the laser detuning. Unfortunately, in this case the peak efficiency will drop due to increased spontaneous scattering. Needless to say, true optimization of these parameters can only be realized with consideration of the experimental constraints.

Chapter 6

VERTICAL INTERFEROMETRY WITH A NON-MAGNETIC ATOM

We have already established that our interferometer sensitivity grows with increasing momentum separation between the different paths. For some fixed optimal rate of acceleration, the greatest attainable momentum separation may only be increased with a longer total interferometer time. In addition, the contrast interferometer has improved sensitivity with more propagation time, T, which further appeals for a longer interferometer. This was the stimulus for performing Bloch oscillations for large momentum separation in a vertical interferometer—in comparison with a horizontal lattice, vertically oriented lattices allow for longer interaction times within the diffraction beams because atoms falling due to gravity remain within the center of the beams aligned to gravity.

For these reasons we chose to convert to a vertical geometry, as described in Section 3.1.2. All of the experiments following in this chapter were performed in the vertical configuration.

6.1 Vertical Launch

One benefit of the vertical lattice is the option of a vertical launch, which initiates an "atomic fountain" that may be used to essentially double the time available to perform our interferometer sequence and and allows greater flexibility for positioning of atom optical elements. Following our course of discovery in the previous chapter, our plan to maintain phase stability in a BO-based interferometer relies on using excited-band Bloch oscillations; however, since the launch occurs prior to the first beam-splitting pulse, ground-band Bloch oscillations should be sufficient for it. The relatively high phase noise only affects the immeasurable global phase and the higher efficiencies observed in this band make this the obvious choice.

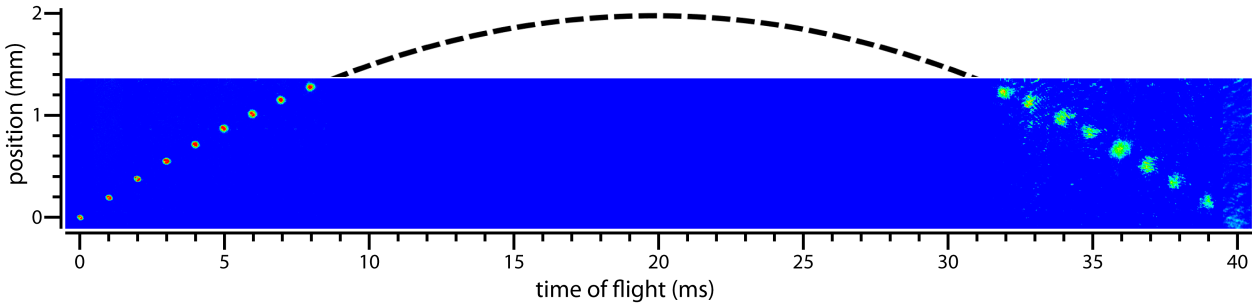

Figure 6.1: Demonstration of a vertical launch, or "atomic fountain", with ground-band Bloch oscillations. The lab-frame momentum of the atoms immediately after the launch was approximately 200 mm/s.

Thus all of the BO launches described in this chapter were performed in the ground band.

While one might attempt to conceive of a means to further double the total interferometer time with a second launch (or triple with a third, etc.), there are several reasons we have avoided this option. In our vertical interferometer design, any Bloch oscillations applied after the initial splitting pulse will see the separate momentum states in different Bloch bands. This may be acceptable when using BOs to accelerate only one path, since the remaining paths are in very high bands where the phase shifts are quite small (exactly the idea of magic depths discussed in the previous chapter). A BO launch on the other hand requires that all paths are in sufficiently low bands to undergo acceleration, where phase noise becomes a problem. This would lead to substantial lattice-induced phase shifts for each path, changing the output phase of the interferometer in an undesirable way.

Even in a horizontal diffraction geometry a vertical launch may be applied prior to the first splitting pulse, but any subsequent relaunches are problematic. Because our interferometer paths are each in different momentum states they are continuously changing their relative locations in position space. While it is possible to begin a BO launch at some time where the paths are spatially overlapped, any significant launch will have a long duration compared with the time it takes for the paths to separate. In the best case, the atoms move through different parts of the diffraction beams and acquire different phases. In the worst case, one

or more paths leave the lattice beams entirely before completion of the launch.

Despite our decision to forgo relaunches within the interferometer sequence, we found that multiple BO launches are incredibly useful for observing long time-of-flight without needing to drastically move the imaging optics. This helped in particular with the characterization of our delta-kick cooling pulse.

6.2 Delta-Kick Cooling

Although I have not quite yet come to the results of our conjugate Mach-Zehnder interferometer, it was during those experiments that we determined the anti-gravity beam (AGB) to be only an adequate cooling method. As mentioned in the corresponding Section 2.5, the reduction of kinetic temperature along the direction of gravity was incredibly challenging for a ^{174}Yb BEC due to the lack of magnetic moment. This was still a necessity for improved Bragg transfer efficiencies and stronger interference signals, so at this point we turned to delta-kick cooling. In fact, we had attempted delta-kick cooling (DKC) much earlier but never got good results until we eventually combined the technique with a BO launch.

The method of delta-kick cooling, or "matter wave lensing" [11, 36], has a very strong analogy to the propagation of a Gaussian laser beam through a physical lens. Upon release from the optical trap our BEC is expanding in time, like a diverging beam of light expands over a distance. By applying a spatially curved optical potential at an appropriate time the expanding matter wave becomes collimated, like a lens collimating light when placed at the correct distance from a point source. The optical potential for such matter wave lensing is typically obtained from the roughly-parabolic region of a simple Gaussian beam. The strength of the lens, applied at time t_0 after release from the ODT, depends on the curvature of the beam as well as the duration, δt, of the pulse. Specifically, collimation is achieved when

$$\delta t \sim \frac{1}{\omega^2 t_0} \tag{6.1}$$

where the trap frequency $\omega = \sqrt{\frac{4U_0}{m{w_0}^2}}$ for atoms of mass m, in a beam with peak depth

U_0 and waist w_0. To maintain a thin lens approximation it is also important that $\delta t \ll t_0$. Some additional considerations towards experimental parameters include (i) $U_0 \propto P_0$ and is limited by the laser power available and (ii) w_0 must be much larger than the size of the BEC at the time t_0 to avoid "aperturing". Finally, I should note that there is—as always—a general desire to increase the magnitude of the single-photon detuning such that spontaneous scattering is minimized; however, it is imperative that the sign of the detuning be negative[1]. (i.e. $\Delta < 0$ forms an attractive potential and behaves like a converging lens, while $\Delta > 0$ acts like a diverging lens.)

With these constraints in mind we settled on the following parameters for our delta-kick beam: the detuning $\Delta = -4600\Gamma$, the waist $w_0 = 150$ μm, and the time $t_0 = 25$ ms. The remaining parameters of pulse amplitude and duration were left unspecified to be optimized *in situ*, but we expected their values to fall within the desirable regimes detailed above.

6.2.1 DKC Beam Alignment

To improve vertical diffraction we needed to perform cooling in the vertical dimension. This meant that the DKC beam had to be oriented along a horizontal axis. Alignment of this beam began by continuously loading the MOT and observing the loss of atoms by intersection of the DKC beam with the MOT. We soon realized, however, that the center of the loading MOT differs from the location of the CMOT, and thereby the position of the crossed ODT. Unfortunately the CMOT cannot be observed in a continuous free-running mode, so the next best thing was to run the loading MOT and slowly step up just the magnetic field gradient until reaching the level attained during the usual CMOT. This was a much better approximation for the final ODT position and provided a good starting point for aligning the DKC beam to the BEC.

Because the delta-kick beam is aligned horizontally and the atoms are falling vertically, it would be a problem if the atoms fell through the beam much faster than δt. Thus we

[1]Incidentally, our optics had been biased towards positive detuning at this point, so we had to flip all of the AOMs to more easily reach large values of negative detuning.

decided to apply a Bloch oscillation launch and align the DKC beam to the apex of the atoms' parabolic trajectory, where their spatial variance would be minimal. Initially the launch was to occur shortly after release of the BEC, placing the apex about 2 mm above the position of the ODT. This was actually exceptionally difficult to align, so we adjusted the BO launch to be centered around $t_0/2$ and impart enough vertical acceleration such that the apex occurs at time t_0 and at the location of the ODT. Incidentally, this means that t_0 cannot be arbitrarily chosen, since the apex occurs when

$$-gt_0 + N_{\mathrm{BO}} \times 2v_{\mathrm{rec}} = 0 \tag{6.2}$$

for an integer number N_{BO} Bloch oscillations. To closely match our earlier chosen value, we elected to perform a launch of 30 Bloch oscillations yielding $t_0 = 25.37$ ms.

Alignment of the DKC beam resumed with resonant blasting of the atoms in the crossed ODT—now a much simpler arrangement than before. This was followed by the more sensitive alignment process of maximizing Kapitza-Dirac diffraction, which required the addition of a retro-reflecting mirror to form a lattice[2]. The final bit of beam alignment was performed by proper application of the delta-kick on the atom cloud at time t_0, then aiming to minimize the asymmetry of the kicked atoms. (This is analogous to the angular deflection of a laser which is displaced from the center of a lens.) This effect is particularly strong in our setup because we were only able to weakly satisfy $w_0 \gg \Delta x_{\mathrm{BEC}}$ due to limitations on our available power.

6.2.2 Temperature Measurement

Now with the beam well-aligned, we could optimize the DKC pulse amplitude and duration with sequences akin to that shown in Figure 6.2. We first attempted to minimize the temperature of the BEC after delta-kicking, a measurement which requires observing the rate of expansion for an atom cloud over a long time-of-flight. Unfortunately, for such low

[2]Although a lattice can be used for delta-kick cooling, we preferred to apply the DKC pulse as a traveling wave. For this reason the retro-mirror is blocked during the actual cooling sequence.

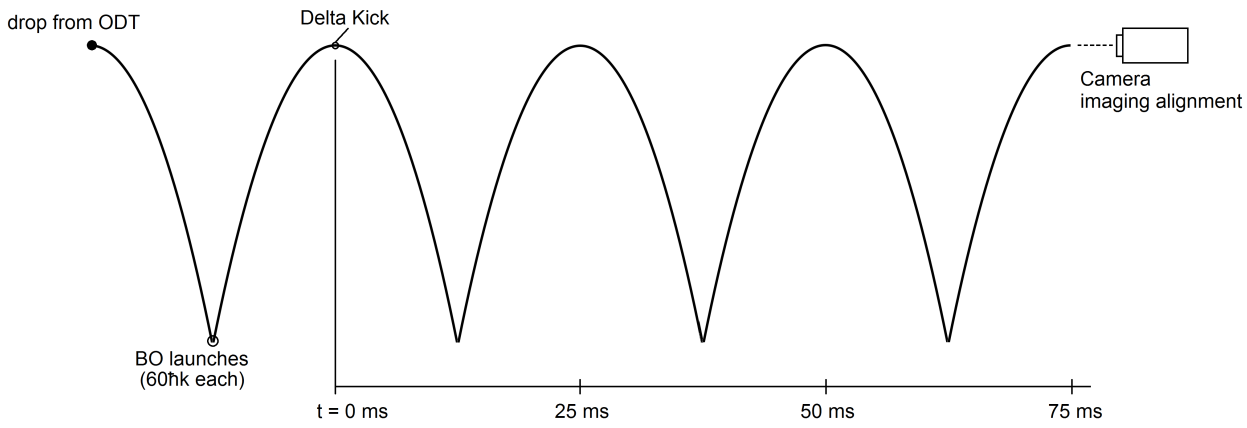

Figure 6.2: A space-time diagram for a vertical launch, delta-kick cooling, and subsequent time-of-flight. The total TOF may be arbitrarily increased by continually relaunching the atoms (limited only by the BO efficiency). This scheme was chosen because it solves the problem of the BEC falling out of view of our camera when imaging along the horizontal axis. While multiple relaunches is generally unfeasible for an interferometer sequence, as discussed in the text, this option is ideal for characterization of the DKC (e.g. through a temperature measurement) or other such cases where viewing the atoms over a large range of TOFs is desirable.

temperatures as we were trying to achieve, the time-of-flight needed to make an accurate measurement was longer than we could reach (limited by BO efficiency of relaunches). Our best temperature measurements through this conventional method all included zero within one standard deviation.

Returning to the analogy of light propagating through a material lens, an object distance x_o from a lens of focal length f will give rise to an image at x_i beyond the lens. Likewise our optical lens of focal strength δt may be applied at some time t_o to image the original atom cloud at a time t_i beyond the point of the delta-kick. If we characterize the lensing force as ΔF^2 and vary the strength of the lens, then the imaged cloud size as a function of δt can be written as [36]

$$\Delta x_i^2 = (\Delta x_i)_{\min}^2 + \frac{1}{m^2}\Delta F^2 t_i^2 \left(\delta t - \delta t_{\min}\right)^2 \tag{6.3}$$

where m is the particle mass and $\delta t_{\min}$ is the duration of the DKC pulse which will properly focus the cloud size to $(\Delta x_i)_{\min}$ at time t_i after the pulse. This dependency is exemplified

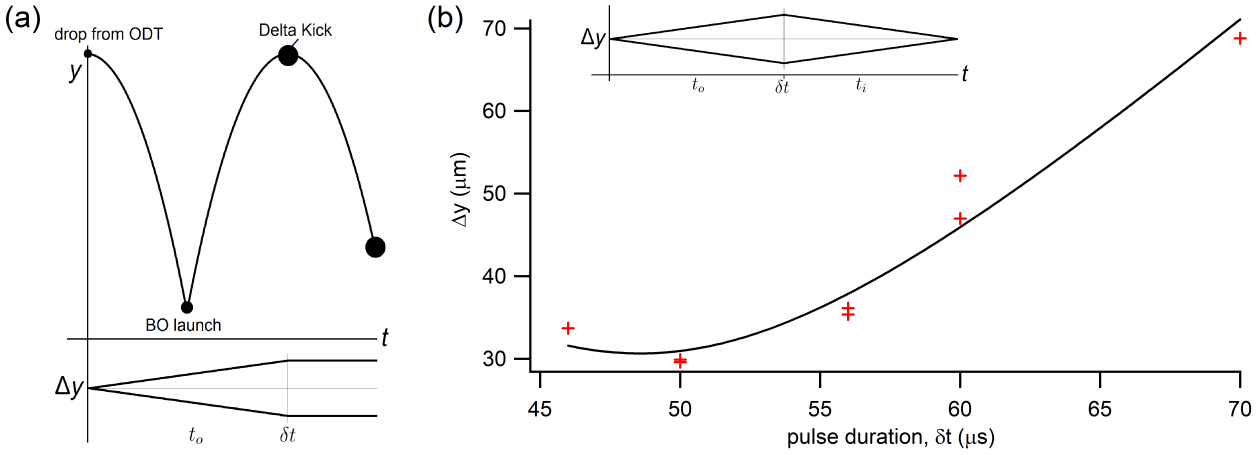

Figure 6.3: Optimization of delta-kick cooling within our experimental system. (a) Space-time diagram showing the trajectory of the atom cloud as well as its size. For a properly tuned delta-kick, the expanding matter wave can be collimated. (b) Measurement of refocused atom cloud size while varying the lens focal strength with δt. Inset illustrates the refocusing of the matter wave using a DKC lens for this measurement. Data are fit by a hyperbola in accord with Equation (6.3), yielding a minimum size of 30.6 ± 2.0 μm at a lens duration of 48.6 ± 1.9 μs. The DKC beam power here was approximately 22 mW.

in Figure 6.3 for which experimental parameters were chosen as $t_o = 25$ ms, $t_i = 70$ ms, and $(\Delta x_i)_{\text{min}}$ was determined to be 30.6 ± 2.0 μm at a lens duration of 48.6 ± 1.9 μs.

Again similar to the behavior of Gaussian laser beams, we know that our matter wave will not remain collimated over an infinite extent—rather, it will eventually approach some finite divergence angle which is inversely related to the beam's waist size. In fact, the minimum cloud size achieved by our lens tells us the upper bound on the minimum velocity spread, $(\Delta v_\ell)_{\text{bound}}$, under collimation conditions [36].

$$(\Delta v_\ell)^2_{\text{bound}} \equiv \frac{(\Delta x_i)^2_{\text{min}}}{t_i^2} = \Delta v_\ell^2 + \delta A \gtrsim \Delta v_\ell^2 \tag{6.4}$$

where δA accounts for the equivalent of lens aberrations and Δv_ℓ is the RMS velocity of the atoms after application of the lens. Through a simple relation based on the equipartition theorem, we can also set an upper bound on the minimum achievable temperature, $T_{\text{bound}} \equiv m\,(\Delta v_\ell)^2_{\text{bound}}\,/k_{\text{B}}$. According to our measurement and with our experimental parameters we

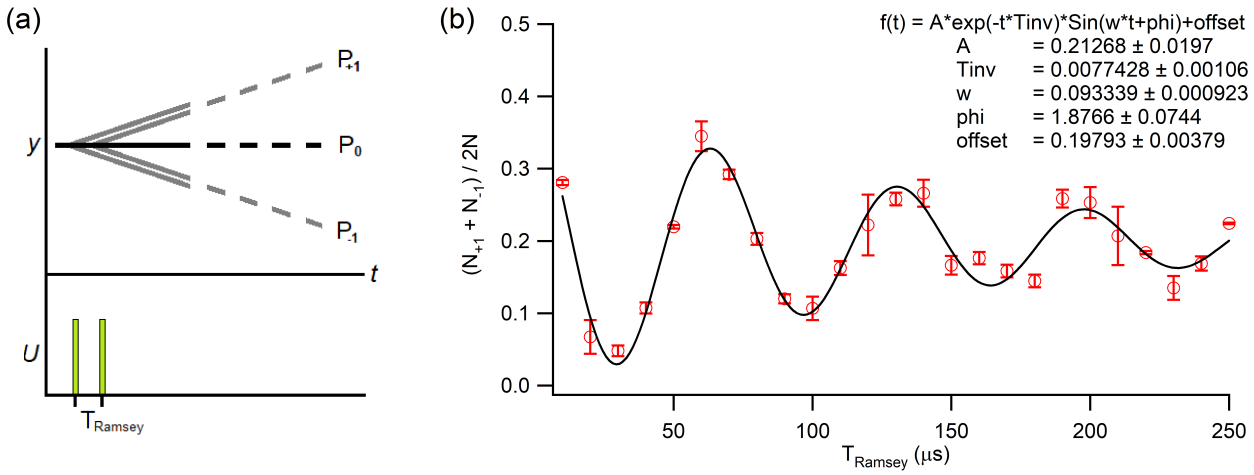

Figure 6.4: Momentum-space Ramsey interferometer to measure the BEC coherence length following DKC. (a) Pulse sequence and space-time diagram. (b) The average fraction of atoms in the $\pm 2\hbar k$ states (i.e. $\pm 1^{\text{st}}$ order) is plotted as a function of the time between Kapitza-Dirac pulses. Data were fit to a sinusoid with an exponential envelope as shown in the inset. From these the coherence time was determined to be 129 ± 18 μs.

found $T_{\text{bound}} = 4.0 \pm 0.5$ nK for our system.

6.2.3 Coherence Length Measurement

Although this value for T_{bound} is comparable with the value we obtained by horizontal ODT painting for horizontal interferometry [53], we desired additional evidence that our delta-kick cooling could produce an ultracold sample suitable for vertical interferometry. To this end we chose to characterize the effectiveness of our DKC pulse with a momentum-space Ramsey interferometer. The composition of such a Ramsey interferometer sequence is simply two short Kapitza-Dirac diffraction pulses separated by a variable time, T_{Ramsey}, during which the different momentum-state wave packets would evolve phase at different rates. Following the second of the two beamsplitting pulses the atoms' amplitude in each state adds constructively or destructively, depending on the relative phase acquired. One peculiarity, which is key in this application, is that this interferometer does not have a "reflection" pulse—that is, at sufficient time after the initial pulse the different momentum states will no longer be spatially

overlapped, such that there will never be a proper interference between these states and those produced by the second pulse. Only at short times will there be observable fringes while the various wavefunction components remain sufficiently overlapped. This effectively describes the region of the BEC over which the matter wave is coherent, aptly labeled therefore as the "coherence length".

In our experiment we used square Kapitza-Dirac pulses as the beam splitters, which allowed us to bring T_{Ramsey} very nearly to zero. The $2\hbar k$ separation between each momentum state results in fringe oscillations at a frequency $4\omega_{\text{rec}}$ as shown in Figure 6.4, wherein we may proclaim a rough incidental measurement of $\omega_{\text{rec}}/2\pi = 3.71 \pm 0.04$ kHz determined from the fit. The coherence time[3] of the observed fringes was extracted from an exponential envelope and found to be 129 ± 18 μs as a result of the delta-kick. This value is more than a factor of 5 improved upon the Ramsey coherence time of the BEC without DKC, measured as 23 ± 3 μs, and appears on par with the coherence times of our past CI experiments [31, 53, 33, 54] all in horizontal geometry.

6.3 Conjugate Mach-Zehnder Interferometer

I will now briefly digress into what was at one point intended to be the culmination of my work. Having just completed our magic depth demonstrations (and before installing delta-kick cooling) the direction of the experiment was leaning towards performance of large momentum transfer in a vertical interferometer using magic-depth Bloch oscillations, where the phase stability of such acceleration pulses could be exploited. We elected to continue use of the simple Mach-Zehnder geometry for this project; however, since the duration required to apply large quantities of BOs would be large compared to the timescale of vibrations, the planned interferometer was modified to become a vibration-insensitive conjugate Mach-Zehnder arrangement (such as may be used for gravity gradiometry [63]). In the typical

[3]Coherence size and coherence time (both sometimes referred to as coherence length) in this context are generally interchangeable, since the two are rather simply related by the velocity difference between the interfering momentum states.

Mach-Zehnder interferometer introduced in Chapter 1, mirror vibrations affect the lattice phase, and thereby the readout phase, in an unknown and unpredictable manor. The conjugate, or "double", Mach-Zehnder geometry (depicted in Figure 6.5) removes this potential liability by its design—the phase shifts from vibrations cancel within the total interferometer phase $\Delta\Phi = \Delta\phi_B - \Delta\phi_A$, where e.g. $\Delta\phi_A = \phi_{1,A} - \phi_{2,A} + 3\phi_{R,A}$ in accord with Equation (1.3).

Because the impact of vibrations on each measured $\Delta\phi_A$ and $\Delta\phi_B$ varies between each experimental run, the usual oscillation of population amplitudes will not be visible. In other words, interference patterns for individual Mach-Zehnder interferometers such as in Fig. 1.1(b) and Fig. 5.7(b) would have a random phase added to each data point, completely obfuscating the fringes. A new method for phase extraction becomes necessary in the regime of large T. Fortunately in the double Mach-Zehnder interferometer the phases $\Delta\phi_A$ and $\Delta\phi_B$ are correlated, so when the populations of similar output ports from different sub-interferometers are plotted against each other the result is an ellipse [17]. The visibility of such signals can be associated with the length of the major axis, while the total interferometer phase $\Delta\Phi$ is determined by the eccentricity and the orientation of the major axis. For example, consider the case where $\Delta\Phi = 0$. This implies $\Delta\phi_A = \Delta\phi_B$, resulting in an eccentricity $e \to 1$ and the major axis along the line $y = x$. Then for $\Delta\Phi = \pi/2$ we would observe a circle ($e = 0$) and for $\Delta\Phi = \pi$ we would again have $e \to 1$ but with the major axis along $y = 1 - x$. There is of course some ambiguity when extracting the phase, akin to determination of the phase from a single point on a sinusoid; however, with enough data over an appropriate range, the value of $\Delta\Phi$ can be correctly known to within some multiple of 2π.

Our conjugate Mach-Zehnder interferometer sequence was performed with a vertical lattice using exclusively third-order Bragg π– and $\frac{\pi}{2}$–pulses. At this time we were still using the AGB for cooling, rather than DKC, so we found it necessary to apply a "clean-up" pulse which would narrow the velocity distribution through the velocity selectivity of the Bragg resonance. Next a $\frac{\pi}{2}$–pulse was used to generate two coherent sources for the double interferometer geometry. These two wave packets were allowed to separate by an amount $6v_{\mathrm{rec}}\Delta t$,

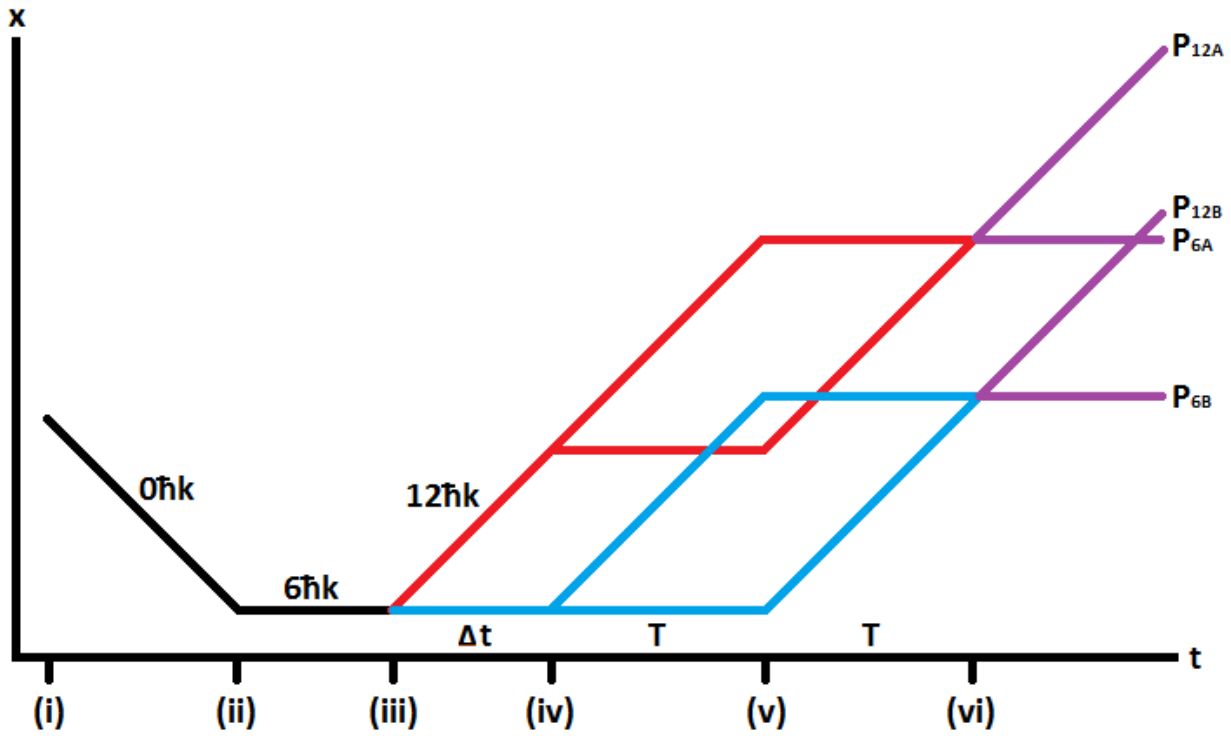

Figure 6.5: Space-time diagram showing a typical geometry and sequence for a vertical double Mach-Zehnder interferometer, shown in the accelerating frame of a falling BEC. (i) The condensate is dropped and labeled as $|0\hbar k\rangle$. (ii) A third-order Bragg pulse accelerates some atoms upwards, serving to narrow the velocity distribution. The remaining $|0\hbar k\rangle$ atoms are henceforth ignored. (iii) A Bragg $\frac{\pi}{2}$–pulse splits the atoms into an equal superposition of $|12\hbar k\rangle$ and $|6\hbar k\rangle$, separating into interferometers A and B, respectively. (iv) Allowing for some separation time Δt, another $\frac{\pi}{2}$–pulse splits the atomic wavefunction again. (v) After propagating for time T, a Bragg π–pulse reflects the diverging paths. (vi) After another time T, the sub-interferometer paths spatially overlap and a standing-wave readout $\frac{\pi}{2}$–pulse is applied. The populations at each output port are measured by absorption imaging after some time-of-flight and are labeled by their final momentum as well as their interferometer of origin, A or B, as shown.

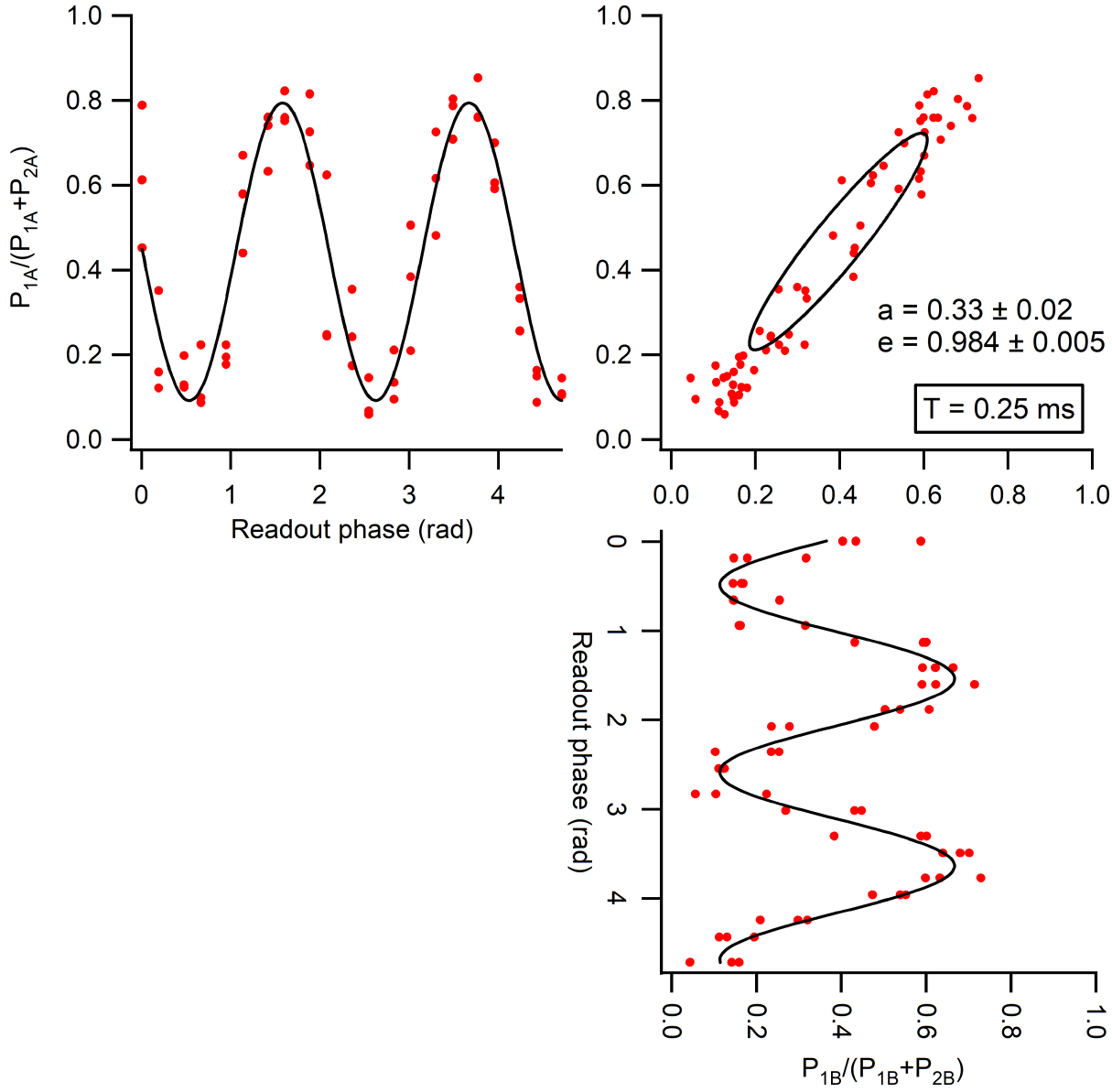

Figure 6.6: Exemplary ellipse signal for a double Mach-Zehnder interferometer. The oscillating populations in the $|12\hbar k\rangle$ output port are plotted versus the readout lattice phase for the two sub-interferometers (left and bottom). An ellipse can then be formed by plotting these populations against each other (top-right). All black curves are best fit sinusoids or ellipses. For this experiment $\Delta t = 3$ ms and $T = 0.25$ ms, and the single-photon detuning of the diffraction beams was $\Delta = +3500\Gamma$.

for which there was a constraint that Δt be large enough for the interferometer paths of like-momentum to appear spatially resolved in our absorption images (since their separation could not be increased by time-of-flight). Finally, a typical Mach-Zehnder pulse sequence was applied, resulting in output ports with momentum states $|6\hbar k\rangle$ and $|12\hbar k\rangle$ relative to the accelerating frame of the original falling condensate. The populations of these states would be obtained by counting the number of atoms in each separated cloud within an absorption image.

With this arrangement we aimed at first to demonstrate the ellipse signal in a regime of minimal vibrations. For our apparatus vibrations are typically observed around and below the 1 kHz level, so we chose to begin with $T = 0.25$ ms. We also set $\Delta t = 3$ ms for all of the double Mach-Zehnder experiments in accord with the constraint mentioned above. Our first demonstration is shown in Figure 6.6, in which the individual oscillations of the different populations remain clear due to negligible vibration effects. Note that because interferometers A and B are sourced by opposite states, the more generally labeled P_{1A} (P_{2A}) corresponds with P_{12A} (P_{6A}) in Fig. 6.5 while P_{1B} (P_{2B}) corresponds with P_{6B} (P_{12B}). Here the fitted ellipse was obtained by converting the data to polar coordinates and performing a simple least-squares regression analysis using the function

$$r = \frac{a(1-e^2)}{1 + e\cos(\theta - \theta_0)} \tag{6.5}$$

for an ellipse with one focus at the origin. This form was chosen (instead of one which places the center at the origin) since it is a well-defined function at all values and avoids the sign ambiguity of square roots. A routine for minimizing the reduced chi-squared resulted in the displayed fits. The total interferometer phase can be extracted from the eccentricity by the relation

$$\Delta\Phi = \cos^{-1}\left(\frac{e^2}{2-e^2}\right) \tag{6.6}$$

defined over one-quarter period. Because the separation of the two sub-interferometers is quite small in this case, we expected that the phase contribution from a gravity gradient

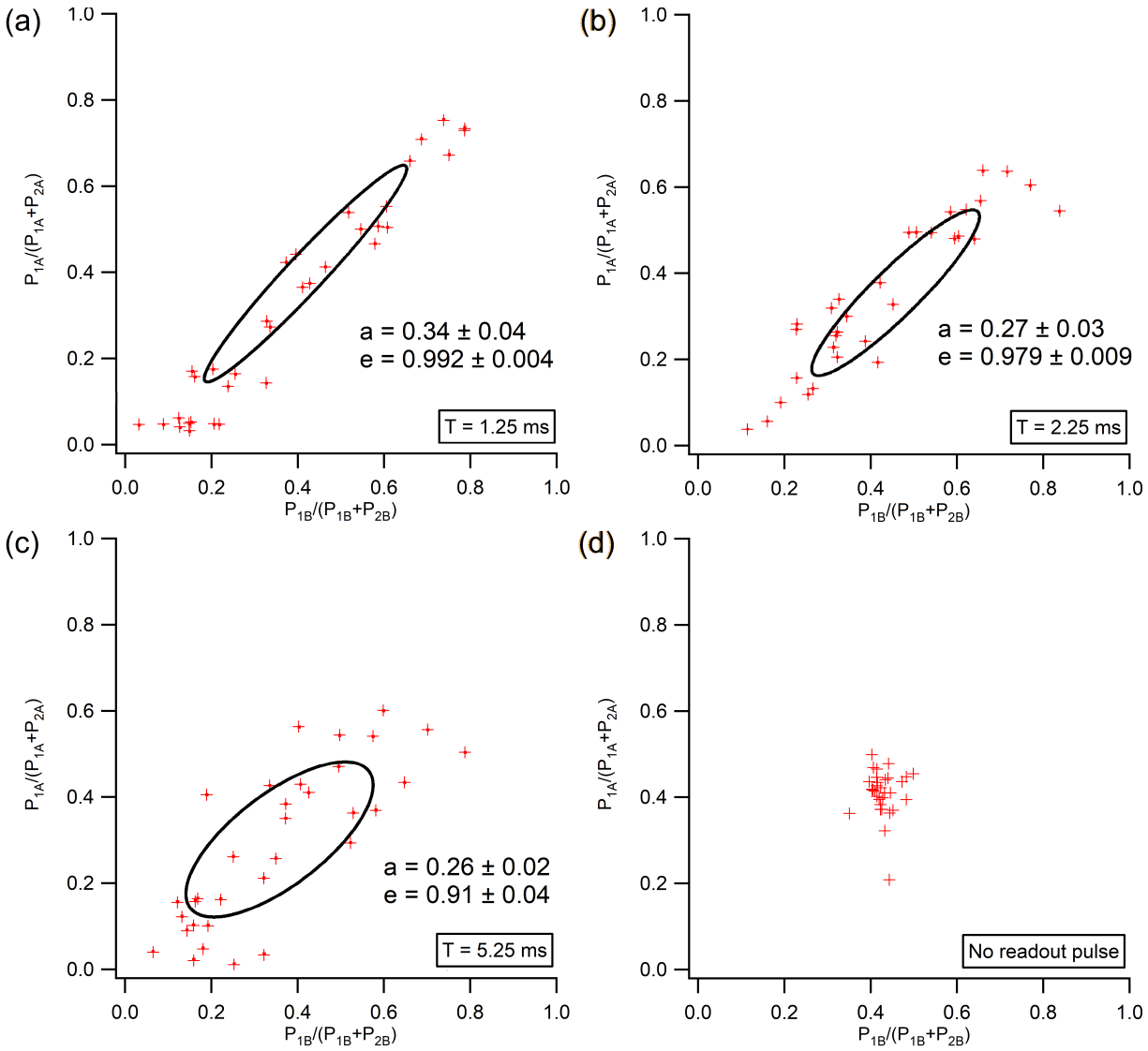

Figure 6.7: Ellipse signals at various values of T for a double Mach-Zehnder interferometer. (a-c) Showing the trend of ellipse signals for propagation times $T = 1.25$, 2.25, and 5.25 ms, respectively. Black curves are best fit ellipses for each data set. (d) Data for an incomplete interferometer, demonstrating that the asymmetry of populations around 0.5 was not introduced by the path interference and was therefore likely inconsequential. For all of these experiments $\Delta t = 3$ ms and the single-photon detuning of the diffraction beams was $\Delta = +3500\Gamma$.

should be negligible[4], resulting in $\Delta\Phi$ nearly zero ($e \to 1$) as observed.

Next we began to push into the vibration-afflicted regime. The total interferometer time was increased by over an order of magnitude, with values of $T = 1.25$, 2.25, and 5.25 ms (see Figure 6.7); however, the ellipse shape remained robust despite a complete loss of visibility in the sub-interferometer population oscillations. One peculiarity of this data set was the asymmetry—the ellipses were not centered around 0.5 as one might expect. A subsequent data set was collected without applying a readout pulse (Fig. 6.7(d)) and the ellipse center was consistent with those previous. This suggests that the cause was simply a benign, imperfectly balanced splitting $\frac{\pi}{2}$–pulse. Another observation was that the eccentricity seemed to decrease slightly over this range of T, but it was inconclusive whether this appearance was due to a real change in $\Delta\Phi$ or just a general increase in noise.

6.4 Contrast Interferometer

Until now all contrast interferometry had been done using a horizontally-oriented optical lattice. With the vertical diffraction beams already set up for conjugate Mach-Zehnder interferometry, it was a natural move at this point to step back to contrast interferometry[5] and demonstrate sustained visibility over large interferometer times. We have already shown how excited-band Bloch oscillations reduce the level of lattice-induced phase noise, but they are generally slower than ground-band BOs. Thus the development of tools for long-time vertical contrast interferometry would allow incorporation of this phase-stable method of momentum transfer into a vibration insensitive interferometer.

The first hurdle towards vertical CI (after precise alignment of the diffraction beams, see

---

[4]For a sphere of radius R, we expect the gravity gradient over a distance Δz near the surface to be $\Delta g = \frac{2g\Delta z}{R}$. In our system $\Delta z = 6v_{\rm rec}\Delta t = 75$ μm for $\Delta t = 3$ ms. Letting $R = R_{\rm Earth}$ we have approximately $\Delta g = 2 \times 10^{-7}$ m/s^2. Finally, the double Mach-Zehnder interferometer phase depends on this gradient according to $\Delta\Phi = k\Delta g T^2$; thus, for our largest values of T this phase shift is only around 6×10^{-5} rad.

[5]Although we had intended to perform a large number of excited-band BOs within a conjugate Mach-Zehnder interferometer, the transfer efficiencies turned out to be insufficient for the magnitude of our desired demonstration. Thus, the plan was altered towards vertical contrast interferometry.

Sec. 3.1.2 and 3.1.3) was obtaining a BEC with a low velocity spread in the vertical direction. This arduous task consumed our efforts for several months, during which we attempted a variety of solutions previously discussed (including a shaped ODT, an anti-gravity beam, and delta-kick cooling). The most successful technique proved to be DKC and was covered most recently at the beginning of this chapter.

Following this achievement we became stalled by an inability to observe a CI signal on the photomultiplier tube (PMT) detector. To diagnose the problem, it was helpful to break down the signal detection process into three stages:

1. The designated readout beam needs to have optimal intensity and detuning and has to hit the BEC near the Bragg reflection angle.

2. The density grating formed by the BEC should have a long coherence length.

3. The reflected photons must be collectible by a PMT which has sufficiently low background noise.

The second step became possible with delta-kick cooling and was later experimentally confirmed, as shown in Figure 6.4. In the next sections I will discuss our progress towards obtaining the CI signal in relation to the remaining two points.

6.4.1 Readout Optics

When we first addressed the conversion from horizontal diffraction optics to a vertical configuration, our scope needed to include several other beam paths in the layout. Figure 3.2 illustrated the simplest set of optics necessary to understand how each of the different paths were incorporated. Spatial constraints forced the choices made for MOT and diffraction optics; however, the lenses used for readout beam manipulation and PMT photon collection underwent multiple revisions. In the earlier figure it is indicated that the readout beam, which is collimated coming out of a fiber, was designed to be focused at the atoms. This was

intended as a means for achieving an appropriate intensity at the atoms while minimizing the total beam power as advised from previous iterations of the experiment [31, 53]. In other words, readout beam light that does not address the atoms contributes only to noise on the PMT as back-scattered photons. This effect will be revisited in the next section as we discuss our attempts to reduce this level of noise, but for now we will simply chronicle the evolution of our readout beam optics arrangement.

To begin, I will describe our two main methods for aligning the readout beam to hit the atoms. A generally applicable and nearly infallible means of precisely positioning a laser beam to intersect a free-falling BEC of less than 100 μm in size is through imaging on a camera[6]. This of course requires near-resonant light, which may not be the case for the beam in question; however, if the light passes through a fiber at any point—most of ours do—then it is a simple task of inserting resonant light into the fiber temporarily for initial alignment. Successful absorption imaging in this manner ensures that beam must be hitting the atoms, as that very same light is being used to project the image of the atoms. Next, a method for improving upon initial alignment is one we refer to as "resonant blasting". This technique also uses near-resonant light, but absorption imaging is now directed along a different axis. The goal here is to maximize the disturbance (e.g. displacement and heating) of the atoms due to an increasingly optimal beam alignment.

Let us return now to the initial readout beam configuration depicted in Figure 3.2. We found that resonant blasting produced very different effects when performed at (i) about 2 ms after dropping the BEC, versus (ii) about 2 ms after the DKC pulse. In the latter case the disturbance to the BEC was significantly weaker. As may be seen in Figure 6.1, the atom cloud should be at the same location in both cases; only the cloud size should be different. Therefore we eventually concluded that the readout beam waist must be too small at the atoms' location, which led to the addition of lenses placed on the readout beam path

[6]This is, in fact, how most of our coarse beam alignment begins. In the case of beams such as the ODT, which are far off resonance and do not traverse a fiber, it is helpful to use a dichroic mirror to spatially overlap the beam along an imaging axis. Then the position of the beam on the camera may be aligned to the position of the atoms in a separate image.

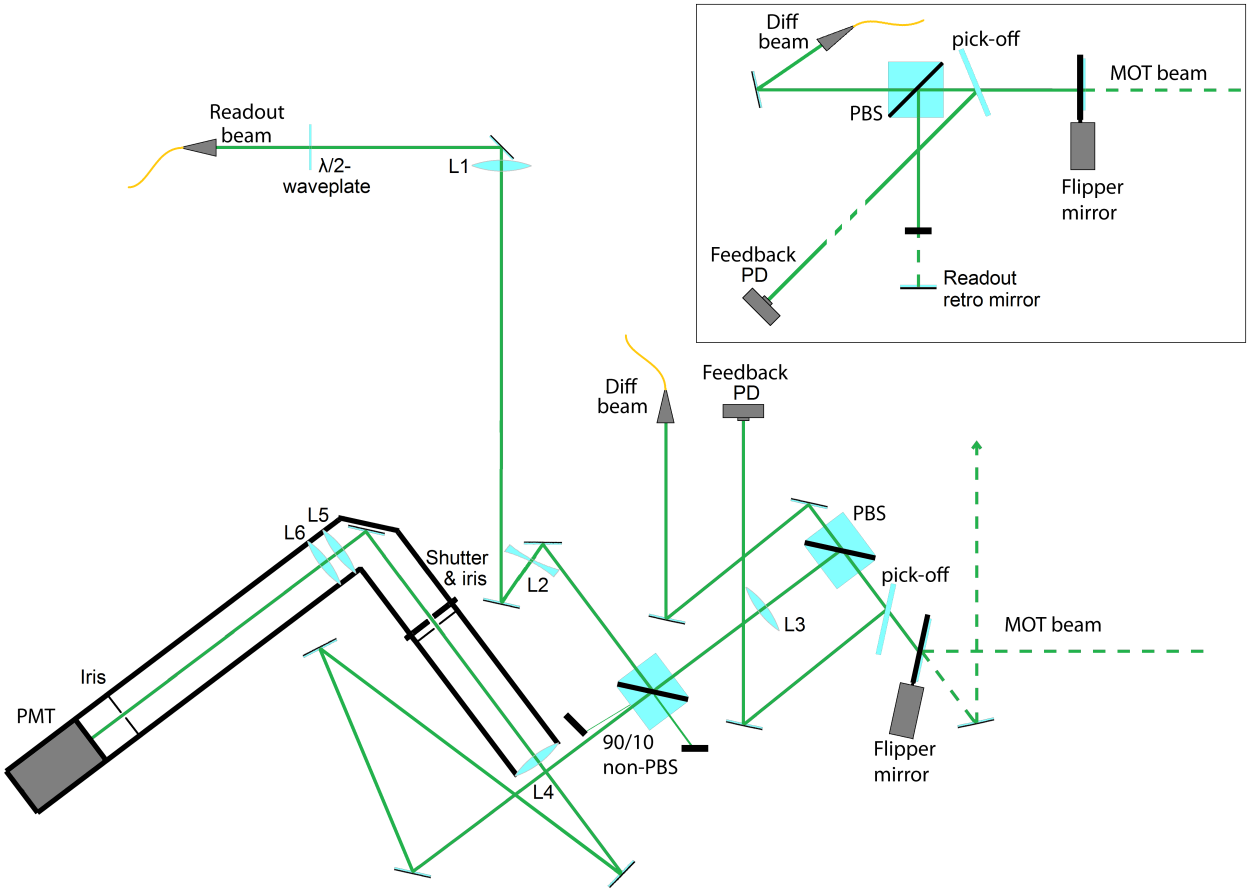

Figure 6.8: Final optics layout for vertical CI diffraction beams, readout beam, and signal collection. Components shown are primarily arranged on the optics table below the vacuum chamber (and BEC) while the inset portrays a portion of the breadboard above the chamber.

to increase the beam size (see Fig. 6.8).

In the figure portraying the final optics layout for vertical contrast interferometry, we may inspect how these changes affect the spot size and divergence properties of the readout beam. The three key elements here are lenses L1, L2, and L3. (There are also two 150 mm lenses not shown, between the flipper mirror and the atoms, forming a one-to-one telescope positioned as in Fig. 3.2.) The 150 mm lens L3 is from the original design and remains in the same location as before, while the two lenses L1 and L2, having focal lengths 400 mm and −100 mm respectively, have been introduced for flexible control of the beam size. Successive adjustments to the position of L1 allowed us to enhance the signal-to-noise ratio on the PMT by mode-matching the readout beam shape to the atom cloud. Lenses L4, L5, and L6 have focal lengths of 100 mm, 100 mm, and 200 mm, respectively, all of which are used for re-imaging the atoms through a pair of irises to enhance readout detection (discussed later).

Finally, similar to the setup in [31], the readout beam is inserted onto the diffraction beam path with a polarizing beam splitter, allowing nearly zero loss in power for the two propagating beams. Note that, unlike the blue readout used in [53], it is acceptable for the diffraction and readout beams to have differing polarization, since the dipole radiation pattern does not disallow any particular orientation for observing efficient reflection of signal photons.[7] Also, the readout beam is separated from the returning signal photons by a non-polarizing beam splitter which exhibits 90% transmission and 10% reflection efficiencies. This enables collection of many more signal photons (compared with, e.g., a 50/50 beam splitter) at the cost of needing ten times the readout light power; however, this is not a hindrance since typical readout pulses operate with only a few microwatts.

6.4.2 PMT Noise Reduction

The readout collection optics—following the 90/10 beam splitter—are housed entirely within a lens tube, which removes essentially all of the ambient light noise. Additionally, there is a

[7] This phenomenon caused trouble in the previous iteration of the CI experiment, and is detailed in [39].

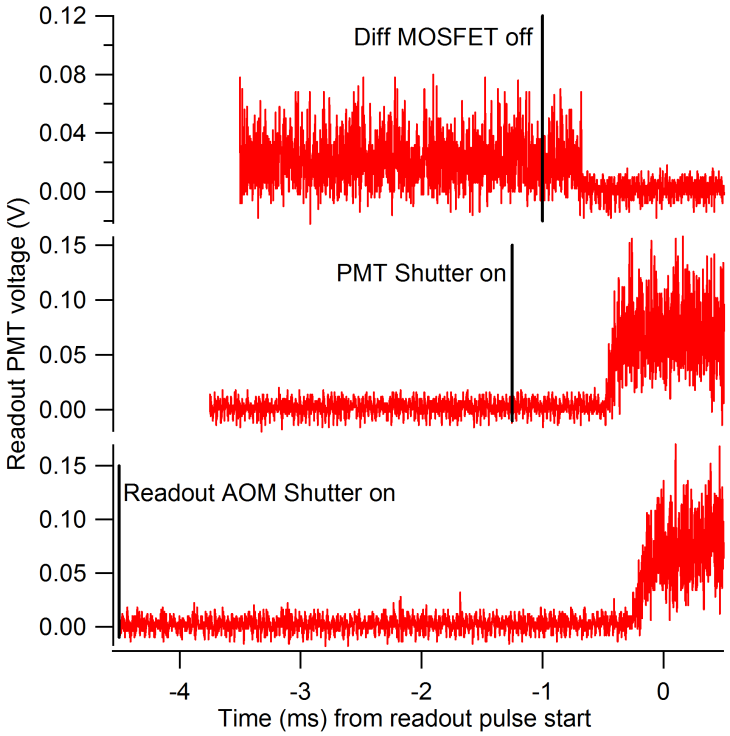

Figure 6.9: Shutter timings in relation to the readout pulse. For these tests the readout beam power was 14 μW, the PMT gain control was 0.9 V, and the amplifier gain was 200 μA/V with no low-pass filtering.

556 nm band-pass filter immediately in front of the PMT; thus, the primary sources of noise become the lattice beams and the readout beam. The diffraction beam originating on the upper breadboard (Fig. 6.8, inset) is the only one which shines directly into the PMT and was therefore the first problem to address.

Some of our interferometer sequences in the past had lattice pulses occurring only a few microseconds before the readout pulse. For this reason we believed a mechanical shutter on the lattice beams would not be fast enough, so instead we incorporated an electrical "shutter" into the RF electronics with a MOSFET. As we sought to bring the PMT noise down to an acceptable level, however, we acknowledged that the attenuation from the MOSFET was insufficient. This led to the addition of a mechanical shutter before the diffraction beam

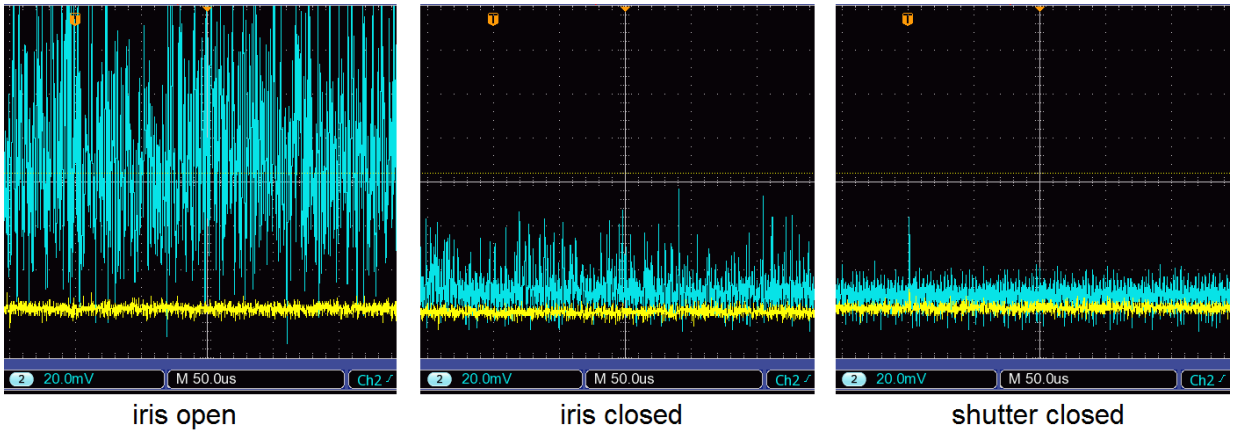

Figure 6.10: Reduction in light noise on the PMT: comparison of the final shutter and final iris. For these tests the readout beam power was 14 μW, the PMT gain control was 0.9 V, and the amplifier gain was 200 μA/V with no low-pass filtering.

fiber which could fully extinguish the light.

This means that the timings for each of the pulses become a little less flexible. We already had a mechanical shutter installed within the PMT lens tube, and the readout beam had its own shutter at this time as well. Each shutter had a unique delay time between when it was triggered from Cicero and when it actually opened or closed over its respective beam. This necessitated the use of pre-triggers (a.k.a "pulses" in Cicero), with timings indicated in Figure 6.9. Note that, although the delay is unique for each shutter, the rise/fall time is less than or approximately equal to 0.5 ms for all of them. Consequently, there is now imposed a minimum time of 1 ms between the readout pulse and the final lattice pulse of an interferometer sequence.

With the shutters installed and the timing constraints implemented into Cicero, the only source of noise that remained during the readout pulse came from the readout beam itself. To ensure that no specular reflections found their way to the PMT, we made sure to position each of the readout optics with a slight tilt. Diffuse reflections could not be so easily removed, but their effect could at least be reduced by repeated imaging and irising of the returning signal photons. In Figure 6.8 two irises can be seen within the lens tube configuration—these

are placed approximately at focal points along the signal path.

By temporarily replacing the PMT with our camera, we could image the atoms and ensure that the BEC is visible through the irises. This implies that the signal photons should be visible when returning to the PMT[8]. Even if the PMT detector does not perfectly replace the camera chip in the same plane, we can remain confident in the robustness of our alignment because the PMT detector is 8 mm in diameter compared with the camera chip of only 4.8 mm $\times$ 3.6 mm. Using the camera we aligned the position of the atoms to be simultaneously centered through the iris and in the middle of the CCD detector. This allowed us to nearly close the iris such that the undesired diffuse scattered light would be apertured and the PMT background noise level reduced. Following several iterations of these alignments, we eventually reached an acceptably low level of noise to begin looking for CI readout signals in earnest.

6.4.3 Readout Signal

Once our noise level was low enough to resolve individual photons, we could more easily adjust our electronic amplification and filtering settings to match the observations in our previous work [54, 53]. When the transimpedance amplifier was set to 10 μA/V with a 1 MHz low-pass filter we found a significant reduction in the high frequency noise; however, this solution primarily addressed outstanding electronic noise—the level of light noise remained. Nonetheless, we finally began detecting the signature oscillations of a CI readout signal.

While other vertical heterodyne interferometric measurements have already been demonstrated [9] in a different geometry, ours are the first vertical CI readout signals. Unfortunately the signal-to-noise is very low (less than one) for any individual run at the moment, but strong phase stability allows for the averaging of several runs to yield coherent addition of oscillations to above the level of the background. This can be observed for the exemplary data provided in Figure 6.11(b), which is an average of 25 experimental runs. For that par-

[8]This assumption is true as long as aperturing of stray light, e.g. with an iris, only occurs at points where the atoms may be properly imaged.

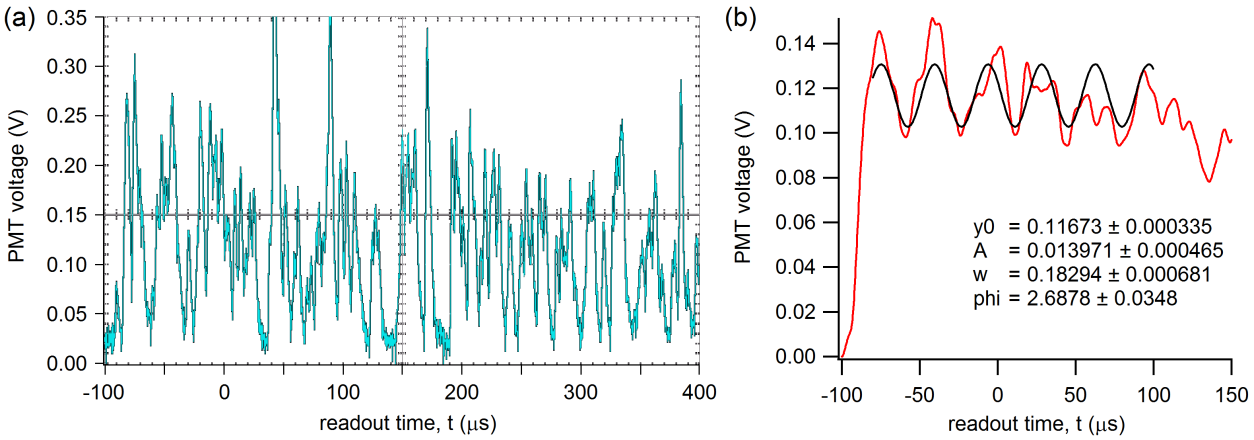

Figure 6.11: Exemplary vertical contrast interferometer readout signal. Shown are signals obtained from (a) a single run and (b) an average of 25 experimental runs with additional low-pass filtering at 100 kHz. The black curve in (b) is a best fit with functional form $y = y0 + A\sin(wt + phi)$, returning a fit visibility of 12%. For all of these experiments, the PMT gain control was 1.01 V and the amplifier gain was 10 μA/V with a 1 MHz low-pass filter. The single-photon detuning of the readout beam was $\Delta = -42.6\Gamma$.

ticular data set (one of our best so far) the fit function returned a signal visibility of 12%. As an alternative means for characterizing the phase stability, we followed the Fourier fitting method prescribed in [53] for picking out the phase of each individual signal. From these we found the standard deviation in the measured phases to be 624 mrad.

We are of course continuing to improve the signal amplitude, which should help increase the visibility and reduce fit error of the extracted individual phases. An inconvenient laser failure halted our progress at this point, but with the return of that system we plan to focus on increasing atom number—a parameter that should yield quadratic growth of the CI signal amplitude. (The quantity of atoms participating in the interferometer had not been our foremost concern while performing readout beam alignments.) Furthermore, increasing atom number will eventually become even more necessary since prospects of longer CI times will likely require a second BO launch, during which additional atoms will inevitably be lost due to finite inefficiencies.

Chapter 7

MULTIPATH LANDAU-ZENER-STÜCKELBERG INTERFEROMETRY

As we were optimizing parameters for the Bloch oscillation launch (as described in the previous chapter), we also began exploring the BO efficiency at large lattice depths outside the regime where the Landau-Zener formula could be expected to work. Momentum transfer with ground-band BOs is typically carried out at high lattice depths, a regime where we have a well-established Bloch-band picture to compare diffraction phase but not transfer efficiency. The motivation here was to see how P_{LZ} as a metric for BO efficiency is altered at high depth, i.e., is it more efficient or less efficient than the Landau-Zener formula would predict. However, among some plots of BO efficiency versus BO period (similar to what had been done in Fig. 5.7(b)) there was a data point far below the rest. To ensure that this initial observation was not simply noise or a statistical outlier, we collected a more dense set of data around these features and found that we had unexpectedly stumbled upon Landau-Zener-Stückelberg (LZS) resonances.

7.1 Multipath LZS Experiments

Although we did not immediately associate our observations with the aforementioned Landau-Zener-Stückelberg interferometry[1], we did quickly determine that the drops in the BO efficiency were due to an interference between atoms traveling in different lattice bands. The first LZS interferometers using cold atoms [34, 69] were two-path interferometers; however, the fact that we see multipath interference for many BOs opens the opportunity to apply

[1]The model we developed to describe multipath LZS interferometry underwent multiple revisions as we sought to improve its accuracy each time it failed to align with new data. These will be discussed in more detail in the following sections.

them towards metrology. During a single Bloch oscillation, each time the atomic wavefunction nears an avoided crossing it has a probability to tunnel into the adjacent band, given by the Landau-Zener tunneling probability,

$$P_{\mathrm{LZ}}^{(b)} = \exp\left(-\pi \frac{\Omega_{\mathrm{BG}}^2}{2b\dot{\delta}}\right) = \exp\left(-\pi \frac{\Omega_{\mathrm{BG}}^2}{2b} \frac{T_{\mathrm{BO}}}{8\omega_{\mathrm{rec}}}\right) \tag{7.1}$$

with some terms slightly redefined from Equation (5.1). The probability (i.e. efficiency) of performing N_{BO} oscillations in, for instance, the ground band is then $(1 - P_{\mathrm{LZ}}^{(1)})^{N_{\mathrm{BO}}}$ which is in clear disagreement with our observations in Figure 7.1. This discrepancy arises from the fact that the piece of the wavefunction "lost" during a previous BO may tunnel back into the primary band (in this case, $b = 0$). The phase difference acquired between these two paths in quasimomentum space is dependent only on the average band gap, $\langle \Delta E \rangle$, and the Bloch period, T_{BO}. We would later recognize this as the Stückelberg phase [64],

$$\begin{aligned} &\phi_{\mathrm{S}} = \tfrac{1}{\hbar} T_{\mathrm{BO}} \langle \Delta E \rangle \\ &\text{where} \quad \langle \Delta E \rangle = \tfrac{1}{2\hbar k} \textstyle\int_{-\hbar k}^{+\hbar k} \left(E_1(q) - E_0(q)\right) \mathrm{d}q \ . \end{aligned} \tag{7.2}$$

The above formula allowed us to accurately corroborate the locations in Figure 7.1 for each first LZS resonance (observable for $U \geq 6\hbar\omega_{\mathrm{rec}}$) and the second LZS resonances ($U \leq 4.5\hbar\omega_{\mathrm{rec}}$), i.e., where the conditions $\phi_{\mathrm{S}} = 2\pi$ and 4π are met, respectively. Note that all of our BO efficiencies were measured by counting atoms in time-of-flight absorption images, so the range of each data set was partly influenced by a limited total efficiency $\lesssim 5\%$.

After our initial observations we began to characterize a LZS resonance by its dependence on the number of Bloch oscillations, N_{BO}. In Figure 7.2 we found that increasing N_{BO} both boosted the amplitude and sharpness of the feature; although, this growth appeared to stagnate after about 20 BOs. This saturation can be rationalized as a steady state realization, where losses from the ground band have become equal to the returning population from the first-excited band.

Finally, we investigated a more specific dependence on N_{BO} in its parity (see Fig. 7.3). Landau-Zener-Stückelberg resonances over the course of multiple BOs have a near analogy

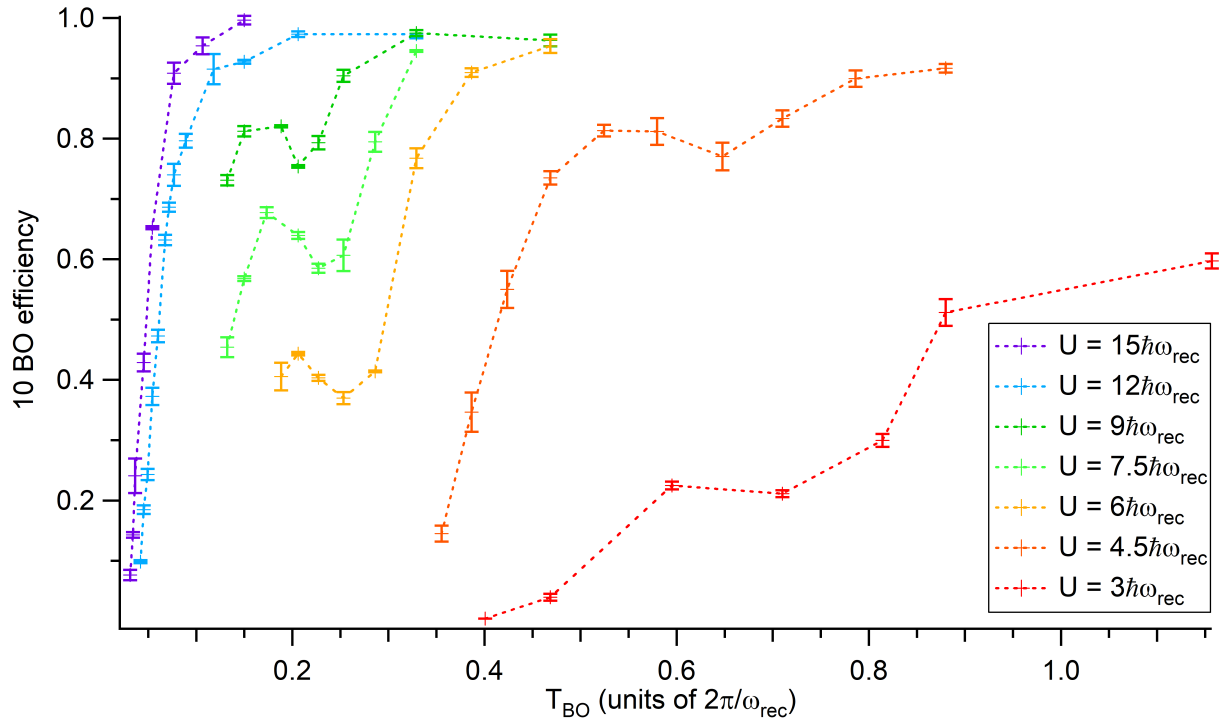

Figure 7.1: Total transfer efficiency of 10 BOs performed in the ground band, $b = 0$, where we found unexpected LZS resonances at various lattice depths. Dashed lines are provided as a guide to the eye. For all data shown, the BO intensity ramp time was 300 μs and the single-photon detuning of the diffraction beams was $\Delta = -3500\Gamma$.

with the quantum resonant effects of a delta-kicked rotor [15, 46]. In the quantum kicked rotor, particles are left to freely propagate between kicks; however, during Bloch oscillations the atoms evolve phase in the lattice rather than in free space. Also, in regular delta-kicked rotor experiments the energy difference between states is always a multiple of the same recoil energy, while this is not so for lattice band energies. Nonetheless we still see the same "resonances" and "anti-resonances" where, in our case, the Landau-Zener tunneling probability is enhanced or reduced, respectively. In regard to the parity of N_{BO}, delta-kicked rotors have also been shown to exhibit anti-resonances—that is, the average energy of the system does not grow as the number of kicks is increased. This suggests that in our experiments we may expect to observe little change in BO efficiency at the anti-resonance,

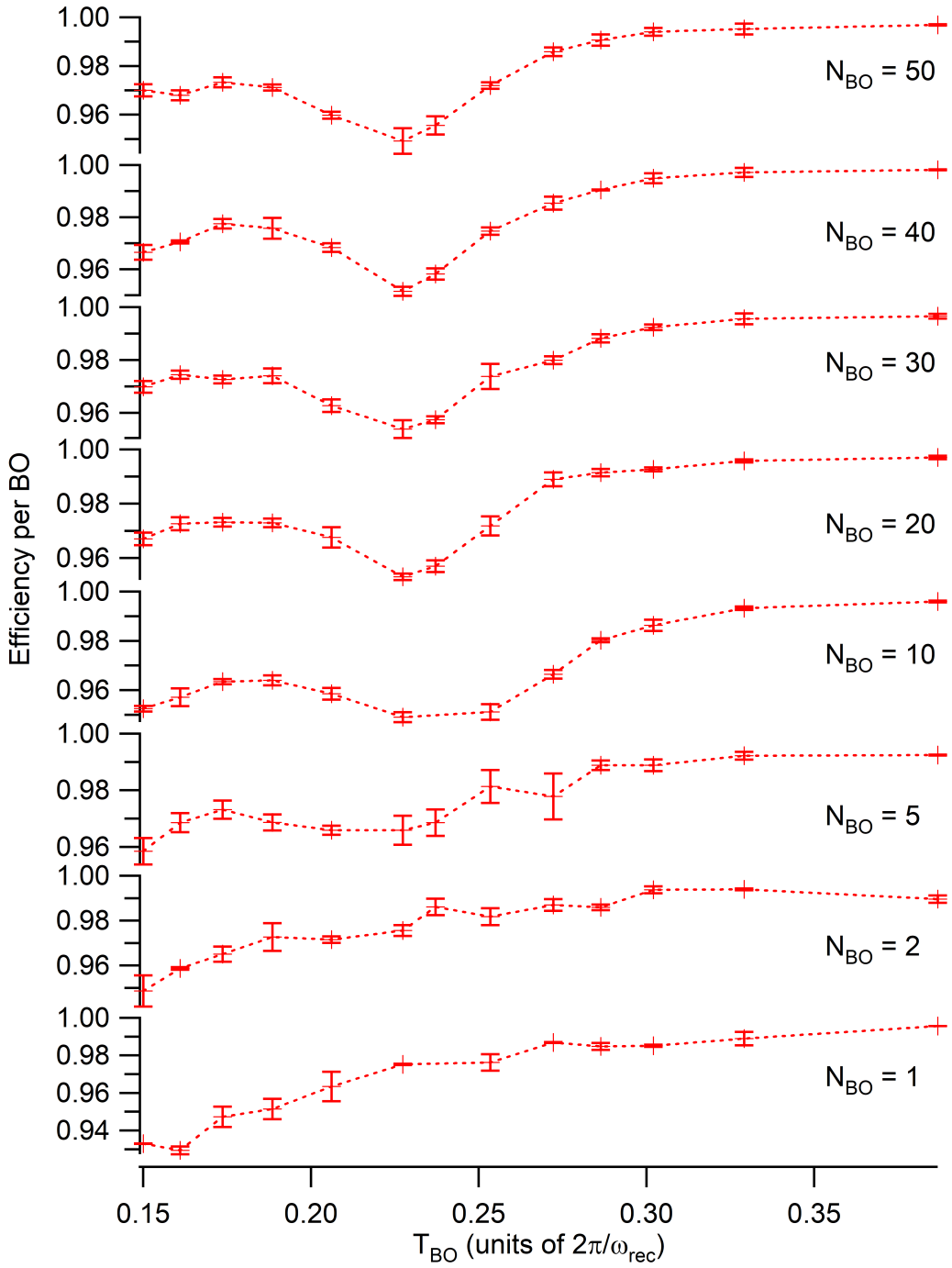

Figure 7.2: LZS resonances shown in the BO efficiency as a function of N_{BO}. Dashed lines are provided as a guide to the eye. For all data shown, BOs were performed in the ground band of a $7\hbar\omega_{\mathrm{rec}}$ deep lattice with intensity ramp times of 300 μs. The single-photon detuning of the diffraction beams was $\Delta = -3500\Gamma$.

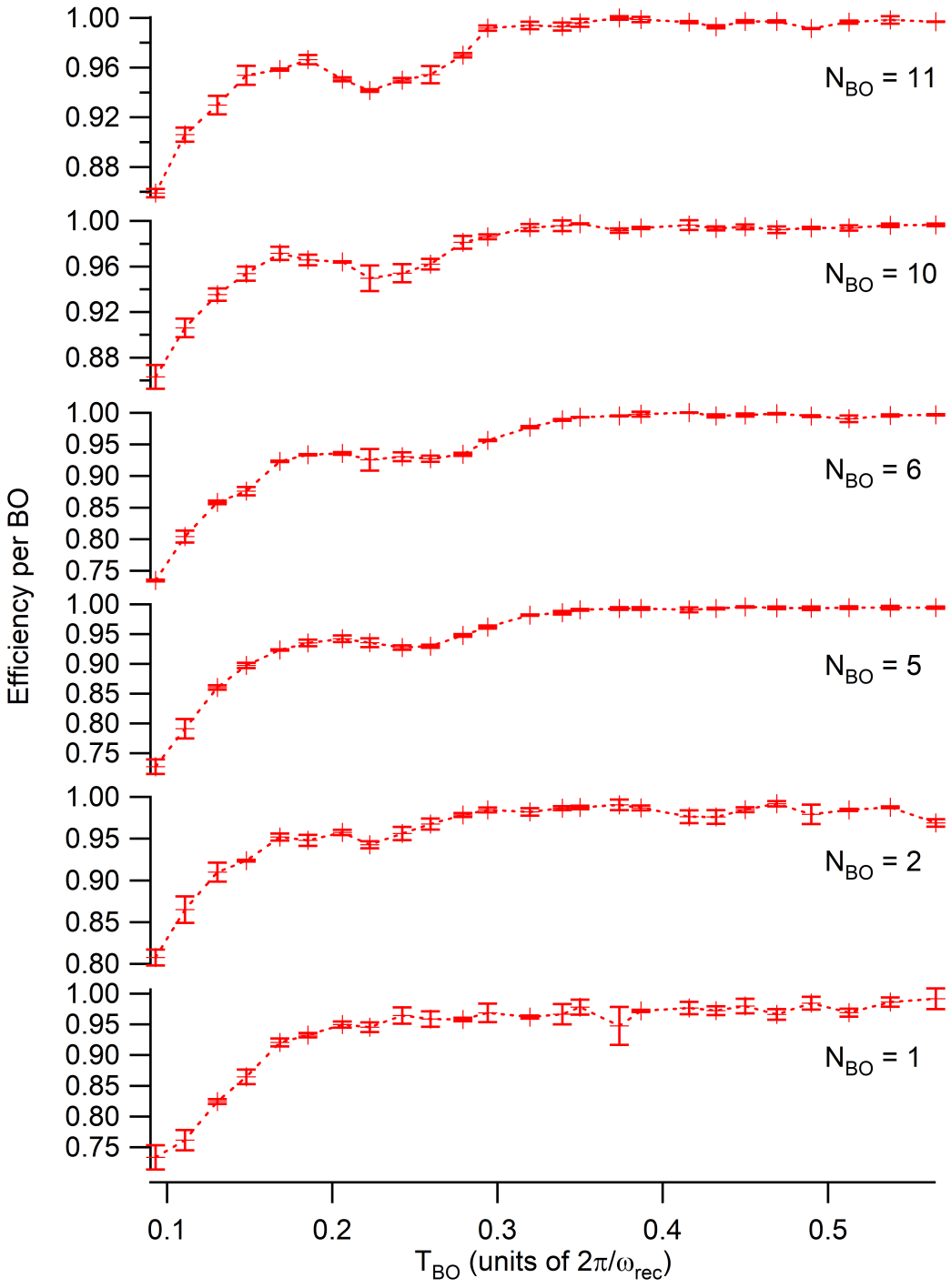

Figure 7.3: More LZS resonances in the BO efficiency to determine a dependence on the parity of N_{BO}. Dashed lines are provided as a guide to the eye. For all data shown, BOs were performed in the ground band of a $6\hbar\omega_{\mathrm{rec}}$ deep lattice with intensity ramp times of 300 μs. The single-photon detuning of the diffraction beams was $\Delta = -3500\Gamma$.

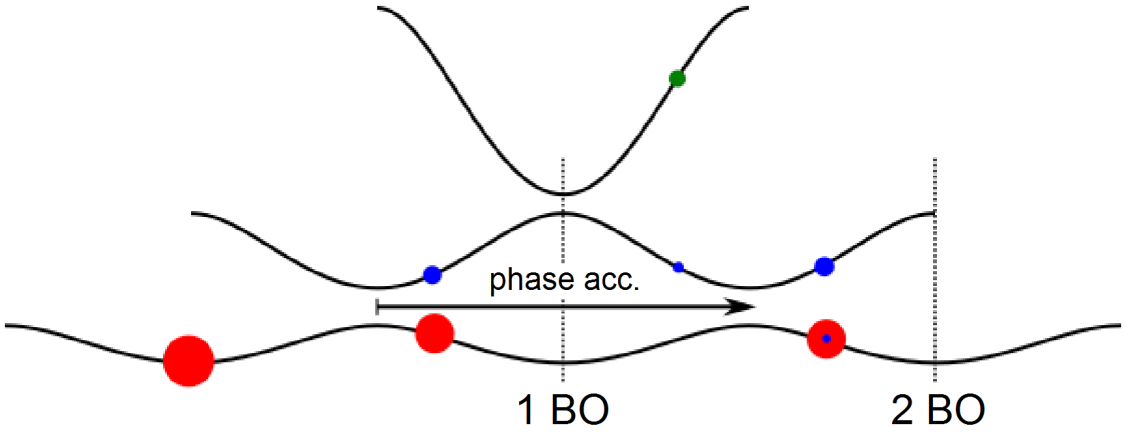

Figure 7.4: Ground-band Bloch oscillations as a two-path (red and blue) LZS interferometer in the extended Brillouin zone.

while at the resonance we should see a dropping efficiency for greater numbers of Bloch oscillations.

7.2 Simple $N_{\mathrm{BO}} = 2$ Model

For one to observe strong LZS interference during ground-band Bloch oscillations it is necessary to satisfy certain constraints on various Landau-Zener tunneling probabilities. After passing through the first avoided crossing, the fraction of atoms transmitted to the first-excited band is $P_{\mathrm{LZ}}^{(1)}$ while the rest remain in the ground band. Around the completion of the first BO, the wavefunction component in $b = 1$ will lose some population to $b = 2$, resulting in $P_{\mathrm{LZ}}^{(1)}(1 - P_{\mathrm{LZ}}^{(2)})$. Then upon conclusion of the second BO, the populations in the bottom two bands will exhibit interference. Therefore, strong interference should be observable when satisfying $0 \sim P_{\mathrm{LZ}}^{(1)} \ll P_{\mathrm{LZ}}^{(2)} \ll P_{\mathrm{LZ}}^{(3)} \sim 1$. In other words: $P_{\mathrm{LZ}}^{(1)}$ is just large enough to appreciably populate both $b = 0$ and $b = 1$, $P_{\mathrm{LZ}}^{(2)}$ is not too large so as not to lose much to $b = 2$, and $P_{\mathrm{LZ}}^{(3)}$ is nearly equal to one such that any atoms at or beyond $b = 2$ are effectively lost from the system.

For this $N_{\mathrm{BO}} = 2$ model, depicted in Figure 7.4, we will be focused on the interference output in the ground band (since total BO efficiency is a useful figure of merit) rather than

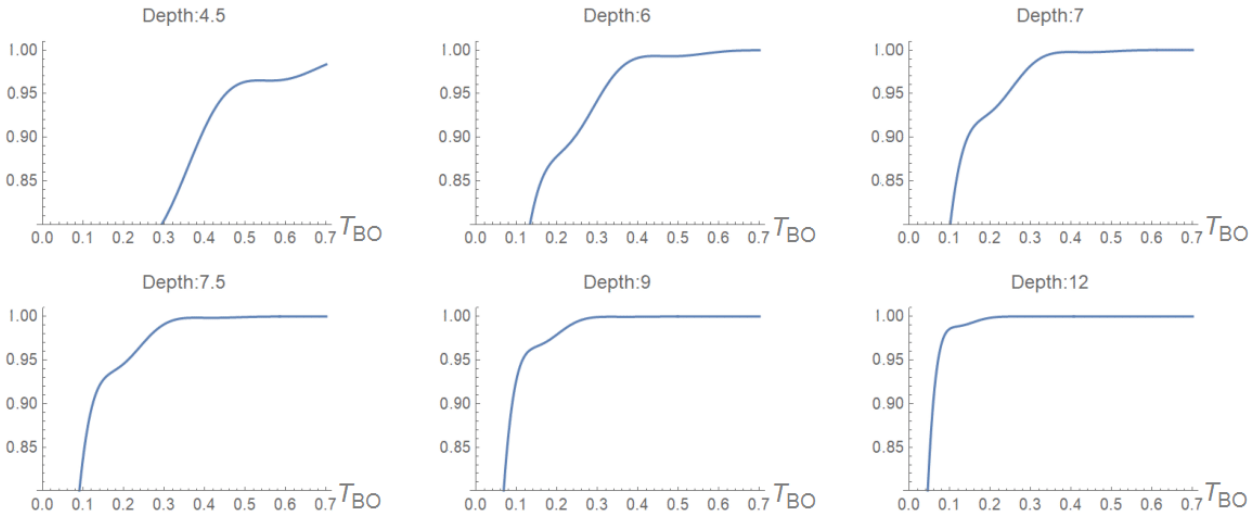

Figure 7.5: Theory curves for efficiency per BO at various depths, according to the $N_{\mathrm{BO}} = 2$ model. These assume an execution of only 2 Bloch oscillations in total and that the Bloch period, T_{BO}, is given in the units of $2\pi/\omega_{\mathrm{rec}}$.

the complementary $b = 1$ output. Based on the previously calculated state populations, the amplitude of the wavefunction in the ground band after two Bloch oscillations is

$$\tilde{A} = 1 - P_{\mathrm{LZ}}^{(1)} + P_{\mathrm{LZ}}^{(1)}\sqrt{1 - P_{\mathrm{LZ}}^{(2)}}\,\mathrm{e}^{-\mathrm{i}(\phi_{\mathrm{S}}+\phi_{\mathrm{LZ}})} \tag{7.3}$$

where ϕ_S is the Stückelberg phase given by Equation (7.2) and ϕ_{LZ} is the phase acquired during the two Landau-Zener tunneling events. The resulting ground band population, $P_{\mathrm{2BO}} = |\tilde{A}|^2$, provides us with the BO efficiency, $P_{\mathrm{eff}} = |\tilde{A}|$, which may be neatly expressed as

$$P_{\mathrm{eff}} = \sqrt{\alpha^2 + \beta^2 + 2\alpha\beta\cos\left(\phi_{\mathrm{S}} + \phi_{\mathrm{LZ}}\right)} \tag{7.4}$$

where $\alpha = 1 - P_{\mathrm{LZ}}^{(1)}$ and $\beta = P_{\mathrm{LZ}}^{(1)}\sqrt{1 - P_{\mathrm{LZ}}^{(2)}}$. Due to our earlier constraints set on the Landau-Zener tunneling probabilities, it is plausible that we may operate in the regime where $P_{\mathrm{LZ}}^{(1)} \ll 1$ and $\beta \ll 1$. This allows us to make the approximation

$$\begin{aligned} P_{\mathrm{eff}} &\simeq \alpha + \tfrac{1}{2}\beta + \alpha\beta\cos\left(\phi_{\mathrm{S}} + \phi_{\mathrm{LZ}}\right) \\ &= \alpha + \tfrac{1}{2}\beta - \alpha\beta\cos\left(\phi_{\mathrm{S}}\right) \end{aligned} \tag{7.5}$$

which can be further simplified on the second line since $\phi_{\mathrm{LZ}} = \pi$ in this context [62, 49].

Comparison of the theory curves in Figure 7.5 with the data from Figure 7.1 shows that the $N_{\mathrm{BO}} = 2$ model is not sufficient to describe the behavior of many Bloch oscillations. A simple modification can be made to improve this model by replacing $\beta \rightarrow \eta\beta$, where the empirically determined factor η represents the continually increasing population in the first excited band over many BOs, which is not accounted for in the $N_{\mathrm{BO}} = 2$ model.

7.3 Extended Multi-band N_{BO} Model

A better solution, perhaps, is to use an approach which tracks the state amplitudes and phases over many Bloch oscillations and can therefore be used for arbitrary N_{BO}. Furthermore, it would be desirable for such a model to be applicable to excited-band Bloch oscillations as well. Below I will demonstrate this general treatment with vectors and matrix operators truncated to three states; however, one may easily extend the model to include more states for when higher band gaps are non-negligible or when performing excited-band Bloch oscillations.

7.3.1 Many Bloch Oscillations ($N_{\mathrm{BO}} > 2$)

In a sense this could be considered a simple recasting and extension of the $N_{\mathrm{BO}} = 2$ model, where we now need to define the state vector, Ψ_0, in addition to the various propagation operators. Let the components of Ψ_0 describe the initial population amplitudes in the lowest three Bloch states. We will break down the propagators into two discrete events—transitions through avoided crossings at either $q = 0$ or $q = \pm\hbar k$—and a continuous evolution of phase for each Bloch oscillation. Denoting the discrete operators $\hat{D}_0$ and $\hat{D}_{\pm 1}$ corresponding to

quasimomentum, and the continuous operator $\hat{M}_{1/2}$ for each half-BO, we have

$$\begin{aligned}
\hat{D}_0 &= \begin{pmatrix} 1 & 0 & 0 \\ 0 & \sqrt{1-P_{\mathrm{LZ}}^{(2)}}\,\mathrm{e}^{-\mathrm{i}\delta^{(2)}} & -\sqrt{P_{\mathrm{LZ}}^{(2)}} \\ 0 & \sqrt{P_{\mathrm{LZ}}^{(2)}} & \sqrt{1-P_{\mathrm{LZ}}^{(2)}}\,\mathrm{e}^{\mathrm{i}\delta^{(2)}} \end{pmatrix} \\
\hat{D}_{\pm 1} &= \begin{pmatrix} \sqrt{1-P_{\mathrm{LZ}}^{(1)}}\,\mathrm{e}^{-\mathrm{i}\delta^{(1)}} & -\sqrt{P_{\mathrm{LZ}}^{(1)}} & 0 \\ \sqrt{P_{\mathrm{LZ}}^{(1)}} & \sqrt{1-P_{\mathrm{LZ}}^{(1)}}\,\mathrm{e}^{\mathrm{i}\delta^{(1)}} & 0 \\ 0 & 0 & \sqrt{1-P_{\mathrm{LZ}}^{(3)}}\,\mathrm{e}^{-\mathrm{i}\delta^{(3)}} \end{pmatrix} \\
\hat{M}_{1/2} &= \begin{pmatrix} 1 & 0 & 0 \\ 0 & \mathrm{e}^{-\mathrm{i}\phi_{\mathrm{S}}^{(1)}/2} & 0 \\ 0 & 0 & \mathrm{e}^{-\mathrm{i}\phi_{\mathrm{S}}^{(2)}/2} \end{pmatrix}
\end{aligned} \tag{7.6}$$

where the Stokes phase, $\delta^{(b)}$, is acquired during the approximately instantaneous momentum transfer as the atoms pass through an avoided crossing. This phase shift can be obtained from evaluating Weber's functions at a regular singularity [68, 70, 49], which in this case yields

$$\delta^{(b)} = \frac{\pi}{4} + \arg\Gamma(1-\mathrm{i}\gamma^{(\mathrm{b})}) + \gamma^{(b)}(\ln\gamma^{(b)} - 1)\ . \tag{7.7}$$

Here $\Gamma(z)$ is the Γ function and $\gamma^{(b)}$ is related to the Landau-Zener tunneling probability by $P_{\mathrm{LZ}}^{(b)} = \mathrm{e}^{-2\pi\gamma^{(b)}}$. Also, the Stückelberg phase is now more generally defined as

$$\begin{aligned}
&\phi_{\mathrm{S}}^{(b)} = \tfrac{1}{\hbar} T_{\mathrm{BO}} \left\langle \Delta E^{(b)} \right\rangle \\
&\text{where} \quad \left\langle \Delta E^{(b)} \right\rangle = \tfrac{1}{2\hbar k} \int_{-\hbar k}^{+\hbar k} \left(E_b(q) - E_{b-1}(q)\right) \mathrm{d}q\ .
\end{aligned} \tag{7.8}$$

Using the 3×3 matrix operators from Equation (7.6), we can express a single operator for one full Bloch oscillation. Recall that for ground-band BOs the atoms typically start and end at $q = 0$, so in this case the correct order of assembly is

$$\hat{M} = \hat{M}_{1/2}\hat{D}_{\pm 1}\hat{M}_{1/2}\hat{D}_0\ . \tag{7.9}$$

For a total of N Bloch oscillations the final state vector is $\Psi_N = \hat{M}^N \Psi_0$.

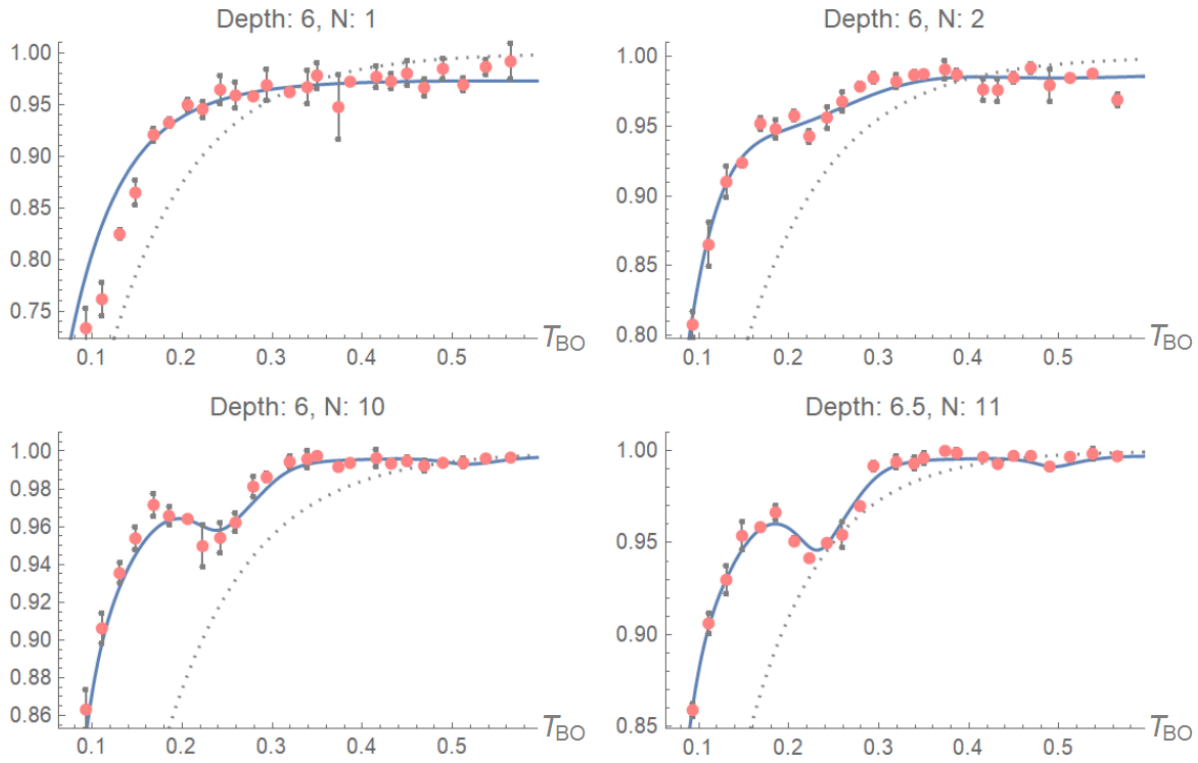

Figure 7.6: Theory curves and data for efficiency per BO at various depths, according to the extended N_{BO} model. Solid blue curves were calculated using the aforementioned model with an empirical correction, while dotted black lines show simply $1 - P_{LZ}^{(1)}$. Data are taken from a subset of those in Figure 7.3. As usual the Bloch period, T_{BO}, is given in the units of $2\pi/\omega_{rec}$.

At very large T_{BO} or N_{BO} spontaneous scattering becomes significant. This can be incorporated into the model by simply adding a scalar factor to the multi-BO operator, resulting in something like Equations (5.5).

$$\hat{M}_{tot} = (1 - P_{int})^2 e^{-R_s T_{BO} N} \hat{M}^N \tag{7.10}$$

where R_s is the spontaneous scattering rate for a given lattice depth and single-photon detuning as defined before, from which P_{int} is calculated as the spontaneous scattering probability during each of the lattice beam intensity ramps.

While the $N_{BO} = 2$ model predicted a Landau-Zener-Stückelberg resonance which was

too weak, the many-N_{BO} model for multipath LZS interference predicts resonances that are too strong. This can be observed in Figure 7.6 along with the more sweeping underestimation of the BO efficiency. Here the model is used with variable N and compared to a set of data from Section 7.1. Similar to our conclusion with the $N_{\mathrm{BO}} = 2$ model, an empirical correction $\left(\gamma^{(b)} \to c\gamma^{(b)}\right)$ can be used[2] to modify $P_{\mathrm{LZ}}^{(b)}$; however, this does not help improve predictive power, indicating that there remain aspects of the model which need to be investigated further.

7.3.2 Excited-band Bloch Oscillations

Alongside the ground-band BO experiments, we also conducted multipath LZS interferometry in the first-excited band. In regard to our recently discussed model, there are two important considerations when performing Bloch oscillations in an excited band. First, for a given lattice depth, the average band gap grows larger with b but the minimum band gap becomes smaller. This means that each resonance will occur at smaller T_{BO} while diminishing $P_{\mathrm{LZ}}^{(b)}$ restricts our window of observable BO efficiencies to higher T_{BO}. Fortunately a straightforward increase in lattice depth will bring these two regimes into conjunction by satisfying the usual constraints on the tunneling probabilities. Second, atoms which tunnel to lower band(s) are not lost from the system because there exist only a finite number of bands below any excited band. This suggests that there may be additional LZS resonances between different sets of Bloch bands; however, this effect should be captured within our extended multi-band model, which must now include more than a 3-state approximation in the truncation of matrix operators for excited-band Bloch oscillations.

In Figure 7.7 we are able to see multiple resonances in the $b = 1$ BO efficiency at higher lattice depths, although those in the low-depth experiments appear fairly weak. Calculation of the Stückelberg phase using Equation (7.8) continues to provide exceptionally good agreement with the measured resonances, in this case between $b = 1$ and $b = 2$. These LZS

[2]In Fig. 7.6 a linear form of this function was used to match the data.

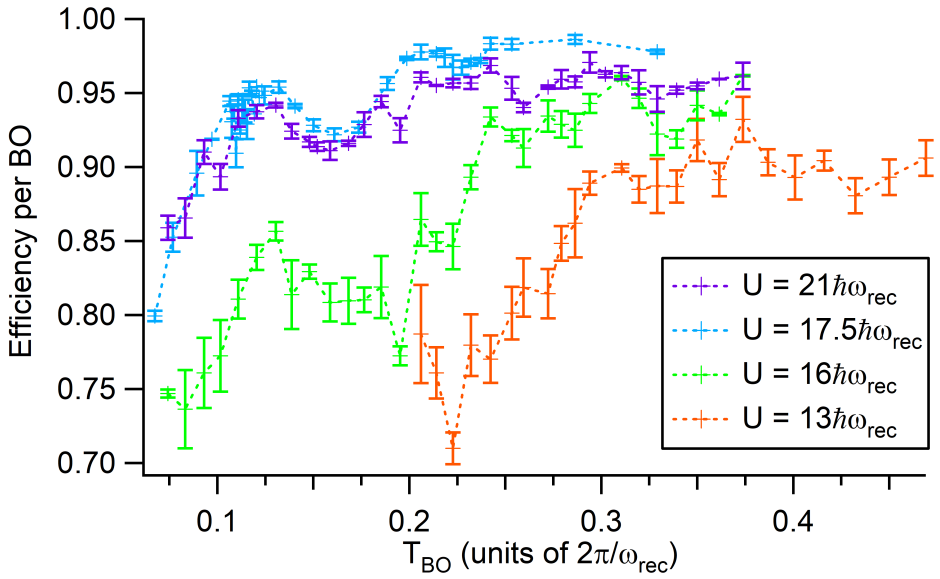

Figure 7.7: LZS resonances shown in the BO efficiency in the first-excited band, $b = 1$, performed at various lattice depths. There we found additional unexpected features at certain T_{BO} not predicted by the multi-band N_{BO} model. Dashed lines are provided as a guide to the eye. For all data shown, the BO intensity ramp time was 300 μs and the single-photon detuning of the diffraction beams was $\Delta = -3500\Gamma$.

resonances are observable in the figure as broad dips around 0.15 to $0.2 \times 2\pi/\omega_{\mathrm{rec}}$, except for the data at $U = 13\hbar\omega_{\mathrm{rec}}$ which was limited by the low overall efficiency. We were surprised again, however, to find additional features which could not be captured by the multi-band N_{BO} model, even with an empirical correction. First, there are sharp dips in efficiency occurring at values of T_{BO} just above the aforementioned LZS resonance. Second, we confirmed the presence of a smaller dip at $0.23 \times 2\pi/\omega_{\mathrm{rec}}$ visible for depths $U = 17.5\hbar\omega_{\mathrm{rec}}$ and $21\hbar\omega_{\mathrm{rec}}$.

We attempted a variety of modifications to the model which might explain these anomalies: The Stückelberg phase was calculated for trajectories through non-adjacent bands forming an interferometer over multiple Bloch oscillations. The gravitational phase shift was included, due to the accumulated vertical spatial separation of the Bloch states over the course of the BO pulse. Analysis of the Stokes phase [70, 49] was performed to account for small, nonzero phase shifts that may become non-negligible at lower lattice depths during

band transitions. Unfortunately, none of these adaptations were successful and at this point the experimental focus began shifting back to vertical contrast interferometry.

Certainly further modeling needs to be done to fully capture the features of multipath Landau-Zener-Stückelberg interference in excited Bloch bands. Nonetheless, we have already shown a clear improvement upon $P_{\mathrm{LZ}}^{(1)}$ in ground-band LZS interferometry exist at the anti-resonances. Thus future corrections upon this model could aid in obtaining greater than $1 - P_{\mathrm{LZ}}^{(b)}$ for Bloch oscillation efficiency in excited bands. This would be of particular use towards bettering the efficiency of excited-band BOs at the magic depth which, while much more phase-stable than ground-band BOs, are otherwise generally less efficient.

Appendix A

PROGRAMMING THE DDS
(*THROUGH AN ARDUINO THROUGH CICERO*)

Following is the list of commands currently available in Cicero to control several DDSs (model: AD9910) through an Arduino (model: Due). To input the command in Cicero, use the RS232 tab and enter the desired command below, creating a new RS232 group if necessary. Click "Output Now" to output commands outside of a running sequence. Adding an RS232 group into the sequence will allow commands to be sent during an experimental run; however, take into account the timing of sent commands in a sequence is unpredictable at the 100 ms level. The interpretation of commands by the Arduino is not very flexible, so be sure the input command matches one of the general forms below (e.g. no extra/missing spaces, correct upper/lower case letters, no commas or decimals in numbers, always end with a semicolon). Cicero only has one-way communication with the Arduino, so there is *no error notification* if the command syntax has been broken. Many commands only address a single DDS at a time, allowing for a greater variety of individual settings in your experiment. The DDS which a particular command is being sent to should be designated by substituting the X parameter with capital letter A, B, or C. All N parameters are numeric with specified range and units (if applicable) for each command.

`PLL X, N;` $\{0 \leq N \leq 100, \max\}$

This command is used when you want to change the master clock frequency of a DDS. For our model of DDS the master clock may be derived from a source with the desired master frequency or some fraction, 1/N, of the desired frequency. The PLL command therefore will tell the DDS to use a phase locked loop, which multiplies a reference frequency by N to create the DDS master clock. The current setup for our DDSs includes a 10MHz reference

signal with a 100x PLL multiplier to obtain a 1GHz master clock.

While avoiding too much detail below, it should first be advised to carefully look over the AD9910 datasheet [3] before changing any of the PLL parameters. Neither the DDS, Arduino, or Cicero can detect the reference clock frequency, so if there is ever any change made to the reference frequency, this must be updated in the Arduino code (look for sourceFreq_X). Because there is a range of allowed reference/master frequencies, the PLL commands accepts N from 0 to 100. However, due to the nature of phase locked loops, as well as the limits of the AD9910, certain combinations of reference frequency and N parameter will not work. Finally, replacing the typically numeric N with the word "max" should allow the user to set the master clock to the maximum allowed by the DDS.

`OSK X, N;` $\{N = 0,1\}$

Our DDSs are set up to use the output shift keying module as a switch to turn on/off their RF output. Setting N to 1 or 0 will enable or disable this feature, respectively. If OSK is turned off, the amplitude of the RF output will be forced to 0. Consider this if troubleshooting a lack of RF. If OSK is turned on, the effective RF switch can be controlled by the corresponding digital channels in Cicero.

`amp X, N;` $\{0 \leq N \leq 16383, \text{max}\}$

While OSK is on and the RF switch is open, the amplitude of the RF signal is mostly set by an external feedback system, but also in part by this command. Generally, once the feedback system is set up, the RF amplitude is controlled by the corresponding channel in Cicero and this value won't need to be changed. When setting up feedback, chose a value of N here such that the light level is sufficiently low with 0 V on the analog channel. Finally, replacing the typically numeric N with the word "max" should be equivalent to setting N to 16383 without having to remember the range of N for this command.

`DRG X, N;` $\{N = 0,1\}$

The AD9910 has multiple modes for frequency control. The two we use are (i) limiting

its RF output to a set of fixed frequencies and (ii) linearly ramping the frequency between two endpoint frequencies. The first mode is useful for conducting a series of Bragg pulses, but can not do Bloch oscillations. The second mode can easily do Bloch oscillations, but some tricks must be played if you want to mix in Bragg pulses into the same sequence (e.g. ramping in the dark and using the hold functionality). See the AD9910 datasheet [3] for details. The digital ramp generator controls the ramping mode, so setting N to 1 will enable this feature. Setting N to 0 will disable this feature and the DDS will return to its default mode of using a set of fixed frequency profiles. Finally, it is worth noting here the relation between frequency on the diffraction AOM and the atom momenta: 14852 Hz corresponds to 1 $\hbar k$. This calibration is useful when setting up experimental sequences.

`freq XP, N;` $\{0 \leq \mathrm{P} \leq 7\}$ & $\{0 \leq \mathrm{N} \leq 400000000\}$ Hz

This command is used to assign a set of 8 different frequency profiles, which can be called upon only while DRG is disabled. The set of frequencies is indexed from 0 by parameter P. Once it has been programmed, each profile may be called upon using the three digital channels in Cicero designated for this 3-bit profile selection.

The range of accepted frequencies is everything below 400 MHz, which is set to prevent going above the Nyquist frequency. Note that because this is an RF device, you will have trouble with frequencies below roughly 10 MHz. In our experiment, we use the DDSs to control a 200 MHz AOM, so these limits are not a concern. Currently, only two DDSs are wired for this select frequency control (DDS B and C).

`freq high X, N;` $\{\mathrm{freqLow\_X} \leq \mathrm{N} \leq 400000000\}$ Hz

This command (along with the next 9) are used when DRG is enabled. When operating with the DRG mode, the RF frequency will continuously ramp in the direction specified by appropriate ramping digital channel in Cicero. The frequency will only stop ramping when held (using another digital channel in Cicero) or when it reaches the upper or lower frequency limit and tries to continue ramping in that direction. See the AD9910 datasheet, especially

page 30, for details [3]. Currently, all DDSs are wired to allow for digital ramp control.

Use this command to set the frequency upper limit for an individual DDS. If the value of N is less than the frequency lower limit, the upper limit will not change and will remain whatever it had been previously.

`freq low X, N;` $\{0 \leq N \leq \text{freqHigh\_X}\}$ Hz

This command is used to set the frequency lower limit for an individual DDS. If the value of N is higher than the frequency upper limit, the lower limit will not change and will remain whatever it had been previously.

`freq ramp pos time X, N;` $\{4 \leq N \leq 262140\}$ ns

Since DDSs are digital devices, the linear frequency sweep in DRG mode is not a truly continuous sweep. Instead, the frequency is made incrementally larger or smaller over a series of discrete time steps. The frequency ramp rate is therefore determined by the size of the frequency step as well as the length of the time step. As an added feature, the AD9910 allows for differing ramp parameters for the positive and negative frequency ramps. Use this command to set the length of the time step for the positive ramp on an individual DDS. The limits on N are determined from the frequency of the master clock (see AD9910 datasheet for details [3]).

`freq ramp pos step X, N;` $\{0 \leq N \leq 400000000\}$ Hz

This command is used to set the size of the frequency step for the positive ramp on an individual DDS.

`freq ramp neg time X, N;` $\{4 \leq N \leq 262140\}$ ns

This command is used to set the length of the time step for the negative ramp on an individual DDS.

`freq ramp neg step X, N;` $\{0 \leq N \leq 400000000\}$ Hz

This command is used to set the size of the frequency step for the negative ramp on an individual DDS.

`freq ramps time X, N;` $\{4 \leq N \leq 262140\}$ ns

It may become tedious to enter all of these parameters, especially if the positive and negative ramps rates are the same. Use this command to set the length of the time step for both the positive and negative ramps on an individual DDS.

`freq ramps step X, N;` $\{0 \leq N \leq 400000000\}$ Hz

This command is used to set the size of the frequency step for both the positive and negative ramps on an individual DDS.

`freq ramps time N;` $\{4 \leq N \leq 262140\}$ ns

Fortunately, the tedium may be alleviated even further if the ramp parameters are the same for all DDSs. In that case, use this command to set the length of the time step for both the positive and negative ramps on every DDS. Note that the X parameter is no longer required because this command doesn't address only one DDS.

`freq ramps step N;` $\{0 \leq N \leq 400000000\}$ Hz

This command is used to set the size of the frequency step for both the positive and negative ramps on all DDSs.

`LRR X, N;` $\{N = 0,1\}$

This command serves absolutely no purpose within the context of any potential physics experiment. It was only added for debugging an issue with the I/O Update during DRG mode. The default mode is disabled, with N set to 0, and therefore it should already be in this configuration each time the DDS is reset. Ignore this unless you are experiencing technical issues with the DDS and you are deeply familiar with the AD9910. Of course, see

the datasheet for details [3].

`reset X;`

The Arduino code includes a set of arbitrary yet functionable values that it loads onto the DDSs when it first turns on. This command will undo any changes you make and reload these preset values. Arguably, it may just be simpler to reset the DDSs by toggling the power down switch on the front of the DDS box to reinitialize them.

The entirety of this Arduino code can be found on GitHub [23]. The main file is Due_4_1_threeDDS.ino which includes the setup and loop functions. DDS_math.ino includes some user defined operations (e.g. calculating FTW). Interp_C.ino is the main piece for interpreting Cicero commands for the AD9910 and contains all of the above content in this Appendix. Finally, Profile_upload.ino and RAM_upload.ino include code for uploading to the single-tone profile and RAM registers (although RAM upload was never fully developed).

BIBLIOGRAPHY

[1] P.A. Altin, M.T. Johnsson, V. Negnevitsky, G.R. Dennis, R.P. Anderson, J.E. Debs, S.S. Szigeti, K.S. Hardman, S. Bennetts, G.D. McDonald, L.D. Turner, J.D. Close, and N.P. Robins. Precision atomic gravimeter based on Bragg diffraction. *New J. Phys.*, 15:023009, 2013.

[2] A. Altmeyer, S. Riedl, C. Kostall, M. J. Wright, R. Geursen, C. Chin, J. H. Denschlag, and R. Grimm. Precision measurements of collective oscillations in the BEC-BCS crossover. *Phys. Rev. Lett.*, 98:040401, 2007.

[3] Analog Devices. "1 GSPS, 14-Bit, 3.3 V CMOS, Direct Digital Synthesizer", AD9910 datasheet, 2016.

[4] M. H. Anderson, J. R. Ensher, M. R. Matthews, C. E. Wieman, and E. A. Cornell. Observation of Bose-Einstein Condensation in a Dilute Atomic Vapor. *Science*, 269:198–201, 1995.

[5] T. Aoyama, M. Hayakawa, T. Kinoshita, and M. Nio. Tenth-Order QED Contribution to the Electron g-2 and an Improved Value of the Fine Structure Constant. *Phys. Rev. Lett.*, 109:111807, 2012.

[6] P. Asenbaum, C. Overstreet, T. Kovachy, D.D. Brown, J.M. Hogan, and M.A. Kasevich. Phase Shift in an Atom Interferometer due to Spacetime Curvature across its Wave Function. *Phys. Rev. Lett.*, 118:183602, 2017.

[7] R. Battesti, P. Clade, S. Guellati-Khelifa, C. Schwob, B. Gremaud, F. Nez, L. Julien, and F. Biraben. Bloch Oscillations of Ultracold Atoms: A Tool for a Metrological Determination of h/m_{Rb}. *Phys. Rev. Lett.*, 92:253001, 2004.

[8] F. Bloch. Über die Quantenmechanik der Elektronen in Kristallgitter. *Z Phys*, 52:555, 1928.

[9] S.B. Cahn, A. Kumarakrishnan, U. Shim, T. Sleator, P.R. Berman, and B. Dubetsky. Time-Domain de Broglie Wave Interferometry. *Phys. Rev. Lett.*, 79:784, 1997.

[10] O. Carraz, C. Siemes, L. Massotti, R. Haagmans, and P. Silvestrin. A Spaceborne Gravity Gradiometer Concept Based on Cold Atom Interferometers for Measuring Earth's Gravity Fields. *Microgravity Sci. Technol.*, 26:139–145, 2014.

[11] S. Chu, J.E. Bjorkholm, A. Ashkin, J.P. Gordon, and L.W. Hollberg. Proposal for optically cooling atoms to temperatures of the order of 10^{-6} K. *Optics Letters*, 11:73, 1986.

[12] ColdQuanta, 2020. Ultra-cold atom systems, https://www.coldquanta.com/standard-products/ultra-cold-atom-systems/.

[13] A. D. Cronin, J. Schmiedmayer, and D. E. Pritchard. Optics and interferometry with atoms and molecules. *Rev. Mod. Phys.*, 81:1051, 2009.

[14] J. H. Denschlag, J. E. Simsarian, H. Haffner, C. McKenzie, A. Browaeys, D. Cho, K. Helmerson, S. Rolston, and W. D. Phillips. A Bose-Einstein condensate in an optical lattice. *J. Phys. B.*, 35:3095, 2002.

[15] S. Fishman, D. R. Grempel, and R. E. Prange. Chaos, quantum recurrences, and Anderson localization. *Phys. Rev. Lett.*, 49:509, 1982.

[16] C. J. Foot. *Atomic Physics*. Oxford University Press Inc., New York, 2005.

[17] G. T. Foster, J. B. Fixler, J. M. McGuirk, and M. A. Kasevich. Method of phase extraction between coupled atom interferometers using ellipse-specific fitting. *Optics Letters*, 27:951–953, 2002.

[18] N. Friedman, A. Kaplan, D. Carasso, and N. Davidson. Observation of chaotic and regular dynamics in atom-optics billiards. *Phys. Rev. Lett.*, 86:1518–1521, 2001.

[19] K.M. Fujiwara, K. Singh, Z.A. Geiger, R. Senaratne, S. Rajagopal, M. Lipatov, and D.M. Weld. Transport in Floquet-Bloch bands. *Phys. Rev. Lett.*, 122:010402, 2019.

[20] M. Gebbe, S. Abend, S. Jan-Niclas, M. Gersemann, H. Ahlers, H. Muntinga, S. Herrmann, N. Gaaloul, C. Schubert, and K. et al Hammerer. Twin-lattice atom interferometry. *arXiv:1907.08416*, 2019.

[21] Z.A. Geiger, K.M. Fujiwara, K. Singh, R. Senaratne, S.V. Rajagopal, M. Lipatov, T. Shimasaki, R. Driben, V.V. Konotop, T. Meier, and Weld D.M. Observation and Uses of Position-Space Bloch Oscillations in an Ultracold Gas. *Phys. Rev. Lett.*, 120:213201, 2018.

[22] D.M. Giltner, R.W. McGowan, and S.A. Lee. Theoretical and experimental study of the Bragg scattering of atoms from a standing light wave. *Phys. Rev. A.*, 52:3966, 1995.

[23] D. Gochnauer. AD9910-DUE, 2020. GitHub repository, https://github.com/dlgoch-uw/AD9910-DUE.

[24] D. Gochnauer, K. E. McAlpine, B. Plotkin-Swing, A.O. Jamison, and S. Gupta. Bloch-band picture for light-pulse atom diffraction and interferometry. *Phys. Rev. A*, 100:043611, 2019.

[25] S. Gupta, K. Dieckmann, Z. Hadzibabic, and D. E. Pritchard. Contrast Interferometry using Bose-Einstein Condensates to Measure h/m and α. *Phys. Rev. Lett.*, 89:140401, 2002.

[26] S. Gupta, A. E. Leanhardt, A. D. Cronin, and D. E. Pritchard. Coherent Manipulation of Atoms with Standing Light Waves. *Cr. Acad. Sci. IV-Phys*, 2:479, 2001.

[27] D. Hanneke, S. Fogwell, and G. Gabrielse. New measurement of the electron magnetic moment and the fine structure constant. *Phys. Rev. Lett.*, 100:120801, 2008.

[28] A. H. Hansen. *Interacting Quantum Gases of Lithium and Ytterbium*. PhD thesis, University of Washington, 2013.

[29] K. Henderson, C. Ryu, C. MacCormick, and M. G. Boshier. Experimental demonstration of painting arbitrary and dynamic potentials for Bose-Einstein condensates. *New Journal of Physics*, 11:043030, 2009.

[30] Q. Hu, J. Yang, Y. Luo, A. Jia, C. Wei, and Z. Li. A theoretical analysis and determination of the technical requirements for a Bragg diffraction-based cold atom interferometry gravimeter. *Optik*, 131:632, 2017.

[31] A. O. Jamison. *Precision Interferometry with Bose-Einstein condensates*. PhD thesis, University of Washington, 2014.

[32] A. O. Jamison, J. N. Kutz, and S. Gupta. Atomic interactions in precision interferometry using bose-einstein condensates. *Phys. Rev. A.*, 84:043643, 2011.

[33] A. O. Jamison, B. Plotkin-Swing, and S. Gupta. Advances in precision contrast interferometry with yb bose-einstein condensates. *Phys. Rev. A*, 90:063606, 2014.

[34] S. Kling, T. Salger, C. Grossert, and M. Weitz. Atomic Bloch-Zener Oscillations and Stückelberg Interferometry in Optical Lattices. *Phys. Rev. Lett.*, 105:215301, 2010.

[35] T. Kovachy, S. Chiow, and M. A. Kasevich. Adiabatic-rapid-passage multiphoton Bragg atom optics. *Phys. Rev. A*, 86:011606(R), 2012.

[36] T. Kovachy, J.M. Hogan, A. Sugarbaker, S.M. Dickerson, C.A. Donnelly, C. Overstreet, and M.A. Kasevich. Matter wave lensing to picokelvin temperatures. *Phys. Rev. Lett.*, 114:143004, 2015.

[37] J. Lee, J. H. Lee, J. Noh, and J. Mun. Core-shell magneto-optical trap for alkaline-earth-metal-like atoms. *Phys. Rev. A*, 91:053405, 2015.

[38] W. Lunden, L. Du, M. Cantara, P. Barral, A. O. Jamison, and W. Ketterle. Enhancing the capture velocity of a Dy magneto-optical trap with two-stage slowing. *Phys. Rev. A*, 101:063403, 2020.

[39] K. E. McAlpine. *Advancing Atom Interferometry with a Bloch-bands Approach*. PhD thesis, University of Washington, 2019.

[40] K. E. McAlpine, D. Gochnauer, and S. Gupta. Excited-band Bloch oscillations for precision atom interferometry. *Phys. Rev. A*, 101:023614, 2020.

[41] G.D. McDonald, C.C.N. Kuhn, S. Bennetts, J.E. Debs, K.S. Hardman, M. Johnsson, J.D. Close, and N.P. Robins. $80\hbar k$ momentum separation with Bloch oscillations in an optically guided atom interferometer. *Phys. Rev. A*, 88:053620, 2013.

[42] H. J. Metcalf and P. van der Straten. *Laser Cooling and Trapping*. Springer, New York, 1999.

[43] A. A. Michelson and E. W. Morley. On the relative motion of the Earth and the luminiferous ether. *Am. J. Sci.*, 34:333–345, 1887.

[44] V. Milner, J. L. Hanssen, W. C. Campbell, and M. G. Raizen. Optical billiards for atoms. *Phys. Rev. Lett.*, 86:1514–1517, 2001.

[45] P. J. Mohr, B. N. Taylor, and D. B. Newell. CODATA recommended values of the fundamental physical constants: 2006. *Rev. Mod. Phys.*, 80:633, 2008.

[46] F. L. Moore, J. C. Robinson, C. F. Bharucha, B. Sundaram, and M. G. Raizen. Atom optics realization of the quantum δ-kicked rotor. *Phys. Rev. Lett.*, 75:4598, 1995.

[47] H. Müntinga, H. Ahlers, M. Krutzik, A. Wenzlawski, S. Arnold, D. Becker, K. Bongs, H. Dittus, H. Duncker, N. Gaaloul, C. Gherasim, E. Giese, C. Grzeschik, T. W. Hänsch, O. Hellmig, W. Herr, S. Herrmann, E. Kajari, S. Kleinert, C. Lämmerzahl, W. Lewoczko-Adamczyk, J. Malcolm, N. Meyer, R. Nolte, A. Peters, M. Popp, J. Reichel, A. Roura, J. Rudolph, M. Schiemangk, M. Schneider, S. T. Seidel, K. Sengstock, V. Tamma, T. Valenzuela, A. Vogel, R. Walser, T. Wendrich, P. Windpassinger,

W. Zeller, T. van Zoest, W. Ertmer, W. P. Schleich, and E. M. Rasel. Interferometry with Bose-Einstein condensates in microgravity. *Phys. Rev. Lett.*, 110:093602, 2013.

[48] M. K. Oberthaler, S. Bernet, E. M. Rasel, J. Schmiedmayer, and A. Zeilinger. Inertial sensing with classical atomic beams. *Phys. Rev. A*, 54:3165, 1996.

[49] T. Ota, K. Hitachi, and K. Muraki. Landau-Zener-Stückelberg interference in coherent charge oscillations of a one-electron double quantum dot. *Scientific Reports*, 8:5491, 2018.

[50] Z. Pagel, W. Zhong, R. Parker, C. Olund, N. Yao, and H. Müller. Symmetric Bloch oscillations of matter waves. *arXiv:1907.05994*, 2019.

[51] R. H. Parker, C. Yu, B. Estey, W. Zhong, and H. Müller. Measurement of the fine-structure constant as a test of the Standard Model. *Science*, 360:191, 2018.

[52] A. Peters, K.Y. Chung, and S. Chu. High-precision gravity measurements using atom interferometry. *Metrologia*, 38:25, 2001.

[53] B. Plotkin-Swing. *Large Momentum Separation Matter Wave Interferometry.* PhD thesis, University of Washington, 2018.

[54] B. Plotkin-Swing, D. Gochnauer, K.E. McAlpine, E.S. Cooper, A.O. Jamison, and S. Gupta. Three-Path Atom Interferometry with Large Momentum Separation. *Phys. Rev. Lett.*, 121:133201, 2018.

[55] B. Plotkin-Swing, A. Wirth, D. Gochnauer, T. Rahman, K. E. McAlpine, and S. Gupta. Crossed-beam slowing to enhance narrow-line ytterbium magneto-optic traps. *Review of Scientific Instruments*, 91:093201, 2020.

[56] R. Rana, M. Hocker, and E. G. Myers. Atomic masses of strontium and ytterbium. *Phys. Rev. A*, 86:050502(R), 2012.

[57] R. Roy, A. Green, R. Bowler, and S. Gupta. Rapid cooling to quantum degeneracy in dynamically shaped atom traps. *Phys. Rev. A.*, 93:043403, 2016.

[58] C. Ryu, P. W. Blackburn, A. A. Blinova, and M. G. Boshier. Experimental realization of Josephson junctions for an atom SQUID. *Phys. Rev. Lett.*, 111:205301, 2013.

[59] V. Schkolnik, O. Hellmig, A. Wenzlawski, J. Grosse, A. Kohfeldt, K. Döringshoff, A. Wicht, P. Windpassinger, K. Sengstock, C. Braxmaier, M. Krutzik, and A. Peters. A compact and robust diode laser system for atom interferometry on a sounding rocket. *Appl. Phys. B*, 122:217, 2016.

[60] B. Seo, P. Chen, Z. Chen, W. Yuan, M. Huang, S. Du, and G. Jo. Efficient production of a narrow-line erbium mot with two-stage slowing. *Phys. Rev. A*, 102:013319, 2020.

[61] K. Shibata, H. Ikeda, R. Suzuki, and T. Hirano. Compensation of gravity on cold atoms by a linear optical potential. *Phys. Rev. Research*, 2:013068, 2020.

[62] M. Sillanpää, T. Lehtinen, A. Paila, Y. Makhlin, and P. Hakonen. Continuous-time monitoring of Landau-Zener interference in a Cooper-pair box. *Phys. Rev. Lett.*, 96:187002, 2006.

[63] M. J. Snadden, J. M. McGuirk, P. Bouyer, K. G. Haritos, and M. A. Kasevich. Measurement of the earth's gravity gradient with an atom interferometer-based gravity gradiometer. *Phys. Rev. Lett.*, 81:971, 1998.

[64] E.C.G. Stückelberg. Theory of inelastic collisions between atoms. *Helvetica Physica Acta*, 5:369–423, 1932.

[65] S. Sturm, F. Kohler, J. Zatorski, A. Wagner, Z. Harman, G. Werth, W. Quint, C.H. Keitel, and K. Blaum. High-precision measurement of the atomic mass of the electron. *Nature*, 506:467, 2014.

[66] A. Sugarbaker, S.M. Dickerson, J.M. Hogan, D.M.S. Johnson, and M.A. Kasevich. Enhanced atom interferometer readout through the application of phase shear. *Phys. Rev. Lett.*, 111:113002, 2013.

[67] B.C. Young, M. A. Kasevich, and S. Chu. Precision Atom Interferometry with Light Pulses. *Atom Interferometry*, edited by P.Berman, Academic Press, New York, 1997.

[68] C. Zener. Non-adiabatic crossing of energy levels. *Proc. R. Soc. London A*, 137:696–702, 1932.

[69] A. Zenesini, D. Ciampini, O. Morsch, and E. Arimondo. Observation of Stückelberg oscillations in accelerated optical lattices. *Phys. Rev. A*, 82:065601, 2010.

[70] C. Zhu and H. Nakamura. Theory of nonadiabatic transition for general two-state curve crossing problems: Nonadiabatic tunneling case. *J. Chem. Phys.*, 101:10630, 1994.